

UNCLASSIFIED

AD NUMBER
AD816184
NEW LIMITATION CHANGE
TO Approved for public release, distribution unlimited
FROM Distribution authorized to U.S. Gov't. agencies and their contractors; Critical Technology; MAY 1967. Other requests shall be referred to Air Force Weapons Laboratory, Attn: Research and Technology Division, Kirtland AFB, NM.
AUTHORITY
afwl ltr, 30 nov 1971

THIS PAGE IS UNCLASSIFIED

AD816184

AFWL-TR-66-163, Vol II

AFWL-TR  
66-163  
Vol II



## STRUCTURAL RESPONSE OF SPINE VEHICLES

Volume II

Simulation of Transient Surface Loads  
by Explosive Blast Waves

H. E. Lindberg                      R. D. Firth  
Stanford Research Institute  
Poulter Laboratories  
Menlo Park, California 94025  
Contract AF 29(601)-7129

TECHNICAL REPORT NO. AFWL-TR-66-163, Volume II

May 1967

AIR FORCE WEAPONS LABORATORY  
Research and Technology Division  
Air Force Systems Command  
Kirtland Air Force Base  
New Mexico

AFWL-TR-66-163, Vol II

Research and Technology Division  
AIR FORCE WEAPONS LABORATORY  
Air Force Systems Command  
Kirtland Air Force Base  
New Mexico

When U. S. Government drawings, specifications, or other data are used for any purpose other than a definitely related Government procurement operation, the Government thereby incurs no responsibility nor any obligation whatsoever, and the fact that the Government may have formulated, furnished, or in any way supplied the said drawings, specifications, or other data, is not to be regarded by implication or otherwise, as in any manner licensing the holder or any other person or corporation, or conveying any rights or permission to manufacture, use, or sell any patented invention that may in any way be related thereto.

This report is made available for study with the understanding that proprietary interests in and relating thereto will not be impaired. In case of apparent conflict or any other questions between the Government's rights and those of others, notify the Judge Advocate, Air Force Systems Command, Andrews Air Force Base, Washington, D. C. 20331.

This document is subject to special export controls and each transmittal to foreign governments or foreign nationals may be made only with prior approval of AFWL (WLRP), Kirtland AFB, NM, 87117. Distribution is limited because of the technology discussed in the report.

DO NOT RETURN THIS COPY. RETAIN OR DESTROY.

STRUCTURAL RESPONSE OF SPINE VEHICLES

Volume II

Simulation of Transient Surface Loads  
by Explosive Blast Waves

H. E. Lindberg                      R. D. Firth  
Stanford Research Institute  
Poulter Laboratories  
Menlo Park, California 94025  
Contract AF 29(601)-7129

TECHNICAL REPORT NO. AFWL-TR-66-163, Volume II

This document is subject to special export controls and each transmittal to foreign governments or foreign nationals may be made only with prior approval of AFWL (WLRP), Kirtland AFB, NM, 87117. Distribution is limited because of the technology discussed in the report.

FOREWORD

This report was prepared by Poulter Laboratories, Stanford Research Institute, Menlo Park, California, under Contract AF 29(601)-7129. The research was performed under Program Element 7.60.06.01.D, Project 5710, Subtask 01.028, and was funded by the Defense Atomic Support Agency (DASA).

Inclusive dates of research were 4 December 1965 to 15 September 1966. The report was submitted 20 April 1967 by the Air Force Weapons Laboratory Project Officer, Lt Walter D. Dittmer (WLRP). Technical direction was provided by Lt Dittmer in coordination with Captain L. T. Montulli and Lt R. H. Brightman.

The contractor's report number is SRI Project FGU-5935.

Volume I contains Secret-Restricted Data information and is titled "Impulsive Structural Response of the SPINE Conceptual Reentry Vehicles (U)."

The electronic portions of the experiments were performed by R. E. Ray and K. E. Nelson. Mechanical assistance in preparing and firing the shots was provided by B. P. Lynch, G. S. Cartwright, E. Daigle, J. H. Yost, and others at the Calaveras Test Site.

In the course of performing the experiments several commercial products were used which can be described only by using their trade names, because in most instances their chemical description and method of manufacture are proprietary information. These products are Detasheet C, Detasheet D, Micarta, and Primacord. Permission for the use of these trade names has been obtained from the manufacturers.

This technical report has been reviewed and is approved.

*Walter D. Dittmer*

WALTER D. DITTMER  
Lt, USAF  
Project Officer

*Edgar M. Munyon*

EDGAR M. MUNYON  
Colonel, USAF  
Chief, Physics Branch

*Claude K. Stambaugh*

CLAUDE K. STAMBAUGH  
Colonel, USAF  
Chief, Research Division

## ABSTRACT

(Distribution Limitation Statement No. 2)

Techniques are described for simulating blast-type transient surface loads of nearly exponential pulse shape having characteristic times (impulse/peak pressure) ranging from 10 to 1000  $\mu$ sec (the quasi-impulsive range for cylindrical shells about 1 foot in diameter). Pressure-time histories are measured at various positions around and along cylindrical models 3.5, 6, and 12 inches in diameter. A basic set of loads is obtained consisting of two limiting pressure distributions, an asymmetric distribution typical of side exposure to a normally incident blast wave, and a symmetric distribution typical of nose-on exposure. All of the loads are obtained using sheet explosive charges of various forms, from flat to semi-cylindrical to completely cylindrical surrounding the model and flat charges suspended at various standoffs in a shock tube. In support of the experiments, the self-similar solutions for blast waves from intense explosions are used to calculate the range of sheet charges needed to produce loads of interest and to show that the corresponding spherical charges become much too small and much too large for practical application near the extremes in load duration. Approximate formulas are also derived (the Korobeinikov theory) for the variation of peak pressure with distance from plane, cylindrical, and spherical charges. The range of validity of the formulas extends from high pressures, where the self-similar solutions are valid, to acoustic shock pressures. Experimental measurements from the present program and from compiled blast data show excellent agreement with the theory over the entire range.

The **PAGES NOT FILMED ARE BLANK** ank.

## CONTENTS

<u>Section</u>		<u>Page</u>
I	INTRODUCTION . . . . .	1
	1. Features of Weapon Effect Loads . . . . .	1
	2. Basis for Simulation and Structural Response Investigations. . . . .	4
	3. Methods of Surface Load Simulation. . . . .	6
II	SUMMARY. . . . .	10
	1. Theory. . . . .	10
	2. Simulation of Asymmetric Loads. . . . .	11
	3. Simulation of Symmetric Loads . . . . .	13
	4. Variations in Load Distribution and Pulse Shape . . . . .	15
III	SIMULATION OF ASYMMETRIC LOADS . . . . .	16
	1. Theoretical Pressure Pulses . . . . .	16
	2. Experimental Arrangements . . . . .	22
	3. Surface Loads from Flat Primacord Charges . . . . .	34
	4. Surface Loads from Flat Detasheet Charges . . . . .	45
	5. Surface Loads from Flat Charges Confined in a Shock Tube . . . . .	47
	6. Effects of Model Size . . . . .	55
IV	SIMULATION OF SYMMETRIC LOADS. . . . .	58
	1. Surface Loads from Cylindrical Charges. . . . .	58
	2. Symmetric Loads in a Capped Shock Tube. . . . .	63
	3. Recommendations for Future Work . . . . .	68
V	LOADS OF OTHER DISTRIBUTIONS AND PULSE SHAPES. . . . .	69
	1. Changes in Load Distribution. . . . .	69
	2. Changes in Pulse Shape. . . . .	75

CONTENTS (Continued)

<u>Section</u>	<u>Page</u>
VI THEORY OF BLAST WAVES FROM INTENSE EXPLOSIONS IN A PERFECT GAS . . . . .	79
1. Introduction . . . . .	79
2. Summary of Self-Similar Theory . . . . .	80
3. Shock Front Motion into an Initial Pressure. . . . .	91
4. Future Theoretical Program . . . . .	96
REFERENCES. . . . .	98
DISTRIBUTION . . . . .	100

## ILLUSTRATIONS

<u>Figure</u>		<u>Page</u>
1	Representative Pressure Distributions and Pulse Shape . . . . .	3
2	Pressure-Impulse Diagram for Several Simulation Methods (for 6-inch-diameter cylinders; hyperbolic curves are buckling thresholds for 6061-T6 aluminum shells, L/D = 1). . . . .	6
3	Load Regions for Basic Simulation Methods . . . . .	9
4	Pressure-Impulse Curves for Asymmetric Loading Techniques (6-inch-diameter model). . . . .	12
5	Pressure-Impulse Curves for Symmetric Loading Techniques (6-inch-diameter model). . . . .	14
6	Incident Pressure Profiles from Self-Similar Theory . . . . .	18
7	Incident and Reflected Overpressures from Sheet Blast Waves . . . . .	20
8	Experimental Arrangement for Flat Charge Field Experiments . . . . .	23
9	Shock Radii from Individual Strands and from Charge as a Continuous Sheet . . . . .	26
10	Primacord Loading Chart for $x/S = 16$ (points are shots fired in present program) . . . . .	28
11	Pressure and Impulse versus Charge Size/Standoff. . . . .	29
12	Shock Transit Times and Apparent Shock Paths for Diagonally Detonating Primacord Charges . . . . .	30
13	Shock Impingement "or Transverse and Longitudinal Model Orientations (both drawn for $x = 2$ feet and $w = 0.114$ psf). . . . .	31
14	Detasheet Charge. . . . .	32
15	Sheet Explosive Loading Chart (strips are all 15-mil-thick Detasheet D; points are shots fired in current program). . . . .	33
16	Pressure Pulses at $\theta = 0_{mid}$ from Flat Primacord Charges at $x = 4$ feet (upper traces pressure, filtered at 120 kc; lower traces integrals, unfiltered) . . . . .	35

ILLUSTRATIONS (Continued)

<u>Figure</u>		<u>Page</u>
17	Pressure Pulses at $\theta = 0_{\text{mid}}$ from Flat Primacord Charges at $x = 1$ foot and 2 feet. . . . .	36
18	Semi-log Plot of Pressure Pulse. . . . .	37
19	Pressure Pulses along and around Model (Shot FP-70, $x = 4$ feet, $w = 0.114$ psf, signals filtered at 120 kc and recorded at 100 $\mu\text{sec/cm}$ except as noted) . . . . .	38
20	Front Face Peak Pressures versus Charge Density for $x = 4$ feet . . . . .	39
21	Measured Pressure Distributions over Front Face of Model for $x = 4$ feet. . . . .	40
22	Peak Pressure and Impulse versus Charge Density (for running detonation of Primacord charges) . . . . .	41
23	Comparison of Theoretical and Experimental Peak Pressures. . . . .	43
24	Pressure-Impulse Curves for Running Detonation of Flat Charges . . . . .	44
25	Pressure Pulses at $\theta = 0$ for Sheet Explosive Charges at $x = 0.5$ feet (sweep rate 20 $\mu\text{sec/cm}$ ) . . . . .	45
26	Peak Pressure and Impulse versus Average Thickness of Sheet Explosive Charges. . . . .	46
27	Arrangement of Flat Charges in Shock Tube. . . . .	48
28	Shock Tube Pressure Pulses at Standoffs from 1 foot to 20 feet (all at $w = 0.316$ psf except $w = 0.52$ psf x 2 in (e)). . . . .	50
29	Shock Tube Pressure Pulses at 10-foot Standoff . . . . .	51
30	Peak Shock Tube Pressures and Impulses versus Charge Density (charges freely suspended except at $x = 20$ feet, charge against bottom of tube) . . . . .	52
31	Pressure-Impulse Curves for Asymmetric Loading Techniques (6-inch-diameter model) . . . . .	54
32	Arrangement for Determining Effect of Model Size (3.5-inch and 12-inch-diameter cylinders). . . . .	56
33	Impulses of 3.5-, 6-, and 12-inch diameter Models. . . . .	57

ILLUSTRATIONS (Continued)

<u>Figure</u>		<u>Page</u>
34	Cylindrical Charges for Symmetric Quasi-Impulsive Loads. . . . .	59
35	Pressure Pulses from Cylindrical Charges (filtered at 120 kc, 50 $\mu$ sec/sec sweep). . . . .	60
36	Variation in Measured Pressures around the Circumference. . . . .	61
37	Peak Pressure and Impulse versus Cylindrical Charge Density. . . . .	62
38	Pressure-Impulse Curves for Symmetric Loading Techniques (6-inch-diameter models). . . . .	63
39	Experimental Arrangement for Symmetric Loads in Capped Shock Tube . . . . .	64
40	Incident and Reflected Pressure Pulses in Capped Shock Tube (sweep rate 1 msec/cm). . . . .	66
41	Pressure and Impulse versus Flat Charge Density in Capped Shock Tube. . . . .	67
42	Experimental Arrangement for Curved Charges. . . . .	70
43	Pressure Distributions from Uniform 0.0143-psf Charges at Various Curvatures. . . . .	72
44	Configuration of Variable Density Charges. . . . .	73
45	Pressure Distributions for Flat and Semicylindrical Charges of Variable Density (in Fig. 44) . . . . .	73
46	Shock Tube Charges of Various Lengths (all made of 400 grain/ft Primacord, total weight 2.74 lb for each). . . . .	76
47	Shock Tube Pressure Pulses for Various Length Charges of Same Total Weight (sweep rate 1 msec/cm). . . . .	77
48	Pressure Pulses from Variable Density Shock Tube Charges (sweep rate 1 msec/cm) . . . . .	78
49	Pressure Distribution in Self-Similar Blast Waves. . . . .	83
50	Incremental Expansion of an Arbitrary Sphere within the Blast Wave . . . . .	86
51	The Ratio $E_o/E = \alpha = \zeta_o^{-(\gamma+2)}$ as a Function of $\gamma$ . . . . .	88

ILLUSTRATIONS (Concluded)

<u>Figure</u>		<u>Page</u>
52	Incident Pressure Pulse at $r_f$ for Self-Similar Flow, Normalized to $p_f = 8E_o/\alpha(\nu + 2)^2 (\gamma + 1)r_f^\nu$ , $t_f = (\alpha\rho_1/E_o)^{1/2} r_f^{(\nu+2)/2}$ . . . . .	90
53	Incident Shock Overpressure Ratio versus $R = r_2/(E_o/p_1)^{1/\nu}$ . . . . .	95
54	Reflected Shock Overpressure Ratio versus $R = r_2/(E_o/p_1)^{1/\nu}$ . . . . .	96

## SECTION I

### INTRODUCTION

This report is concerned with economical methods for simulating transient surface pressure loads, similar to those produced by blast waves, on cylindrically shaped objects. The subject has wide application because these loads are produced by a variety of weapon effects and cylindrical shapes appear in a variety of structures (e.g., aircraft, missiles, satellites, and reentry vehicles).

The work is a direct extension of the study of response of reentry vehicle-type shells to blast loads under the HARTS program.<sup>1</sup> There, long duration loads were produced by shock tubes, and a limited range of moderately short duration loads, intermediate between shock tube and impulsive loads, was produced by explosive spheres. However, methods were not available for producing the entire range of intermediate duration loads with a minimum of explosive (less than 100 pounds). This report describes techniques developed to cover this intermediate range.

#### 1. Features of Weapon Effect Loads

Surface loads from a variety of weapon effects<sup>2</sup> have three common features that make simulation with blast waves possible: the pressure is applied by a gas, it varies smoothly around the surface, and the pulse shape (time history) consists of a sudden rise in pressure followed by a decay to zero pressure. These are the essential features of the diffracted pressures experienced on the leading surface of a vehicle or model enveloped by a blast wave. A complete description of the pressure-time history at every point on the model is quite involved, but to investigate structural response it is usually sufficient to characterize the load by the product of a pressure distribution and a pulse shape, i.e., the pressure distribution can be treated as the same at every

instant with the pressure varying simultaneously around the model at a single time history. Actual loads differ from this idealization; for example, a blast wave takes a finite time to sweep over the model and, also, the low pressure on the far side of the model rises slowly rather than suddenly. However, these complicating features are generally secondary, either because time differences are small compared to structural response times, or because the area in which the pressure is not properly represented by a product form is at a relatively low pressure.<sup>1</sup>

The pressure distribution for a particular weapon effect depends on the orientation of the model relative to the on-coming load source. For example, radiation induced surface loads on a cylinder illuminated from one side produces a  $\cos \theta$  distribution over the illuminated side, and no pressure on the shaded side. Side exposure to intense blast waves produces an approximately  $\cos^2 \theta$  distribution over the exposed side superimposed on a relatively low pressure that can be treated as uniform around the circumference. End-on exposure results in pressures symmetric around the circumference, while intermediate incidence angles result in varying degrees of asymmetry. Two representative distributions are sketched in Fig. 1. There is no end to the number of distributions that can be imagined, but it is reasonable to expect that the distinguishing feature of a load distribution is its degree of symmetry, and it is common practice to divide weapon encounters into two basic types, side-on (asymmetric) and nose-on (symmetric). Asymmetric loads are the most probable and generally result in more severe structural damage and have therefore received the most attention.

Separation of surface loads into asymmetric and symmetric types is a logical division for structural response. The primary response of a cylinder or cone to symmetric loads is the development of hoop membrane stresses and possibly buckling. For asymmetric loads, a net side load must also be sustained; this gives rise to beam bending and shear forces and also to large end reaction forces at points of attachment, possibly causing cracks or local yielding. Accelerations of internal components are also generally more severe for asymmetric loads. These

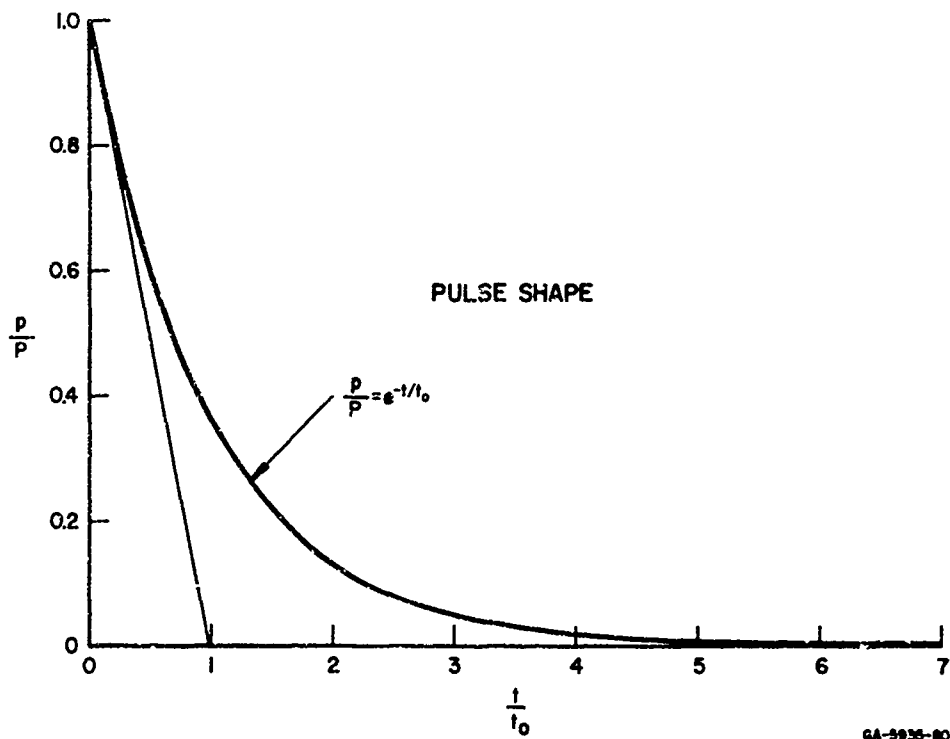
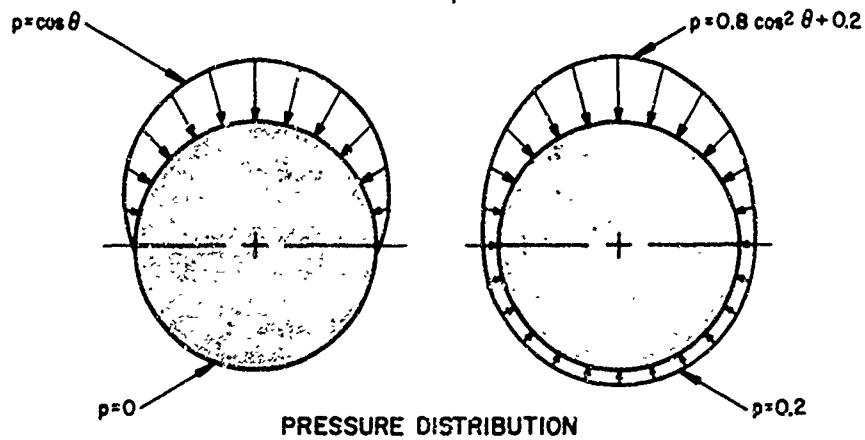


FIG. 1 REPRESENTATIVE PRESSURE DISTRIBUTIONS AND PULSE SHAPE

observations suggest that the extremes of structural response can be examined by testing with normally incident side-on exposure and with nose-on exposure. Tests on cylindrical shells<sup>1</sup> demonstrate that the exact pressure distribution of a side-on load is secondary and, in fact, for shell buckling, critical pulses for damage from asymmetric loads can be nearly the same as from symmetric loads.

The essential features of the pulse shape are exhibited by the exponential pulse

$$p = \begin{cases} 0 & t < 0 \\ P e^{-t/t_0} & t > 0 \end{cases}$$

where  $P$  is the peak pressure,  $t$  is time, and  $t_0$  is a characteristic time related to the total impulse under the pressure-time curve by  $t_0 = I/P$ . A sketch of this pulse is shown in Fig. 1. The sensible duration of the pulse is about  $5t_0$ . Actual pulses differ from this exponential shape, but the value of 5 is a representative ratio between sensible duration and an artificial characteristic time defined by  $I/P$ . For either the idealized exponential or the actual pulse, selection of a sensible duration is quite subjective; to avoid this difficulty we shall use instead the artificial characteristic time  $t_0 = I/P$  for any pulse. If the pulses do not differ widely from a single pulse shape, they can be characterized by two parameters, for example peak pressure and impulse, or peak pressure and characteristic time. Surface loads from weapon effects of interest here have pressures ranging from many kilobars to a few bars, and characteristic times ranging from a fraction of a microsecond to many milliseconds.

## 2. Basis for Simulation and Structural Response Investigations

To determine structural response to each weapon effect separately would be both expensive and time-consuming. If the problem is inverted, however, and structural response is first determined for a range of loads significant to the structure, it will then be relatively easy to determine structural response for a particular weapon effect. To fully exploit this approach, it is essential that structural response be understood over the entire range of loads; only then can the influence of load characteristics on structural response be discussed in terms of the structure rather than in terms of a specific weapon effect.

From the preceding discussion, and arguments given in Reference 1, we take the essential surface load parameters to be peak pressure, impulse, and, to a lesser extent, the symmetry of the pressure distribution. An adequate description of the strength of a given structure for weapon effects work can then be obtained by tests using two pressure distributions, one symmetric and the other asymmetric, and pressure pulses ranging in peak pressure and impulse over the range of significance to the structure. All of the remaining details of the actual loads are expected to be of secondary importance. These include effects of pulse shape (e.g., triangular vs. exponential decay), detailed pressure distribution (e.g.,  $\cos \theta$  vs.  $\cos^2 \theta$  load on one side, or the effect of small pressures on the unloaded side) and time phasing (e.g., inexact simulation of the time for a blast wave to sweep over the model). Since this simplification is merely a reasonable assumption and not an a priori conclusion, the approach is to examine the effect on structural response of changing these details within the capabilities of simple tests. If the resulting effects are indeed small, then the main bulk of experiments can be run using more standard tests with fewer parameters. This results in a systematic method for determining structural vulnerability and avoids the excessive expense of attempting "exact" simulation, which can never be attained.

Peak pressure and impulse are chosen as the two parameters to characterize the pulse because these are the significant parameters at each extreme of pulse duration; for very short durations response depends only on impulse and for very long durations response depends only on peak pressure. For intermediate values the response depends on both pressure and impulse. Critical curves for a given extent of damage often have a hyperbolic shape in the pressure-impulse plane; for example, Fig. 2 (taken from Reference 1) shows curves for simple cylindrical shells of aluminum subjected to asymmetric loads. In this plane, lines of constant characteristic time  $t_0$  are rays through the origin or, in the log-log plot of Fig. 2, parallel lines at unit slope. To experimentally determine critical damage curves, methods must be available to provide pulses throughout the entire region of interest in the pressure-impulse plane for both asymmetric and symmetric loads.

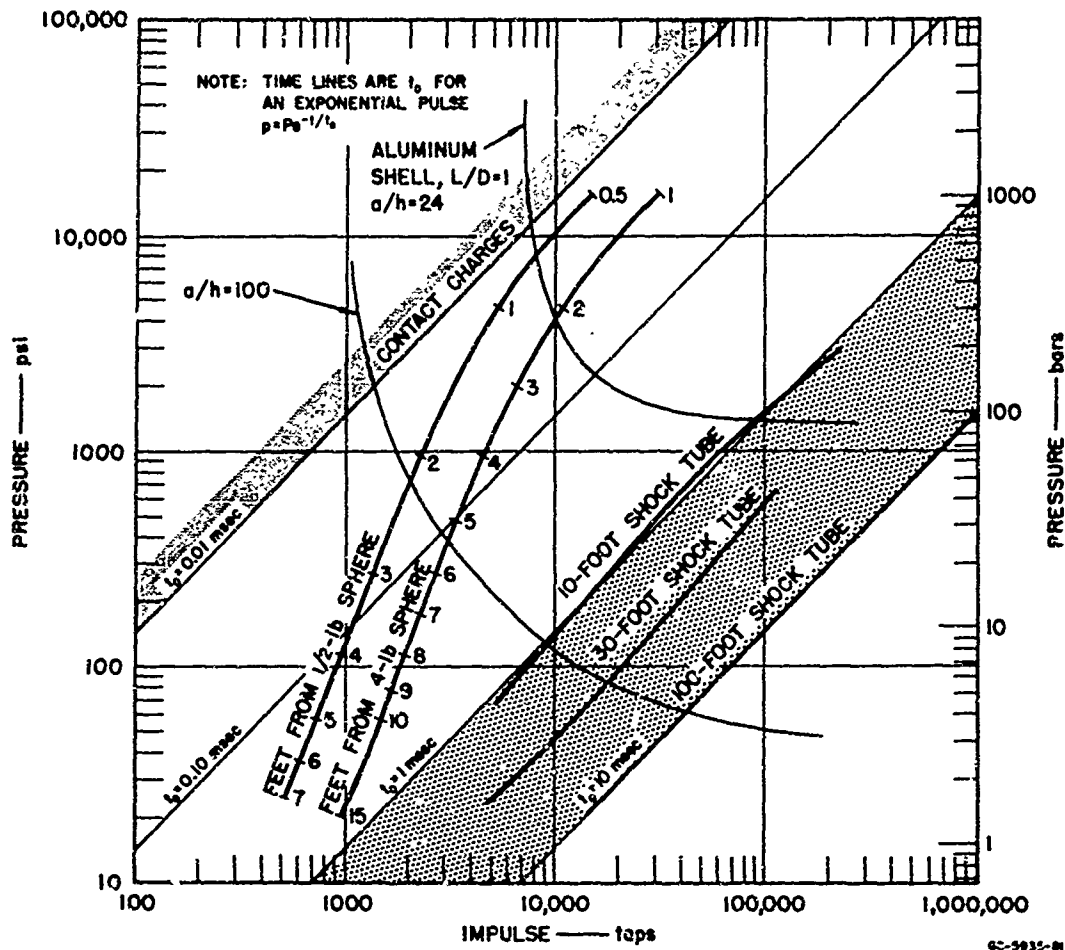


FIG. 2 PRESSURE-IMPULSE DIAGRAM FOR SEVERAL SIMULATION METHODS (for 6-inch-diameter cylinders; hyperbolic curves are buckling thresholds for 6061-T6 aluminum shells,  $L/D = 1$ )

### 3. Methods of Surface Load Simulation

The range of application of the simulation methods used in the previous programs is also shown in Fig. 2, for 6-inch-diameter models. Loads in the region of very short pulses, to the left of the  $t_0 = 0.01$  msec line, are obtained with explosive sheet or gas detonated adjacent to the model.<sup>2,3,4</sup> For loads of intermediate duration the two steep curves on the left give the peak pressure and impulse at the point of maximum pressure for side exposure to blast waves from 0.5 and 4-pound charges. The parameter varied on each curve is the distance (standoff) from the model to the charge. For long duration loads the

three curves at approximately  $45^\circ$  on the right are for side exposure to blast waves from explosively driven shock tubes<sup>1,5,6</sup> 10, 30, and 100 feet long. The parameter varied on these curves is the weight of explosive in the shock tube.

The object of the present investigation is to provide better loading methods in the intermediate region between contact loads and shock tube loads. Characteristic times in this region range over  $0.01 < t_0 < 1$  msec, a factor of 100. Since the characteristic time for a given pressure varies in direct proportion to the charge radius and hence as the cube root of spherical charge weight,<sup>\*</sup> spherical charges ranging in weight by a ratio of more than  $10^6$  would be required to cover this region. For example, at surface pressures near 2000 psi, from Fig. 2 a one-pound sphere gives  $t_0 = 0.03$  msec. To obtain  $t_0 = 1$  msec would require a charge weighing more than  $(1/0.03)^3 = 37,000$  pounds, much too large for economical use. At the other extreme, to obtain a pressure pulse at 1000 psi and the lower limit of interest,  $t_0 = 0.01$  msec, would require a charge of 0.01 pound, much too small for structural testing. Furthermore, the rapid variation of peak pressure with standoff from a spherical charge makes accurate adjustment of pressure difficult.

All of these shortcomings--excessively large charges and charges so small that they do not provide coverage of the model, and extreme accuracy requirements on standoff distance--can be overcome by using sheet charges.<sup>†</sup> In their simplest form these consist of a flat sheet of explosive suspended in air as for spherical charges. Unlike the sphere, however, at distances from the sheet small compared to its lateral dimensions the blast wave expands in only one dimension rather than in three. Thus for a fixed area, charge weight varies with the first power of the characteristic time rather

<sup>\*</sup>This simple geometric scaling applies to the pressure pulse incident upon the model. For very large charges the impulse experienced on the model would be smaller than given by this rule because of flow around the model, thus requiring a still larger range of charge weights.

<sup>†</sup>The term sheet charge is used to designate any charge in the form of a two-dimensional surface, whether it is flat, curved, or in the form of a complete cylinder. It may or may not be made of sheet explosive, a name reserved here for plasticized PETN explosive, made by Du Pont under the registered trade names Detasheet C and Detasheet D.

than the third, thereby reducing the required weight ratio from  $10^6$  to  $10^2$ . Blast loads of interest can be obtained with average explosive sheet thicknesses ranging from a few mils to something less than an inch. To maintain the lateral dimensions of the charge large compared to the standoff requires excessively large charge areas for distances greater than a few feet. At these larger distances the charge can be placed in a shock tube to maintain one-dimensional flow. At very small distances the charge must be curved partly around the model to obtain an appropriate pressure distribution and loading simultaneity; in the limit it becomes a contact charge. Thus sheet charges continuously span the load region of interest and at each extreme merge continuously with contact charge and shock tube techniques.

A pressure-impulse diagram similar to Fig. 2 can also be drawn for symmetric loads. In this case the sheet charges (both contact and standoff) take the form of cylinders completely surrounding the model, and in the shock tube the model is pointed nose-on down the tube (with a suitable nose-tip, if not already part of the model). For either symmetric or asymmetric loads on models about one foot in diameter, the characteristic times which (somewhat arbitrarily) divide contact charges, sheet blast charges, and shock tube techniques are 10  $\mu$ sec and 1 millisecond. A schematic diagram of the corresponding load regions is shown in Fig. 3. Contact techniques are limited on the left by minimum practical sheet or gaseous explosive thicknesses, and shock tube techniques are limited on the right by the economics of making very long shock tubes.

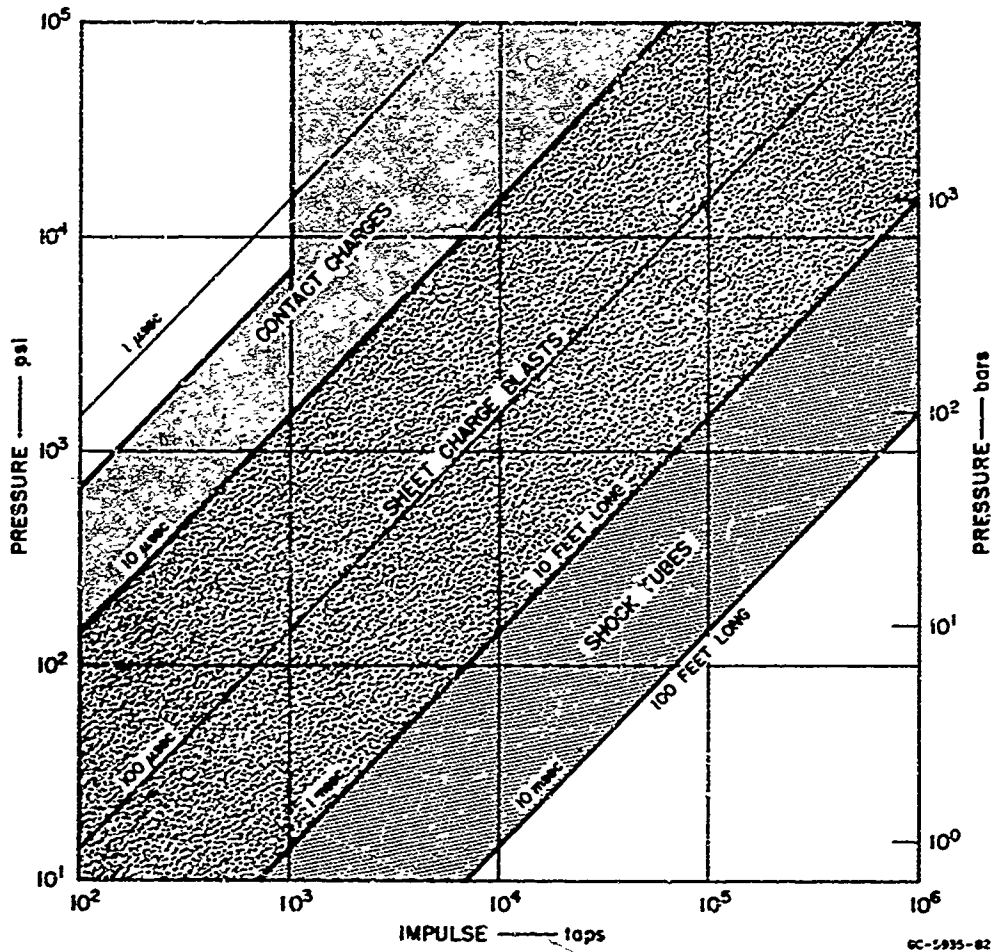


FIG. 3 LOAD REGIONS FOR BASIC SIMULATION METHODS

## SECTION II

### SUMMARY

#### 1. Theory

Using the self-similar theory of intense explosions, it is shown in Section III that blast waves from flat sheet charges have free-field pressure-time histories very similar to those from spherical charges. Thus, at these high overpressures, sheet charges give a good simulation of spherical blast waves. The theory is also used to make a quantitative comparison between the explosive required in the two geometries.

At lower pressures, further from the explosion, the self-similar theory underestimates the pressure because the energy of the ambient gas enveloped by the blast wave is neglected. Using an approximation suggested by Korobeinikov, it is shown that the decay of peak pressure with distance from the charge, taking into account the initial pressure  $p_1$  of the ambient gas, can be expressed by very simple formulas for all three geometries. Peak incident shock overpressure is given by

$$\frac{p_2}{p_1} - 1 = \frac{4\gamma}{\gamma + 1} A^2 \left[ 1 + (1 + A^{-2})^{1/2} \right] \quad (1)$$

where  $\gamma$  is the specific heat ratio of the ambient (ideal) gas and  $A$  is given by the following formulas in each geometry:

Plane Waves	$A^{-2} = 9\alpha\gamma R$	all $R$	
Cylindrical Waves	$A^{-2} = \begin{cases} 16\alpha\gamma R^2 & R \leq 2 \\ 16\sqrt{2} \alpha\gamma R^{3/2} & R \geq 2 \end{cases}$	$R \leq 2$ $R \geq 2$	(2)
Spherical Waves	$A^{-2} = \begin{cases} 25\alpha\gamma R^3 & R \leq 2 \\ 50\alpha\gamma R^2 \left[ \ln\left(\frac{R}{2}\right) + 1 \right] & R \geq 2 \end{cases}$	$R \leq 2$ $R \geq 2$	

In each case  $R$  is a dimensionless radius defined in terms of the actual radius (standoff)  $x$  by

$$R = \frac{x}{r_0} \quad , \quad r_0 = \left( \frac{E_0}{p_1} \right)^{1/\nu} \quad (3)$$

where  $\nu = 1, 2, \text{ or } 3$  in plane, cylindrical, or spherical geometry, respectively, and  $E_0$  is the energy deposited in the blast wave by the explosive, given approximately by the yield energy of the explosive per unit area, per unit length, or total energy, for  $\nu = 1, 2, \text{ or } 3$ . The parameter  $\alpha$  in Eq. (2) is a function of  $\gamma$  in each geometry; for air,  $\gamma = 1.4$  and  $\alpha = 1.075, 1.00, \text{ and } 0.85$  for  $\nu = 1, 2, 3$ . Taking  $E_0 = 1430 \text{ cal/gm}$  for 50/50 pentolite,\* Eq. (2) gives pressures within 5 percent of compiled experimental data for spherical charges to pressures as low as  $(p_2/p_1) - 1 = 0.03$ . Good agreement is also found for the plane blast waves measured here, but measured pressures extend only as low as  $(p_2/p_1) - 1 \approx 2$ .

## 2. Simulation of Asymmetric Loads

The desired range of quasi-impulsive loads was obtained with (1) flat sheet charges placed on the ground, with the model suspended above them, and (2) flat sheet charges placed in a 2-foot-diameter shock tube with the model at the open end of the tube. Standoff distances were varied from a few inches to 20 feet, and the sheet charge thickness was varied from a few mils to a few tenths of an inch. Pressure-impulse curves for these techniques are given in Fig. 4. The three uppermost curves are for charges on the ground at standoffs of 0.5, 1, and 2 feet, and the four lower curves are for charges in the shock tube at standoffs of 2.5, 5, 10, and 20 feet. The parameter varied along each curve is the density (or equivalent thickness) of the charge in pounds per square foot and in mils.

\* A mixture of PETN and TNT.

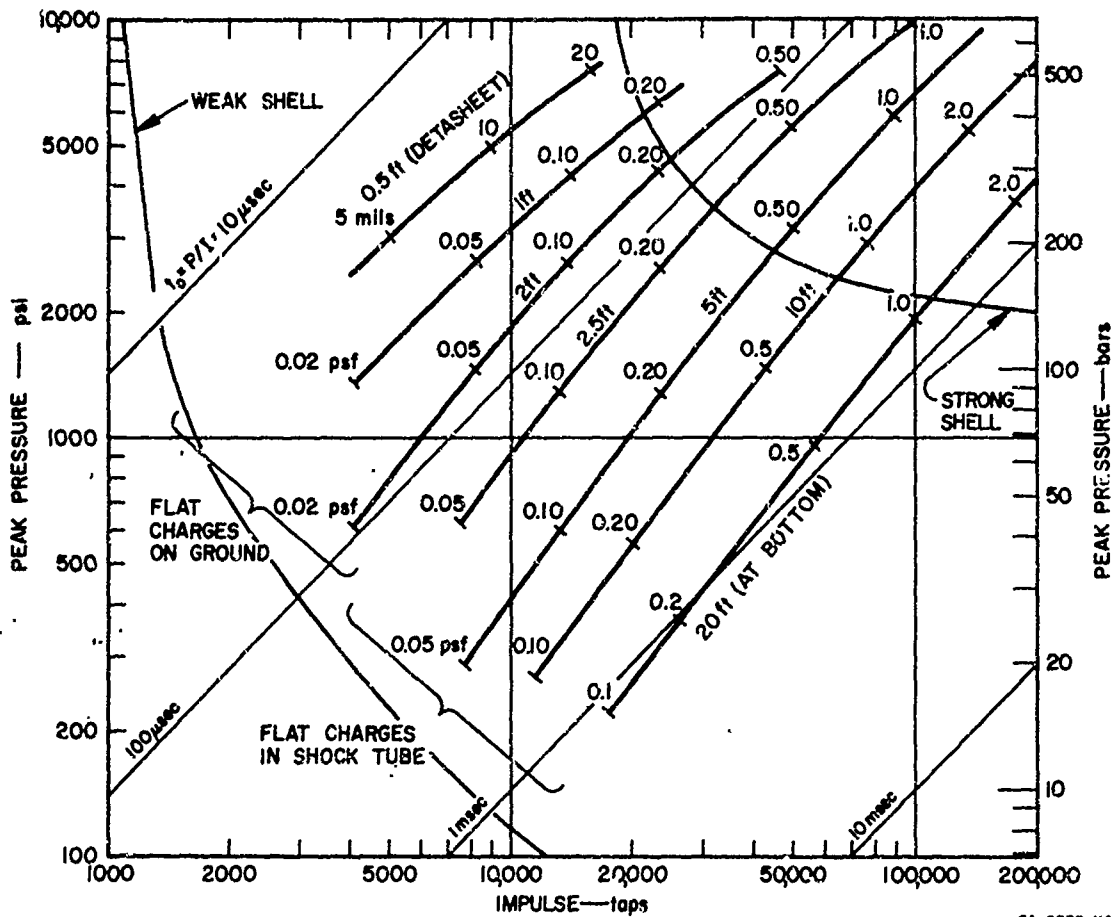


FIG. 4 PRESSURE-IMPULSE CURVES FOR ASYMMETRIC LOADING TECHNIQUES (6-inch-diameter model)

Loads were also determined for larger standoffs from charges on the ground, but the same loads can be obtained with less explosive by using the shock tube. Similarly, standoffs somewhat smaller than 2.5 feet can be used in the shock tube, but greater complications arise in initiating the charge at many points to obtain a nearly plane blast wave. (This difficulty is avoided for charges on the ground by using a running detonation, which is acceptable because there are no tube walls from which the resulting oblique shock can reflect to give undesirable secondary shocks on the model.) The crossover standoff of about 2 feet between the two techniques is satisfactorily within these limitations for the

3-inch-diameter model and 2-foot-diameter shock tube used here. Impulses at the same standoff are about 40 percent higher in the shock tube because there is no loss from lateral expansion.

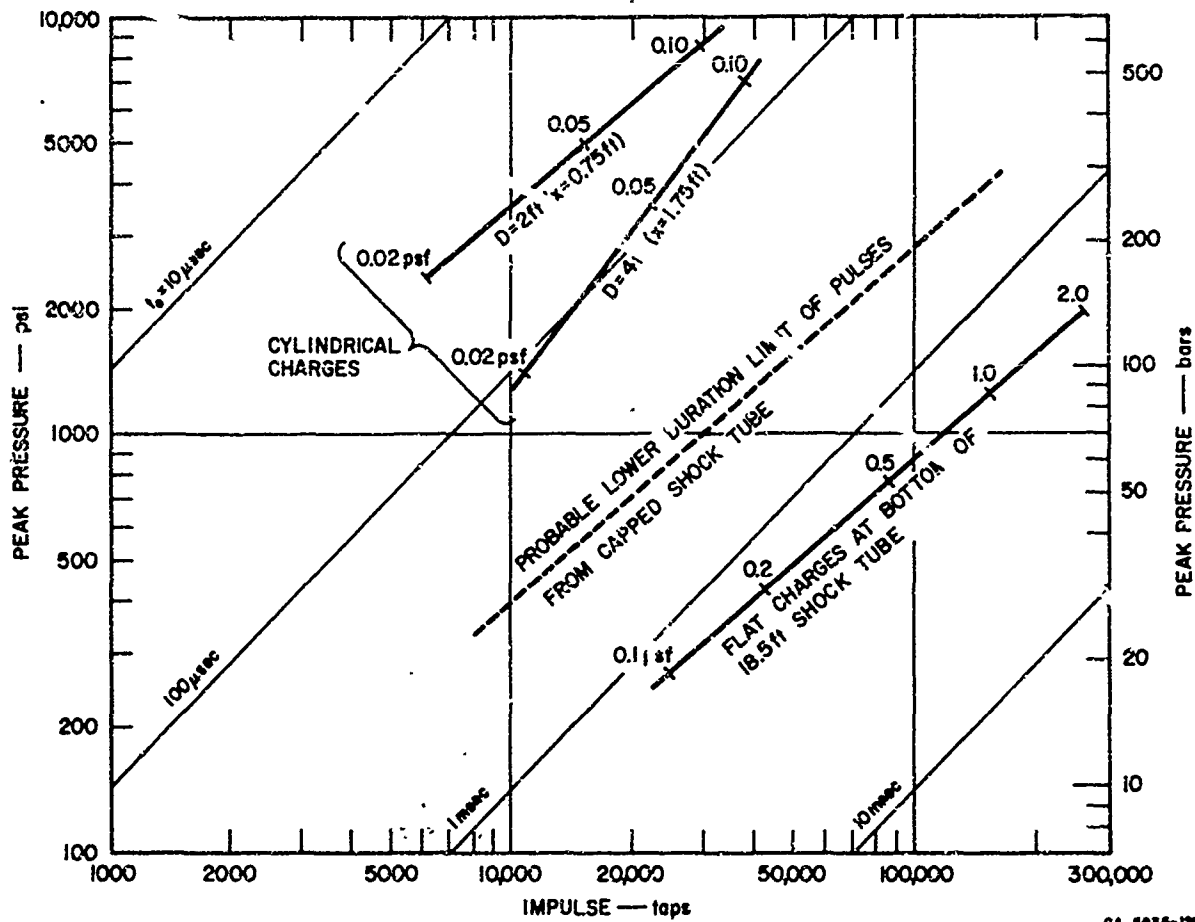
Comparison of the measured peak pressures with the self-similar theory shows that over the entire range of loads the peak pressure is the reflected pressure that would be experienced on a flat, rigid wall. Pulse shape is approximately exponential as in Fig. 1. At the larger standoffs, however, an exponential fit to the main body of the pulse gives a peak pressure of only about 70 percent of the measured initial pressure, possibly because the duration of diffraction flow is short compared to the total pulse duration. The distribution of peak pressure around the front half of the model, facing the blast, was found to be given within  $\pm 10$  percent by

$$p = (P_r - P_i) \cos^2 \theta + P_i \quad -90^\circ < \theta < 90^\circ \quad (4)$$

where  $P_r$  and  $P_i$  are the reflected and incident overpressures. Few measurements were made on the back half of the model because the pressures were very low compared to the front face pressure and mechanical gage vibrations made accurate measurement difficult. These pressures were always less than  $P_i$  and, since  $P_r \gg P_i$  for loads of interest, were considered to be of little importance for structural response.

### 3. Simulation of Symmetric Loads

Figure 5 gives pressure-impulse curves for symmetric loads obtained using (1) unconfined cylindrical charges and (2) flat charges in the shock tube with the model facing axially down the tube and backed by a plate so that the model experiences the reflected pressure propagating from the back plate. The data are less extensive than for asymmetric loads because these techniques were previously untried and the experiments were mainly exploratory. The upper two curves show that cylindrical charges 2 feet and 4 feet in diameter give loads having characteristic times near  $t_0 = 50$  and  $100 \mu\text{sec}$ . The lowermost curve shows that the shock tube gives loads having  $t_0 \approx 1500 \mu\text{sec}$  when the charge is placed at the base of the tube (standoff  $x = 18.5$  feet).



GA-5936-12

FIG. 5 PRESSURE-IMPULSE CURVES FOR SYMMETRIC LOADING TECHNIQUES (6-inch-diameter model)

Satisfactory loads having  $t_0 \approx 500 \mu\text{sec}$  could probably be obtained by placing the charge at  $x = 5$  feet in the shock tube, but still smaller standoffs could give objectionable shock decay along the length of the model and durations of the incident pressure pulse comparable to that of the reflected pulse from the model back plate. This lower limit of pulses obtainable in the capped shock tube technique is indicated by the dashed curve in Fig. 5. Pulse times from  $t_0 = 100$  to  $500 \mu\text{sec}$  would require cylindrical charge diameters larger than 4 feet, which may give difficulty in maintaining the stability of the imploding shock. Even at the 4-foot-diameter, significant variations in peak pressure around

the model were observed in the highest charge density shot. A continuing experimental and theoretical study would be required to give a range of symmetric loads comparable to the range of asymmetric loads demonstrated in Fig. 4.

#### 4. Variations in Load Distribution and Pulse Shape

A series of experiments were also performed to explore possible methods for varying load distribution and pulse shape. To vary load distribution, the technique of varying charge density around the model, which had already been demonstrated to provide variations in impulse distribution for contact charges, was applied to sheet charges at stand-offs of a few feet. It was found that charge density variations in a flat charge had little effect on pressure distribution. Density variations in a curved charge, however, had a strong effect on pressure distribution. In fact, changes in curvature (from flat to semi-cylindrical around the model) at a constant charge density also gave significant changes in pressure distribution. Using both flat and curved charges pressure distributions from  $\cos^2\theta$  to uniform over the loaded side were obtained.

Changes in pulse shape were studied for shock tube loads using volume charges of various lengths and density distributions. Flat charges (as used for Fig. 4) were found to give the most satisfactory simulation of expected high altitude pressure pulses. Charges having a stepwise variable density, most dense near the model, gave pulse shapes approaching that of the flat charge but had undesirable pressure jumps, probably caused by the discontinuities in charge density. Such charges should be used only if the stresses in the shock tube from the localized, more intense flat-charge explosions would cause tube damage.

### Section III

#### SIMULATION OF ASYMMETRIC LOADS

Asymmetric loads are more probable and tend to be more damaging than symmetric loads and are therefore treated first and more extensively. The theoretical feasibility of using sheet charges is demonstrated and then extensive measurements of pressure, impulse, and pressure distribution around cylindrical models are given for free expansion from flat charges and for flat charges suspended in a two-foot-diameter shock tube.

##### 1. Theoretical Pressure Pulses

Before describing the experimental results it is helpful to make a theoretical estimate of sheet charges required for the desired pressure pulses and compare them with the corresponding spherical charges. This can be done using the theory of blast waves from intense explosions given in Section VI. Near the explosion the self-similar theory gives the following expressions for peak incident pressure  $p_i$  and time scale  $t_{fv}$ :

$$\frac{p_i}{p_1} = \frac{8R_v^{-\nu}}{\alpha_v (2 + \nu)^2 (\gamma + 1)} \quad (5)$$

$$t_{fv} = \left( \frac{\alpha_v \rho_1}{p_1} \right)^{1/2} s_{\nu} R_v^{\frac{\nu+2}{2}} \quad (6)$$

where  $p_1$  and  $\rho_1$  are the pressure and density of the undisturbed ambient gas ahead of the shock,  $\gamma$  is the specific heat ratio,  $\nu$  is an index having values  $\nu = 1, 2,$  and  $3$  in plane, cylindrical, and spherical blast waves, and  $\alpha_v$  is the corresponding constant. The distance from the center of the charge to the shock front is denoted here by  $x_v$  and in Eqs. (5) and (6) appears in the dimensionless form

$R_v$ , normalized to a characteristic length in each geometry according to\*

$$R_v = \frac{x_v}{s_v}, \quad s_v = \left( \frac{E_v}{p_1} \right)^{1/v} \quad (7)$$

In each geometry  $E_v$  is the effective release energy of the charge, having units of energy per unit area in plane geometry, energy per unit length in cylindrical geometry, and total energy of the charge in spherical geometry.

a. Comparison of Spherical and Plane Blast Waves

We first compare the incident pressure pulse shapes from plane and spherical charges. These are shown in Fig. 6, taken from Fig. 52a with the time scale for the plane wave compressed by a factor of 2 to give close agreement at early times. With this modification, the two pulses are nearly identical until  $p/p_1$  falls below 0.2. At later times the pressure decays more slowly for the plane wave, but the difference is not great and effects not treated in the self-similar theory would tend to make the pulses more nearly the same. Similar comparisons of the density, particle velocity, and dynamic pressure behind the shock can also be made; these again show some differences between the two waves but the similarity is close enough that plane blast waves give a good simulation of spherical blast waves.

Knowing that the pulse shapes are similar, we can now compare the charge weights and standoff distances  $x_v$  for plane and spherical blast waves that give the same peak pressure and duration. Equating peak pressures from Eq. (5) gives

$$R_1 = \frac{25\alpha_3}{9\alpha_1} R_3^3 = 2.16 R_3^3 \quad (8)$$

in which  $\alpha_1 = 1.075$  and  $\alpha_3 = 0.85$  have been taken for  $\gamma = 1.4$  as

\*The notation here is slightly changed from that in Section VI because waves of different geometries are being compared; a subscript  $v$  is used here and  $r_0$  is replaced by  $s_v$  to avoid confusion.

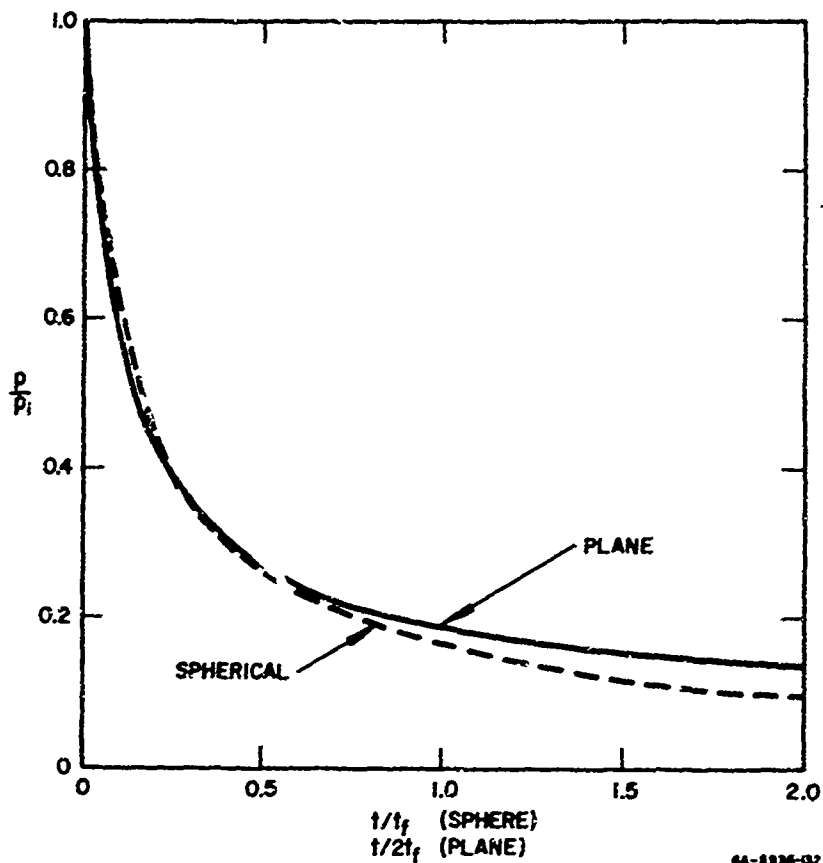


FIG. 6 INCIDENT PRESSURE PROFILES FROM SELF-SIMILAR THEORY

discussed in Section VI. From Fig. 6 the durations are made comparable by taking  $2t_{f1} = t_{f3}$ . Using this in Eq. (6) results in

$$2\alpha_1^{1/2} s_1 R_1^{3/2} = \alpha_3^{1/2} s_3 R_3^{5/2} \quad (9)$$

Combining this with Eq. (8) yields

$$s_1 = \frac{1}{2} \left( \frac{27}{125} \right) \frac{\alpha_1}{\alpha_3} s_3 R_3^{-2} = \frac{0.137}{2} \frac{s_3^3}{x_3} \quad (10)$$

From the definition of  $s_v$  in Eq. (7),  $s_1$  is proportional to the thickness of the sheet charge (weight per unit area) and  $s_3$  is proportional to the radius of the spherical charge ( $s_3^3$  is proportional to

the total charge weight). In these terms Eq. (10) becomes

$$w_1 = \frac{0.137}{x_3^2} W_3, \quad \text{or} \quad W_3 = 81 x_1^2 w_1 \quad (11)$$

where  $w_1$  is weight per unit area of the sheet charge and  $W_3$  is total weight of the spherical charge. Combining Eqs. (8) and (10) with the definition of  $R_v$  from Eq. (7) gives

$$x_1 = \frac{3}{10} x_3 \quad (12)$$

Equations (11) and (12) are the desired relations between charge sizes and model-to-charge distances and are applicable for pressure pulses in the range of approximate validity of the self-similar approximation. This range is rather narrow ( $5 \lesssim p_i/p_1 - 1 \lesssim 50$ ), but the corresponding range in reflected pressure with  $p_1 = 14.7$  psi is  $300 \lesssim p_r \lesssim 5000$  psi, which happens to be the range in which many structural models of interest are damaged. Also, since Eqs. (11) and (12) are comparative, their range of validity is probably somewhat larger than the range of absolute accuracy of the self-similar theory. From Eq. (12) we see directly that the space required for a sheet charge experiment is inherently less than that required for a spherical charge, the standoff distance being only 30 percent of that for a spherical charge. From Eq. (11) we see, as expected, that at large distances (long durations) a great savings in weight can be achieved by using one-dimensional blast waves.

#### b. Estimates of Sheet Thickness and Standoffs

As discussed in Section I, the model pulse characteristic times for which sheet charges appear attractive are in the range  $10^{-5} < t_0 < 10^{-3}$  sec. Using the self-similar theory, the range of sheet charge thicknesses and standoff distances required to give these characteristic times for the incident pressure pulses can be estimated. The theory will also prove valuable later in interpreting peak pressure measurements in the experiments.

As the experiments will show, the peak pressure experienced on the model is the reflected pressure  $p_r$  corresponding to the incident pressure  $p_i$ . Figure 7 gives a plot (taken from Section VI) of  $p_i$  and  $p_r$  versus  $R$  for flat charges, using the self-similar theory for small  $R$  and an asymptotic theory for large  $R$ . To obtain a model overpressure ratio of 200 (giving a pressure of about 3000 psi at sea level) Fig. 7 requires that  $R_1 = 0.012$ . The explosive thickness to produce this pressure at various incident pressure durations can be calculated from Eq. (6). We first use definition (7) to obtain

$$s_1 = h \frac{Y}{p_1} \quad (13)$$

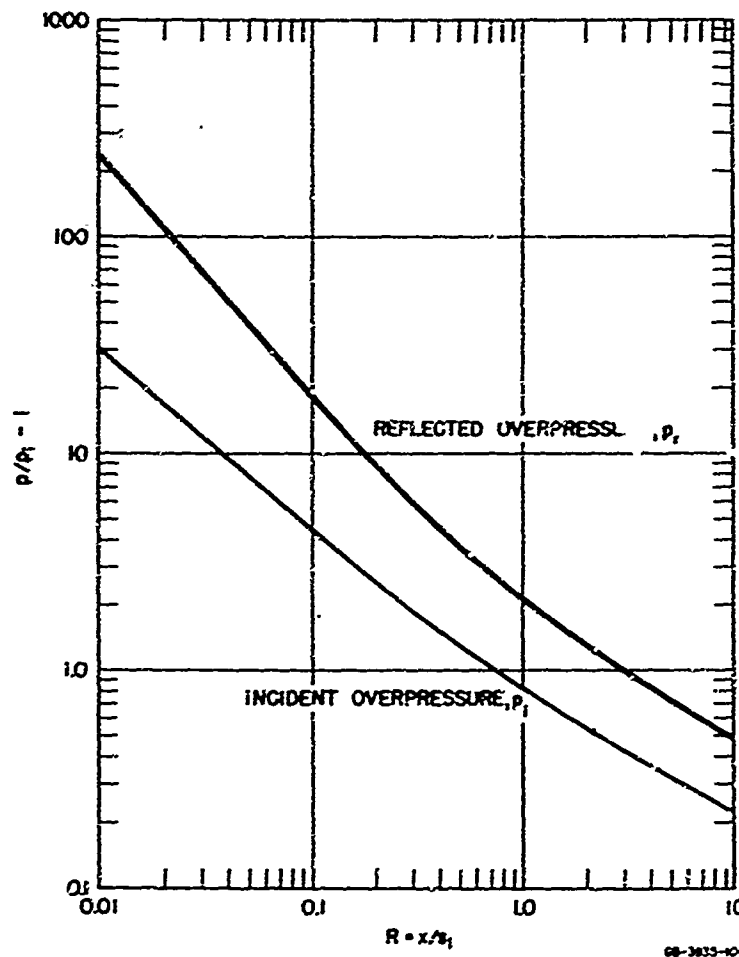


FIG. 7 INCIDENT AND REFLECTED OVERPRESSURES FROM SHEET BLAST WAVES

where  $h$  is the explosive thickness and  $Y$  is its effective release energy per unit volume. PETN has an energy release of about 1600 cal/gm which, at a  $1.4 \text{ gm/cm}^3$  density, gives  $Y \approx 10^{11} \text{ ergs/cm}^3$ . Substituting Eq. (13) into Eq. (5) gives for the explosive thickness

$$h = \frac{p_1}{Y} \left( \frac{p_1}{\alpha_1 \rho_1} \right)^{1/2} \frac{1}{R_1^{3/2}} t_{fl} \quad (14)$$

Comparison of Figs. 1 and 6 shows that to a reasonable approximation  $t_{fl}$  for plane blast waves can be used as the equivalent exponential characteristic time  $t_0$ . Thus we can substitute  $10^{-5} \lesssim t_0 \lesssim 10^{-3}$  directly into Eq. (14) with  $p_1 = 10^6 \text{ dyne/cm}^2$ ,  $\rho_1 = 1.293 \times 10^{-3} \text{ gm/cm}^3$ ,  $Y = 10^{11} \text{ ergs/cm}^3$ , and  $R_1 = 0.012$  to obtain the range for  $h$  at this pressure:

$$0.0020 \lesssim h \lesssim 0.20 \text{ cm} \quad (15)$$

To obtain the corresponding standoff distances, we use Eqs. (7) and (13) to get

$$x = R_1 h \frac{Y}{p_1}$$

which, with Eq. (15), yields

$$2.4 \lesssim x \lesssim 240 \text{ cm} \quad (16)$$

Since the characteristic times of the diffracted pressures measured on cylindrical models are somewhat less than the incident times (about half, and decreasing with increasing standoff, as we shall see) Eqs. (15) and (16) give lower bounds on the required values. Doubling these values we obtain standoff distances from about 2 inches to 20 feet and explosive thicknesses from about 2 mils to 0.2 inch. These ranges can be reasonably obtained experimentally. The lower limit of 2 mils for explosive thickness cannot be obtained in a continuous sheet, but thin extruded rods of explosive can be used to give an average

thickness of 2 mils at a spacing small compared to the 2-inch standoff. At pressures appreciably below the 3000 psi example here, however, gaseous explosives would have to be used to maintain durations as short as 10  $\mu$ sec.<sup>2,3</sup> The upper limit of  $x = 20$  ft requires a shock tube to maintain one-dimensional flow, as already observed in Section I.

By comparison, the spherical charges corresponding to the range of flat charges in Eq. (15) and (16) become impractical at each extreme. Using Eqs. (11) and (12) and an explosive density of 1.4 gm/cm<sup>3</sup>, the range of spherical charge weights and standoffs are

$$1.30 < W_3 < 1.30 \times 10^6 \text{ gm} \tag{17}$$

$$8 < x_3 < 800 \text{ cm}$$

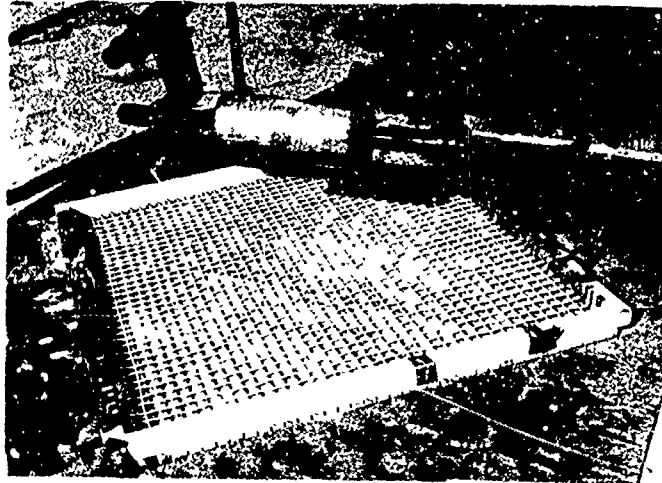
## 2. Experimental Arrangements

### a. Model Support and Charge Layout

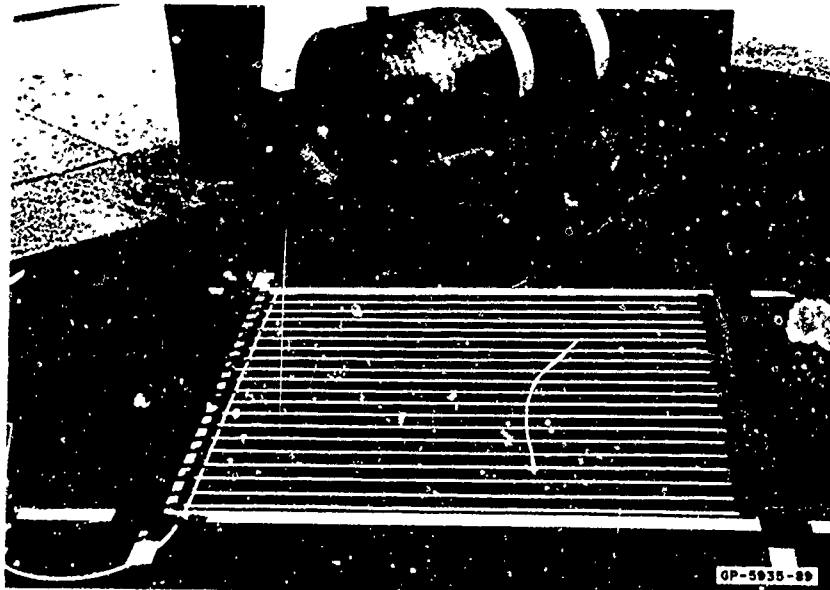
The general arrangement typical of most of the field experiments is shown in Fig. 8. The charges are layed on a one-inch-thick steel plate resting on a bed of sand. Considering the plate as a rigid wall, this doubles the effective yield of the explosive as compared to expansion from a charge freely suspended in air. The model is held in a stand large enough to be used over charges 12 feet square. Standoff is adjusted by raising or lowering the entire cross frame. Coarse adjustment is made by sliding the frame over the four pipe legs; fine adjustment is made by telescoping screw jacks at the base of each leg.

The charges in Fig. 8 are all made of Primacord,<sup>\*</sup> which consists of PETN packed in a polyethylene sheath and textile braid. Primacord was used for most of the shots because it is relatively inexpensive (about \$3 per pound of core loading) and is readily available from local suppliers in sizes from 25 to 400 grains of PETN per foot. Detasheet explosive is conceptually more desirable than Primacord because it comes in sheet form and can be rolled to any desired thickness greater than 15 mils, the limit for reliable detonation. However, Detasheet is

<sup>\*</sup> Primacord is a registered trademark of the Ensign Bickford Company.



(a) WOVEN PRIMACORD

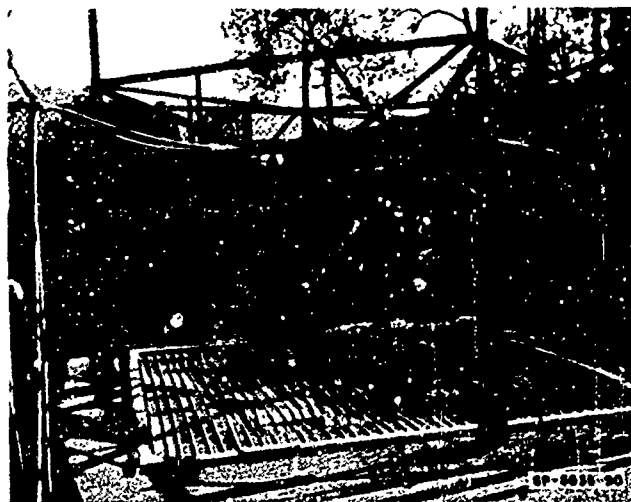


(b) PARALLEL STRANDS

FIG. 8 EXPERIMENTAL ARRANGEMENT FOR FLAT CHARGE  
FIELD EXPERIMENTS



(c) 1-FOOT STANDOFF



(d) 4-FOOT STANDOFF

FIG. 8 (Concluded)

is relatively expensive (about \$10 per pound for Detasheet C and \$25 per pound for Detasheet D) and must be ordered several months in advance. Detasheet was therefore used only for equivalent sheet thicknesses and standoffs too small to be obtained with Primacord. The very lightest charges were made using Detasheet D extruded into 0.028-inch-diameter rods weighing about 4 grains/ft.

The majority of the charges were made of parallel strands of Primacord as in Fig. 8b with a single cross strand (at the left in the figure) for detonation. Early in the program a few charges were made by weaving Primacord as in Fig. 8a to increase detonation reliability. These are time consuming to make and the single strand method of detonation proved just as reliable so woven charges were discontinued. In the parallel strand configuration, the charge weight per unit area is

$$w \text{ (psf)} = \frac{12 \text{ in./ft}}{7000 \text{ grains/lb}} \cdot \frac{g \text{ (grains/ft)}}{S \text{ (in.)}} \quad (18)$$

where  $g$  is the Primacord size and  $S$  is the strand spacing. For a given charge density  $w$ , the Primacord size and strand spacing can generally be chosen small enough that the charge appears as a continuous sheet at the model standoff. No detailed investigation of the maximum allowable strand spacing was made. Instead, a spacing rule was adopted that allowed reasonable shot assembly and then a few shots were fired at coarser spacing for comparison.

The spacing rule is

$$\frac{x}{S} = 16$$

where  $x$  is the standoff distance between the charge and the closest point on the model. This rule insures that the strength of the cylindrical shocks from individual strands at radius  $S/2$  where they first intersect (see Fig. 9), is large compared to the overall "plane" shock arriving at standoff  $x$ . From Eq. (43) for  $\nu = 2$ , the cylindrical shock pressure at  $S/2$  within the self-similar approximation is

$$p_s = \frac{8}{\alpha_2^2 (4)^2 (\gamma + 1)} \frac{E_2}{(S/2)^2} = \frac{8}{\gamma + 1} \cdot \frac{G}{4\alpha_2 S} \quad (19)$$

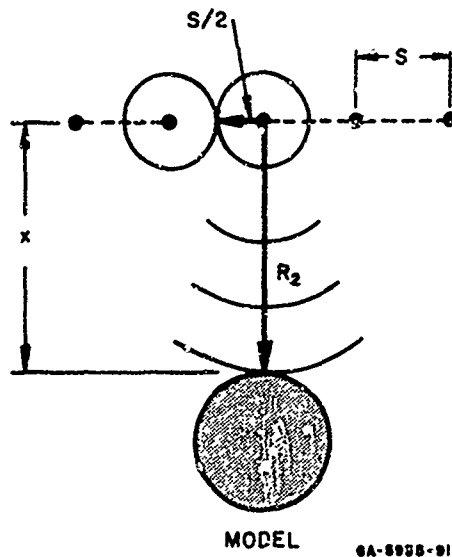


FIG. 9 SHOCK RADII FROM INDIVIDUAL STRANDS AND FROM CHARGE AS A CONTINUOUS SHEET

where  $G$  is the energy release per unit length of Primacord explosive. Similarly, the plane shock pressure at  $x$  is

$$p_x = \frac{8}{\alpha_1 (3)^2 (\gamma + 1)} \frac{E_1}{x} = \frac{8}{\gamma + 1} \cdot \frac{G}{9\alpha_1 Sx} \quad (20)$$

in which we have used  $E_1 = G/S$ . The pressure ratio is

$$\frac{p_s}{p_x} = \frac{9\alpha_1}{4\alpha_2} \cdot \frac{x}{S} = 2.42 \frac{x}{S} \quad (21)$$

For  $x/S = 16$ ,  $p_s/p_x = 39$ .

Another interpretation of fixing  $x/S$  at a large value is that it makes the pressure  $p_2$  arriving at  $x$  from each strand, if it were to act individually, small compared to the effective overall plane shock. Within the self-similar approximation,  $p_2$  is found by replacing  $S/2$  in Eq. (19) by  $x$ :

$$p_2 = \frac{8}{\gamma + 1} \cdot \frac{G}{16\alpha_2 x^2}$$

Then

$$\frac{p_2}{p_x} = \frac{9\alpha_1 S}{16\alpha_2 x} = 0.61 \frac{S}{x} \quad (22)$$

For  $x/S = 16$ ,  $p_2/p_x = 0.038$ . This result is changed only slightly if the more accurate expressions in Eq. (60), taking into account the ambient pressure  $p_1$ , are used to calculate  $p_2$  and  $p_x$ . Many experiments were also run with  $x/S = 8$ , and smoothly decaying model pressure pulses were recorded. It was concluded that  $x/S = 16$  is a conservative spacing rule and that spacings at least as coarse as  $x/S = 8$  can also be used where the minimum available explosive size does not allow  $x/S = 16$ .

Figure 10 gives a loading chart for  $x/S = 16$  and currently available Primacord sizes. The points indicate configurations for which experiments were run in the current program. Since 50 and 25 grain/ft sizes have only recently become available, load points for these sizes were run using 40 grain/ft Primacord at  $x/S = 20$  and  $x/S = 10$ . Charge densities used ranged in multiples of 2 from 0.0143 psf to 0.456 psf. Corresponding Detasheet thicknesses for the same amount of PETN can be calculated using a PETN density of  $1.12 \text{ gm/cm}^3$ , which is 30 percent of the total  $1.4 \text{ gm/cm}^3$  Detasheet density. The resulting Detasheet thicknesses range from 2.5 to 78 mils. It is probable that the coarser strand spacing rule  $x/S = 8$  could also be used, extending the lower limit of available charge densities by shifting the curves down by a factor of 2.

#### b. Charge Size

In the foregoing theory, it has been assumed that the flat charge is infinite in extent. To estimate the effect of finite charge size on peak pressure and impulse, a series of experiments were run using rectangular charges as in Fig. 8 with sides of lengths  $b$  in the ratio  $b/x = 1, 2, \text{ and } 3$  relative to the standoff. Three series were run, one with  $x = 2$  feet and  $w = 0.114$  psf, one with  $x = 2$  feet and  $w = 0.456$  psf, and one with  $x = 4$  feet and  $w = 0.114$  psf. The averages of the

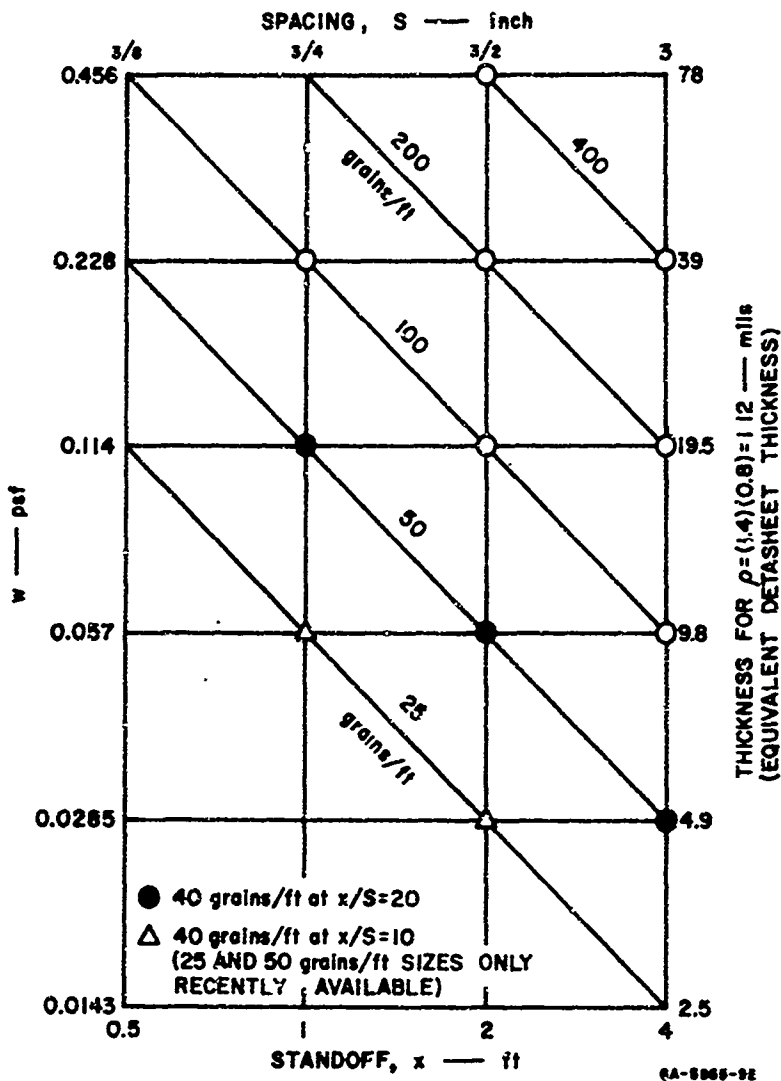


FIG. 10 PRIMACORD LOADING CHART FOR  $x/S = 16$  (points are shots fired in present program)

data from all three sets of experiments are plotted in Fig. 11, with pressure and impulse (at  $\theta = 0^\circ$ , facing the blast) normalized to their values for  $b/x = 2$ . The data show that the increase in pressure and impulse in going from  $b/x = 2$  to  $b/x = 3$  is small, and suggest that even at  $b/x = 2$  the pressure is within about 10 percent of its infinite sheet value and impulse is within about 30 percent. Both decrease rapidly as  $b/x$  falls below 2. In the remainder of the experiments

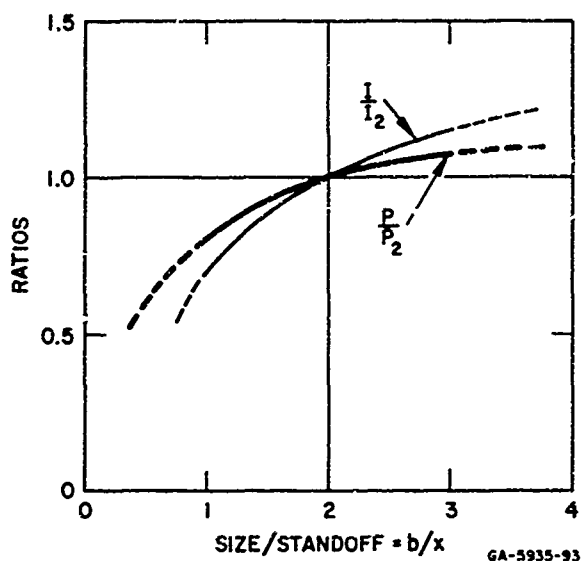


FIG. 11 PRESSURE AND IMPULSE VERSUS CHARGE SIZE/STANDOFF

$b/x$  was therefore fixed at 2.\* Comparison of the absolute magnitudes of the pressures and impulses with the infinite sheet theory is deferred until later.

c. Shock Path and Model Orientation

In addition to the charges being of finite size, they also differed from the simple one-dimensional theory because they were not detonated simultaneously over their entire area. Instead, a single detonator was placed in one corner (see Fig. 8) and detonation took place along a diagonal line sweeping over the charge.† At some distance from the charge the shock angle is sufficiently shallow that the one-dimensional theory is adequate. Figure 12 shows the apparent shock paths,

\* At  $x = 1$  with large charge densities, a diagonally detonating charge gave pressures lower than predicted and also a humped pressure profile because of the diamond shape of the charge. Data from these charges were therefore deleted in favor of the sheet explosive charges to be described next.

† Detonation proceeds at  $7 \text{ mm}/\mu\text{sec}$  along each Primacord strand, parallel to the side of the charge. Since each successive strand is initiated at a slightly later time by the edge strand running at right angles, the effective detonation front moves parallel to a diagonal at velocity  $7 \cos 45^\circ = 5 \text{ mm}/\mu\text{sec}$ .

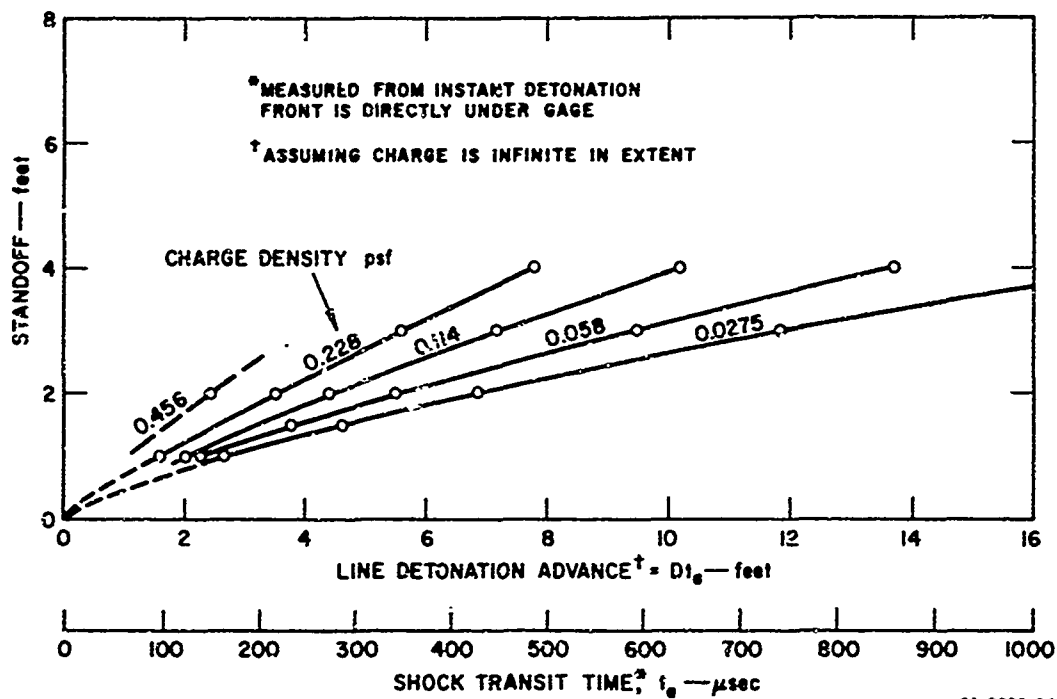


FIG. 12 SHOCK TRANSIT TIMES AND APPARENT SHOCK PATHS FOR DIAGONALLY DETONATING PRIMACORD CHARGES

obtained from accumulated data on shock transit time to the model from the time the detonation passes the center of the charge. These are not strictly the shock paths because in each shot the measurement was made after the entire charge had detonated--we do not have a steady detonation, so time and distance cannot be interchanged. However, since Fig. 11 indicates that the peak pressure is near the infinite sheet pressure, the curves in Fig. 12 give a good indication of the shock paths. Shock angles at the model range from about 25 degrees at small distances from heavy charges to about 10 degrees at large distances from light charges.

Two orientations of the model relative to the shock path were studied, transverse and longitudinal, as sketched in Fig. 13. Each method has advantages. In the transverse placement the shock arrives simultaneously along the length of the model at normal incidence to an angle  $\theta_0$ , giving the maximum possible peak pressure and minimizing end effects. In the longitudinal orientation the shock arrives at angle  $\theta_0$  relative to the model axis, giving lower peak pressure and aggravating

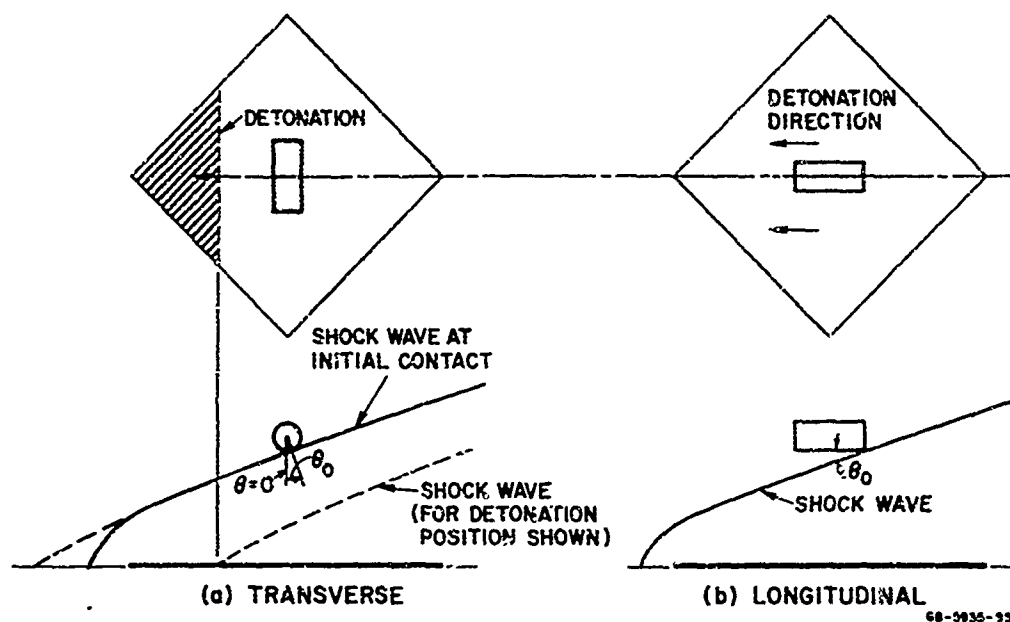


FIG. 13 SHOCK IMPINGEMENT FOR TRANSVERSE AND LONGITUDINAL MODEL ORIENTATIONS (both drawn for  $x = 2$  feet and  $w = 0.114$  psf)

possible longitudinal variation of pressure because of end effects. These disadvantages were found to be minor and the advantage of knowing that the pressure distribution is symmetric about  $\theta = 0$ , without prior knowledge of  $\theta_0$ , was considered to be more important in the present program. The majority of the experiments were therefore run in the longitudinal orientation to avoid having to adjust the pressure gage orientation to  $\theta = \theta_0$  (the slopes  $\theta_0$  of the curves in Fig. 12 were not known at the outset of the program). Longitudinal detonation also gives a continuous transition to the contact techniques, which also use a detonation sweeping along the model axis. In studying methods for modifying pressure distribution, longitudinal detonation is almost imperative to insure symmetric pressure distributions.

#### d. Sheet Explosive Charges

Charges made from Detasheet were used only at small standoffs, at which the range of equivalent sheet thicknesses available from Primacord is limited (see Fig. 10). To reduce the shock angle as much as possible at these standoffs, Detasheet charges were oriented with their sides parallel to the model axis as in Fig. 14 so that the detonation

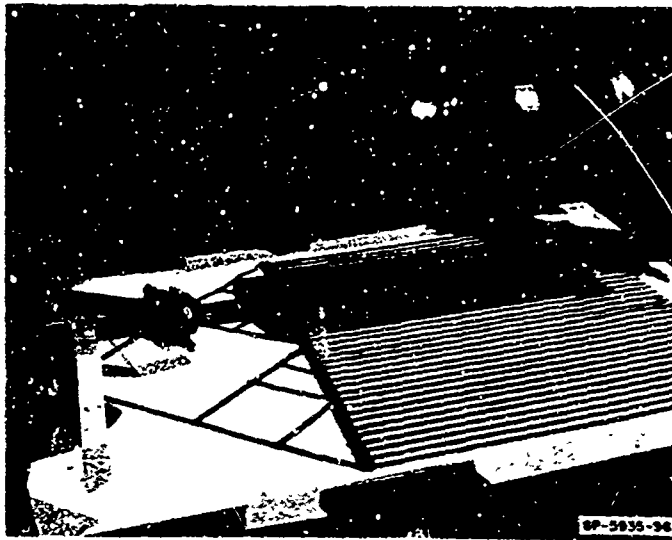


FIG. 14 DETASHEET CHARGE

wave swept along the charge at the full detonation velocity of 7.3 mm/ $\mu$ sec. Also, at small standoffs, the size of the model, rather than the magnitude of the standoff, dominates charge size and  $b/x$  must be made larger than 2. For 0.5 foot and 1-foot standoffs, the charges were made with  $b/x = 3$ .

Figure 15 is the loading chart used for sheet explosive. For sheet thicknesses greater than 30 mils, solid sheets of Detasheet C can be used. At smaller thicknesses Detasheet D must be used because Detasheet C does not detonate well below 30 mils. For the same reason, below 15 mils Detasheet D was cut into strips and spaced apart with a spacing rule of  $x/S = 12$  where possible, and with  $x/S = 6$  for smaller average thicknesses. For still lower loads, 38-mil-diameter extruded rods were used; the lowest loads were obtained using 28-mil-diameter rods, the smallest cross section that will detonate. At a standoff of 3 inches the smallest obtainable average thickness is about one mil.\*

\* Pressure and impulse data from the 3-inch standoff shots are not reported because they were not extensive enough to allow comprehensive treatment.

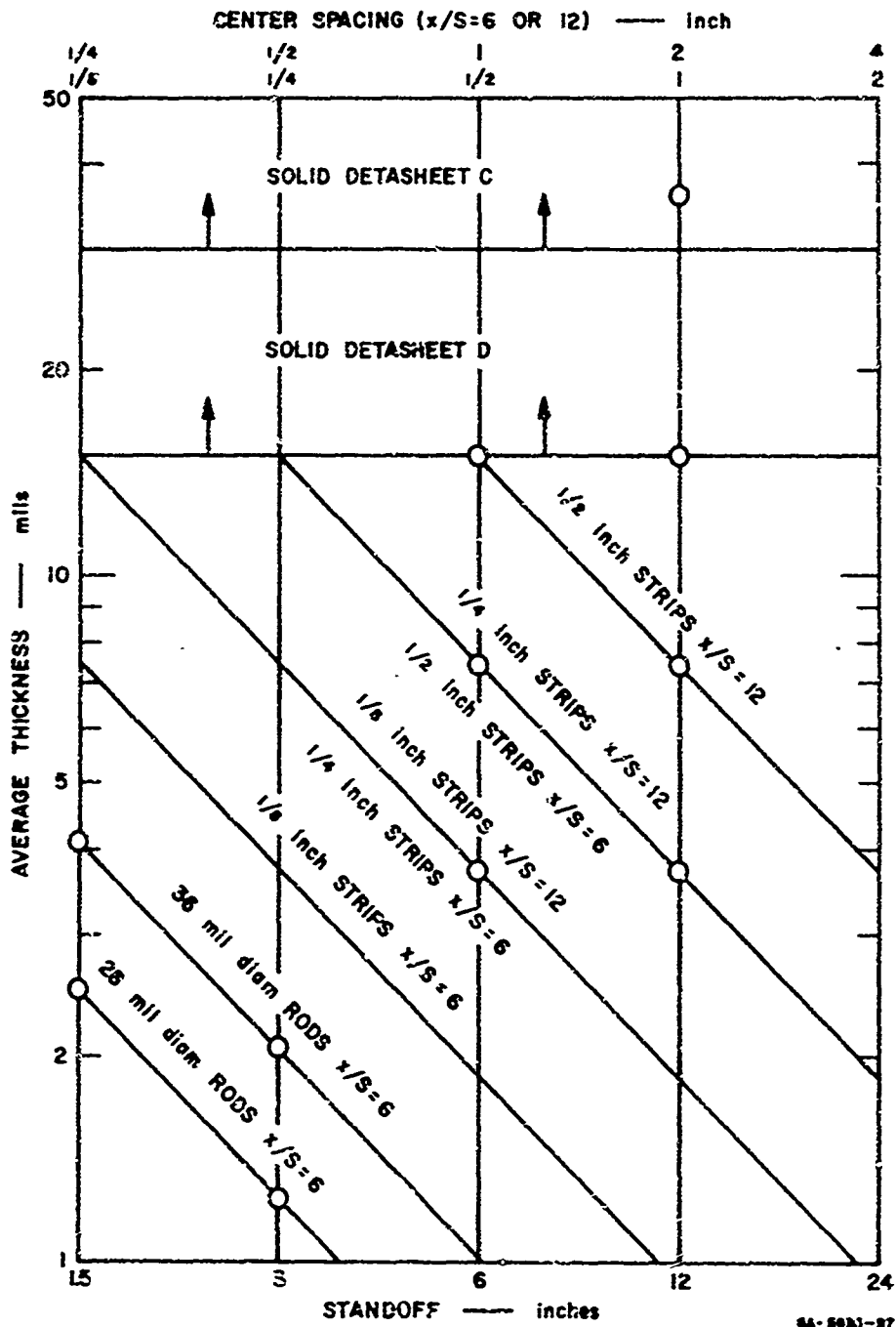


FIG. 15 SHEET EXPLOSIVE LOADING CHART (strips are all 15-mil-thick Detasheet D; points are shots fired in current program)

#### e. Other Charge Configurations

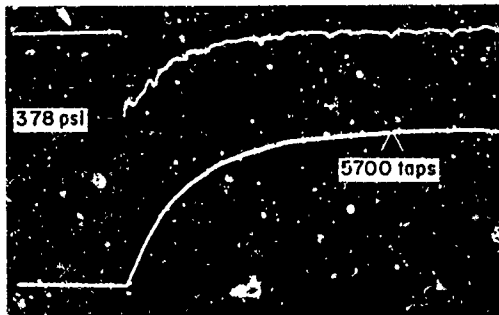
To investigate methods for modifying the pressure distributions from those obtained with the flat charges described above, curved charges and charges of nonuniform density were also used. These are described in Sections IV and V.

#### 3. Surface Loads from Flat Primacord Charges

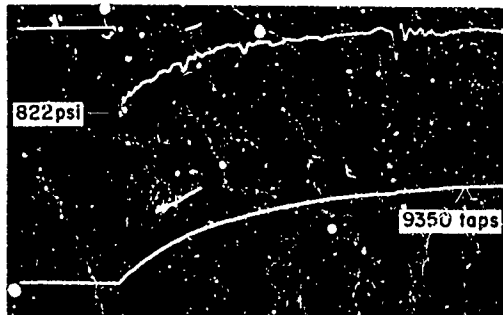
In this section we will examine the pulse shape, pressure distribution, peak pressures, and impulses from Primacord charges at  $x = 1$ , 2, and 4 feet. In the majority of the experiments the model cylinder was steel, 6 inches in diameter and 15 inches long with a 1-inch wall thickness. Pressure was measured with Kistler model 601H and 603H gages. To measure circumferential pressure distributions, gages were mounted at the center of the model at 22.5 degree intervals over one-half of the circumference and at 45 degree intervals over the other half. Possible axial variations in pressure were measured with gages mounted 3 inches in from each end, giving 3 gages in all at  $\theta = 0$  (facing the blast). These are denoted by  $O_1$ ,  $O_{mid}$ , and  $O_2$ , in the order in which the blast sweeps over the model as seen in Fig. 13b. In Section III.6 data are given from 3.5- and 12-inch-diameter models instrumented in a similar manner. Further details of the models and pressure instrumentation are given in Reference 1.

#### a. Pulse Shape

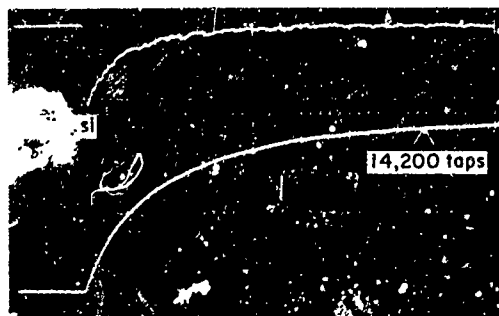
As in the pressure pulses measured from explosive spheres,<sup>1</sup> surface pressure pulses from sheet charges are very nearly exponential in shape. Example pulses are given in Fig. 16 for  $x = 4$  feet with  $w$  ranging from 0.0275 to 0.228 psf, and in Fig. 17 for  $x = 2$  feet and 1 foot at the extremes in  $w$ . In Fig. 18 a pressure record typical of those in Figs. 16 and 17 is plotted on semi-log paper to show the closeness to an exponential decay. The measured pressure in this record does not differ from an exponential until it has decayed to about 1/6 of its initial value.



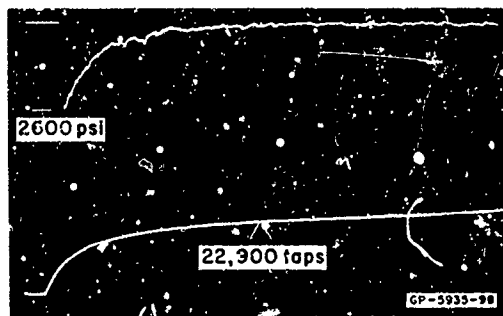
(a)  $w = 0.0275$  psf, SHOT FP-69  
SWEEP RATE:  $200 \mu\text{sec/cm}$



(b)  $w = 0.055$  psf, SHOT FP-68  
SWEEP RATE:  $100 \mu\text{sec/cm}$



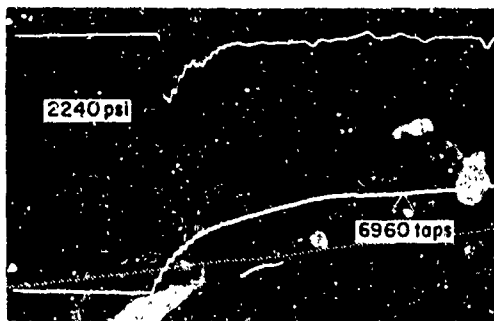
(c)  $w = 0.114$  psf, SHOT FP-70  
SWEEP RATE:  $100 \mu\text{sec/cm}$



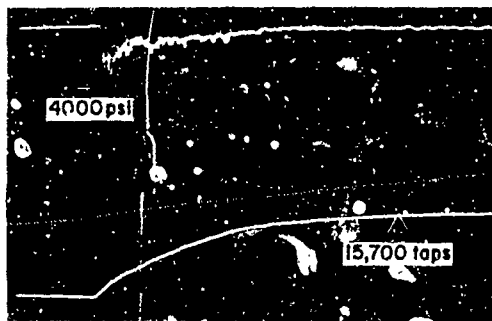
(d)  $w = 0.228$  psf, SHOT FP-71  
SWEEP RATE: UPPER  $100 \mu\text{sec/cm}$   
LOWER  $200 \mu\text{sec/cm}$

FIG. 16 PRESSURE PULSES AT  $\theta = 0_{mid}$  FROM FLAT PRIMACORD CHARGES AT  $x = 4$  FEET (upper traces pressure, filtered at 120 kc; lower traces integrals, unfiltered)

Because of this exponential behavior, semi-log pressure plots were used to extrapolate back to the "true" peak pressure  $P$  (3000 psi in the example) from the highest pressure the gage was able to record within the frequency band limitation of the gage and signal filter. Direct and extrapolated pressures were generally within 15 percent of each other. Impulse was measured by electronically integrating the pressure signal. These are the lower traces in Figs. 16 and 17.

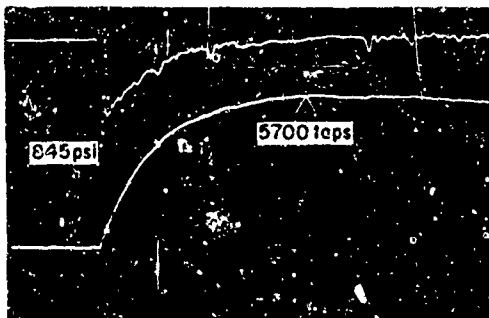


(a)  $w = 0.055$  psf, SHOT FP-61

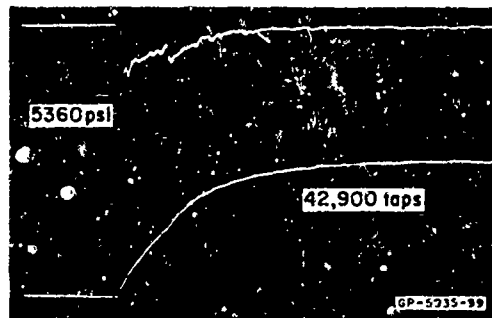


(b)  $w = 0.228$  psf, SHOT FP-119  
PRESSURE UNFILTERED

1-FOOT STANDOFF (SWEEP RATE  $50\mu\text{sec/cm}$ )



(c)  $w = 0.0275$  psf, SHOT FP-65



(d)  $w = 0.456$  psf, SHOT FP-74

2-FOOT STANDOFF (SWEEP RATE  $100\mu\text{sec/cm}$ )

FIG. 17 PRESSURE PULSES AT  $\theta = 0_{\text{mid}}$  FROM FLAT PRIMACORD CHARGES  
AT  $x = 1$  FOOT AND 2 FEET

b. Pressure Distribution

Figure 19 gives pressure pulses measured at various angles around the front face of the model for  $x = 4$  feet and  $w = 0.114$  psf. The pulse shape is about the same at each gage, and peak pressure falls off approximately as  $\cos^2\theta$ . The records from gages near  $\theta = \pm 90^\circ$  have a different appearance, largely because the pressure is much lower and the signal-to-noise ratio is therefore much lower. Pressures on the back side of the model (not shown) do not rise suddenly with the shock, but the pressures are so low that this difference in pulse shape is unimportant.

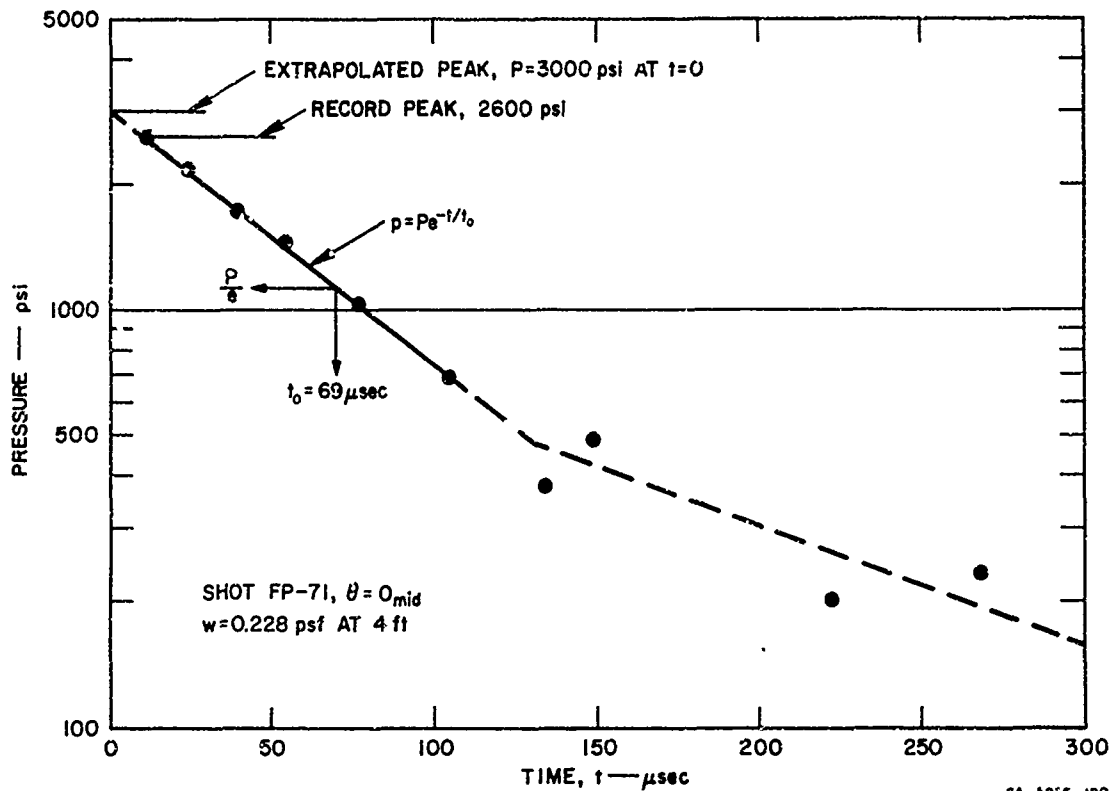


FIG. 18 SEMI-LOG PLOT OF PRESSURE PULSE

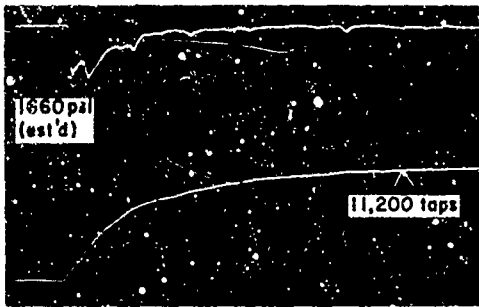
A plot of peak pressure at each gage location versus charge density is given in Fig. 20 for  $x = 4$  feet. Data from the smooth curve fits in Fig. 20 are plotted in Fig. 21 as a function of angle, and the raw data points are repeated. The dashed curve in Fig. 21 is from the formula

$$P = (P_r - P_i) \cos^2 \theta + P_i \quad -90^\circ < \theta < 90^\circ$$

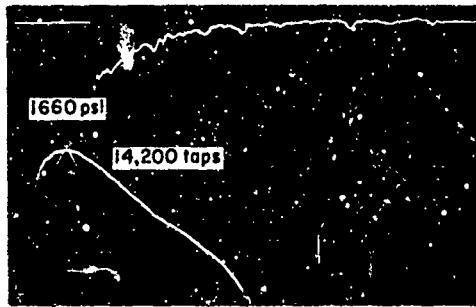
$$P = P_i \quad 90^\circ < \theta < 270^\circ$$

(23)

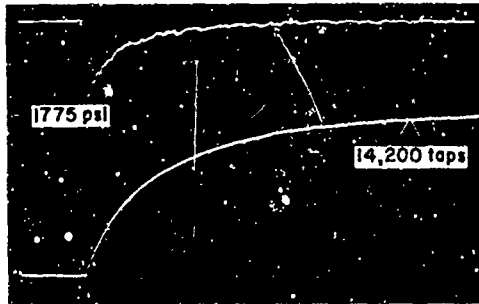
where  $P_r$  is the observed peak overpressure at  $\theta = 0^\circ$  and  $P_i$  is the incident overpressure to give  $P_r$  as a reflected overpressure (using, for example, Fig. 7). As the example curve shows, pressures from this empirical formula coincide with the experimental curves out



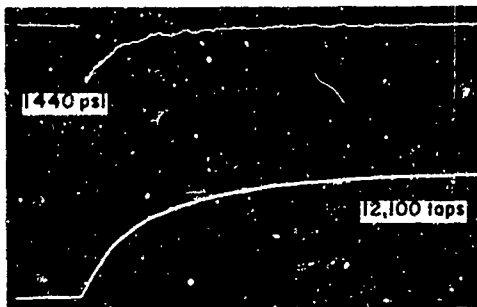
(a)  $\theta = 0_1$



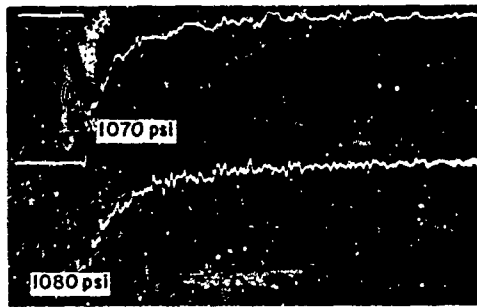
(b)  $\theta = 0_2$  (LOWER TRACE 1 msec/cm BY MISTAKE)



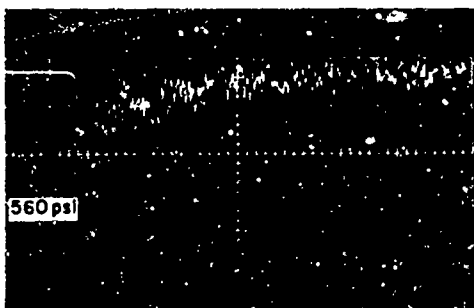
(c)  $\theta = 0_m$



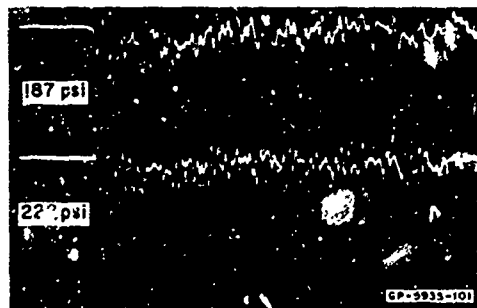
(d)  $\theta = 22.5^\circ$



(e)  $\theta = 45^\circ$  (UPPER) AND  $315^\circ$  (LOWER)



(f)  $\theta = 67.5^\circ$



(g)  $\theta = 90^\circ$  (UPPER) AND  $270^\circ$  (LOWER)

FIG. 19 PRESSURE PULSES ALONG AND AROUND MODEL (Shot FP-70,  $x = 4$  feet,  $w = 0.114$  psf, signals filtered at 120 kc and recorded at  $100 \mu\text{sec/cm}$  except as noted)

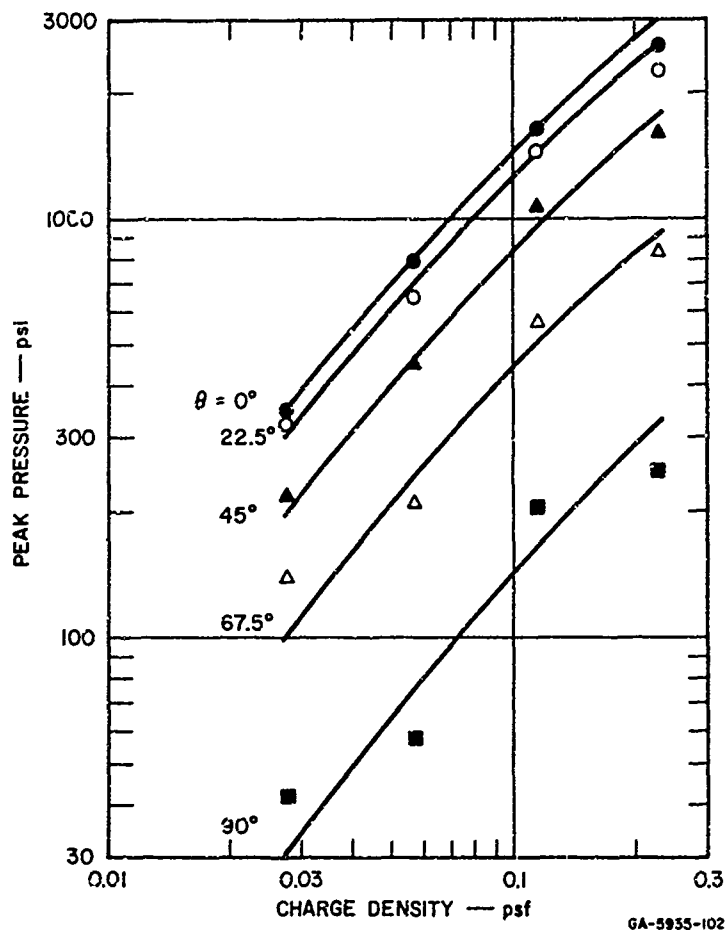


FIG. 20 FRONT FACE PEAK PRESSURES VERSUS CHARGE DENSITY FOR  $x = 4$  FEET

to about  $\theta = 80^\circ$ . Measured pressures further around the model are lower than given by Eq. (23), but in either case are too low to have a significant effect on structural response. Pressure distributions measured for  $x = 1$  foot and  $x = 2$  feet are also represented by Eq. (23) within the experimental error of about  $\pm 10$  percent.

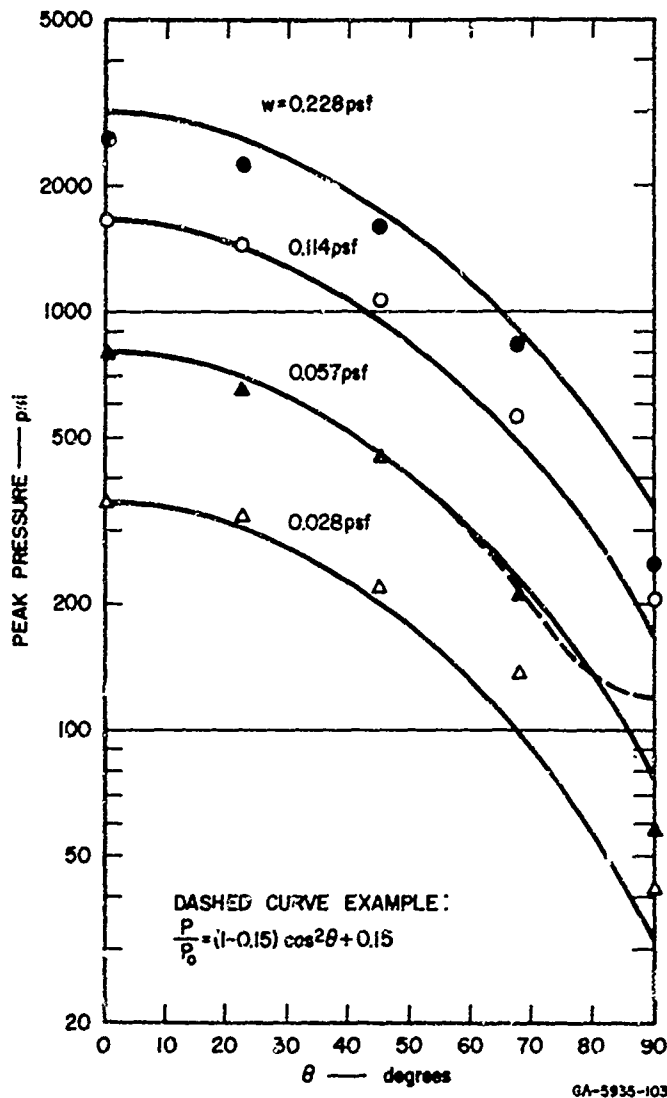


FIG. 21 MEASURED PRESSURE DISTRIBUTIONS OVER FRONT FACE OF MODEL FOR  $x = 4$  FEET

c. Peak Pressure and Impulse

Plots of peak pressures and impulses at  $\theta = 0$  are given in Fig. 22. Although peak pressure depends directly on both charge density and standoff, impulse over this small range of standoffs appears to depend almost entirely on charge density. One would expect the impulse for a fixed charge density to be smaller for a larger standoff, but the measurements show that any difference is hidden in the small scatter in the data of Fig. 22; therefore a single impulse curve is drawn for all three standoffs.

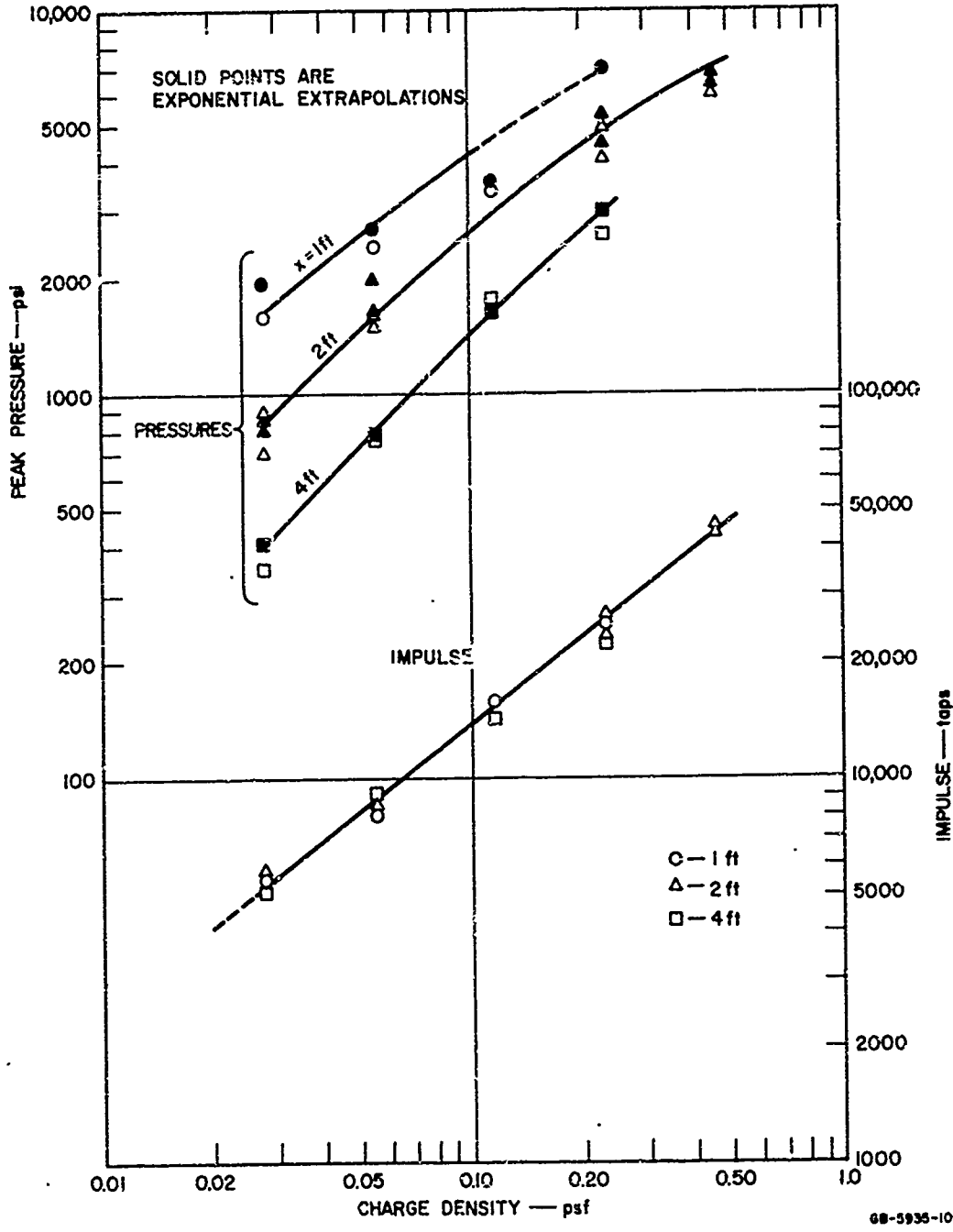


FIG. 22 PEAK PRESSURE AND IMPULSE VERSUS CHARGE DENSITY  
(for running detonation of Primacord charges)

The pressures in Fig. 22 can be compared with the theory of plane expansion from an intense explosion given in Section VI. To make this comparison the explosive yield of Primacord is assumed to be 1570 calories/gm. This is at the lower extreme given for PETN (from 1570 to 2000 cal/gm) by Kinney<sup>7</sup> and is chosen because the PETN here is packed at a relatively low density and, furthermore, the Primacord plastic and braid sheath tend to reduce the effective yield by absorbing more chemical energy than they release. Assuming this yield, the energy release in ergs/cm<sup>2</sup> is\*

$$E_1 = \left[ w_{\text{eff}} \text{ psf} \right] \left[ \frac{454 \text{ gm}}{\text{lb}} \right] \left[ \frac{\text{ft}^2}{(30.5 \text{ cm})^2} \right] \left[ 4.19 \times 10^7 \frac{\text{ergs}}{\text{cal}} \right] \quad (24)$$

$$E_1 \left( \frac{\text{ergs}}{\text{cm}^2} \right) = 3.21 \times 10^{10} w_{\text{eff}} \text{ (psf)}$$

where  $w_{\text{eff}}$  is the effective charge density. For the charges here  $w_{\text{eff}} = 2w$  because they are on the ground and expansion is confined to one direction.† From Eq. (7) the characteristic length is

$$s_1 = \frac{E_1}{P_1} = \frac{3.21 \times 10^{10} w_{\text{eff}} \frac{\text{ergs}}{\text{cm}^2}}{1.013 \times 10^6 \frac{\text{dynes}}{\text{cm}^2}} = 3.16 \times 10^4 w_{\text{eff}} \text{ cm}$$

or, dividing by 30.5 cm/ft

$$s_1 \text{ (ft)} = 1040 w_{\text{eff}} \text{ (psi)} \quad (25)$$

Using  $s_1$  from Eq. (25), the pressures in Fig. 22 are replotted against  $R = x/s_1$  in Fig. 23. Data from all three standoffs fall on a

\* It is unfortunate that cgs units could not be used throughout, but feet, inches, and pounds were firmly entrenched in the shot makeup and hardware.

† Several shots were fired at  $x = 2$  feet from charges freely suspended in air to confirm that the effective charge weight is doubled for confined charges.

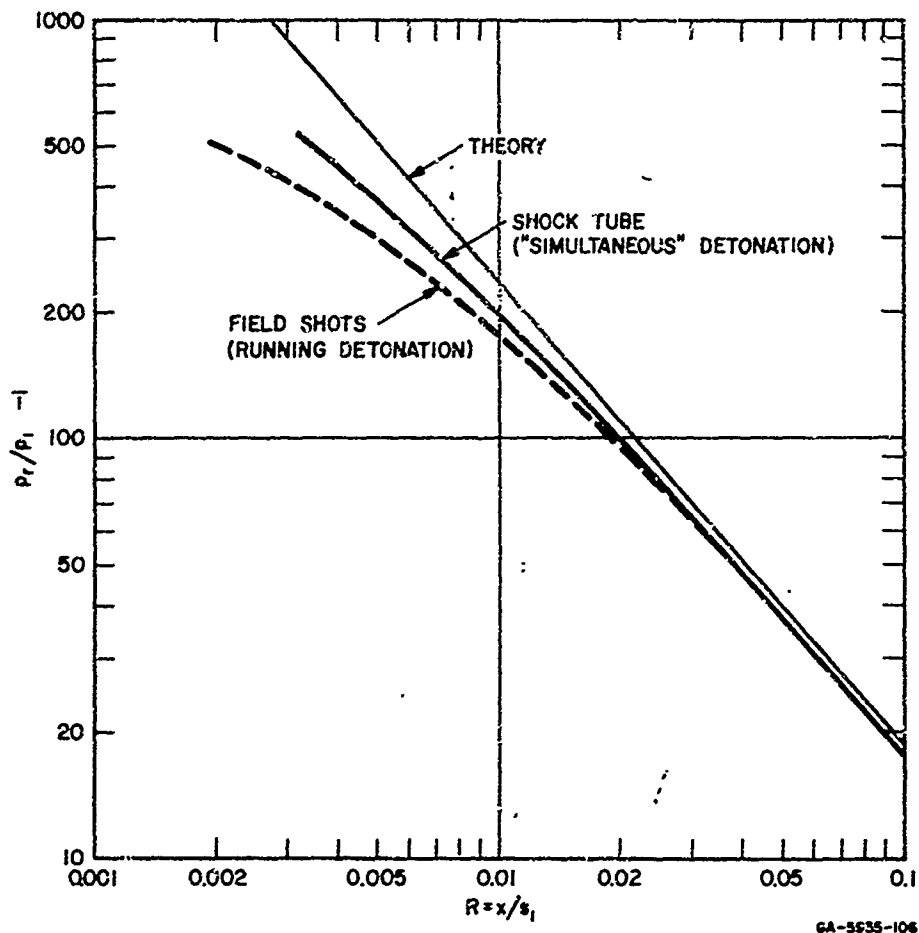


FIG. 23 COMPARISON OF THEORETICAL AND EXPERIMENTAL PEAK PRESSURES

single curve, demonstrating that the normalization to  $s_1$  is appropriate. The curve is therefore simply labeled "running detonation" to emphasize that this is the most significant departure from a truly one-dimensional wave. At the low pressure end of the data (overpressure ratio about 20, or about 300 psi), the measured pressures are only a few percent smaller than the theoretical curve. Furthermore, the theoretical and experimental curves have the same slope. At higher pressures (above about 1500 psi) the measured pressures begin to fall away from the theoretical curve until at  $R = 0.003$  the measured pressure is less than half the theoretical pressure. This difference is caused partly by the neglect of real gas and explosive behavior in the self-

similar theory, and partly because the shock angle caused by the running detonation (see Fig. 13) increases with decreasing R, thereby giving a larger difference from the normally reflected shock assumed in the theory. Pressures from shock tube experiments (to be described later), in which the shock was always normally incident upon the model, are in closer agreement with the theory.

The data from Fig. 22 are replotted in the peak pressure-impulse plane in Fig. 24. The curves for each standoff are roughly parallel to the constant time lines, giving  $t_0 \approx 40 \mu\text{sec}$  at  $x = 1$  foot to  $t_0 \approx 160 \mu\text{sec}$  at  $x = 4$  feet. These curves are discussed more fully at the end of Section III.5.

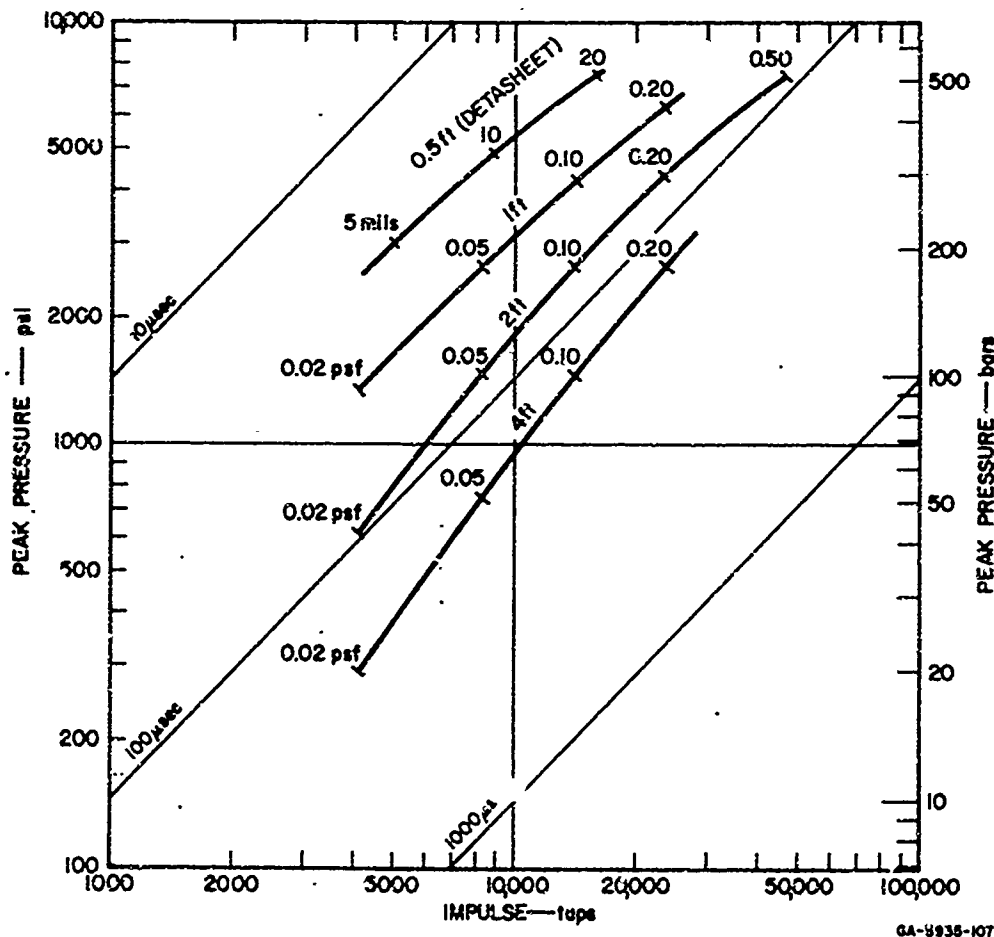
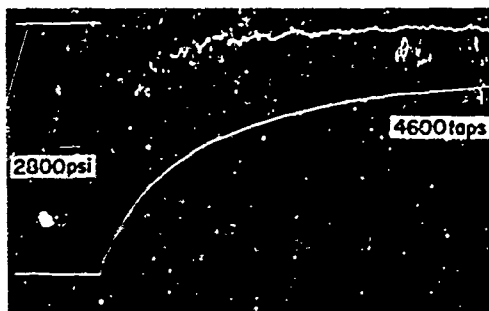


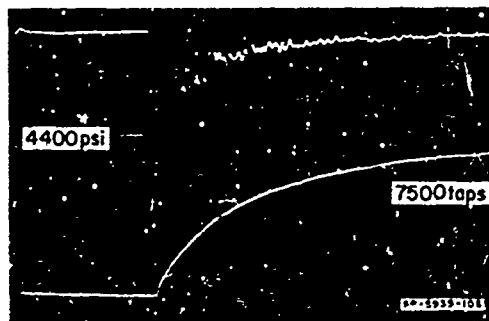
FIG. 24 PRESSURE-IMPULSE CURVES FOR RUNNING DETONATION OF FLAT CHARGES

#### 4. Surface Loads from Flat Detasheet Charges

Pressure pulses were measured for sheet explosive charges at  $x = 0.5$  and  $1.0$  feet. Typical records are shown in Fig. 25 for  $x = 0.5$  foot. As at the larger standoffs using Primacord, these pulses are exponential in shape. Pressure distributions differ from those given by Eq. (23) because the standoff is now so small that it is comparable to the model diameter. However, the significant decrease in pressure caused by the increase in shock travel distance with increasing  $\theta$  can be taken into account by adjusting at each  $\theta$  the reflected pressure  $p_r$  in Eq. (24), using the curves established for  $p_r$  versus  $x$ . Pressures calculated by this procedure agree with measured pressures within the precision of measurement.



(a)  $h=4.4$ mils



(b)  $h=8.8$ mils

FIG. 25 PRESSURE PULSES AT  $\theta = 0$  FOR SHEET EXPLOSIVE CHARGES AT  $x = 0.5$  FEET (sweep rate  $20 \mu\text{sec/cm}$ )

Peak pressures and impulses are plotted against average explosive thickness in Fig. 26. Again, to the accuracy of the data, impulse depends only on explosive thickness. To compare the peak pressures with theory,  $s_1$  is calculated using 1570 cal/gm of PETN content (about 80 percent by weight) in the Detasheet. This is the same yield used for Primacord and should give comparable results, because the 20-percent nonexplosive binder ingredients in Detasheet reduce the yield in the same way as the sheath in the Primacord. The release energy per

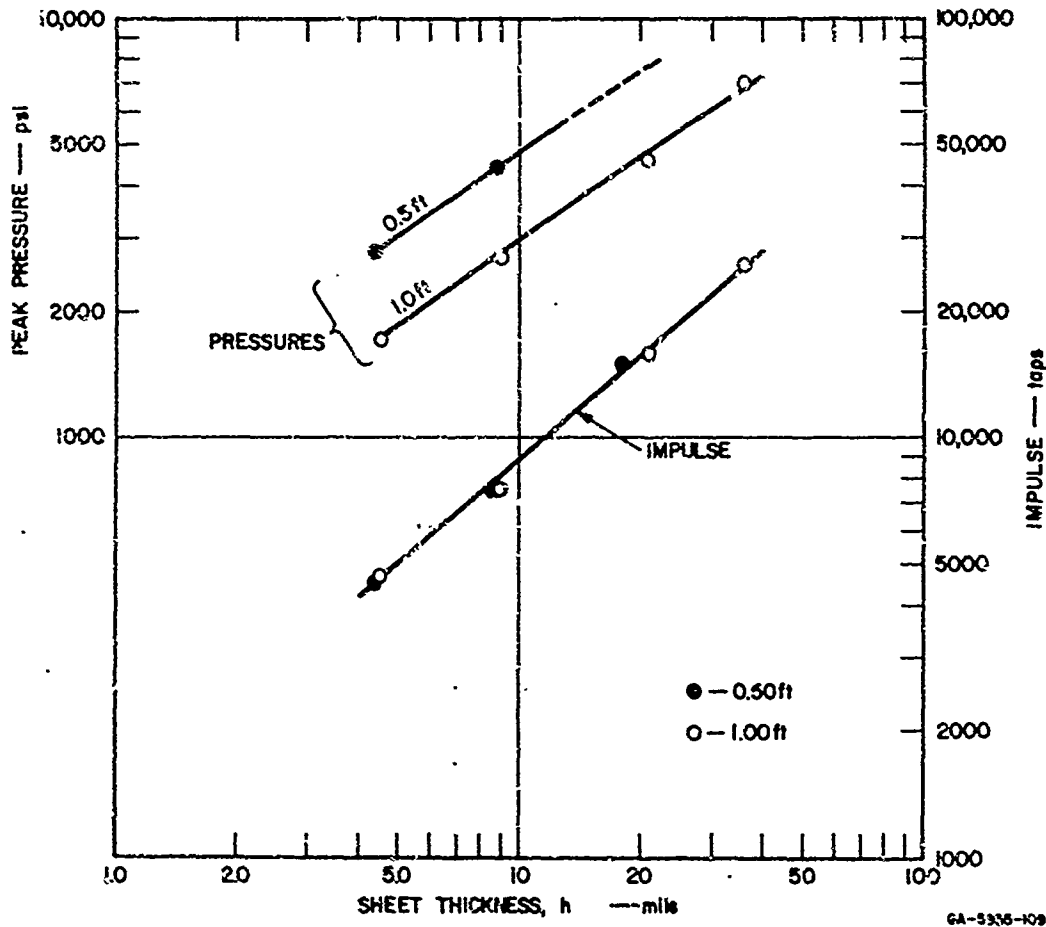


FIG. 26 PEAK PRESSURE AND IMPULSE VERSUS AVERAGE THICKNESS OF SHEET EXPLOSIVE CHARGES

unit area for an effective thickness  $h_{\text{eff}}$  is then

$$E_1 \left( \frac{\text{ergs}}{\text{cm}^2} \right) = \left[ h_{\text{eff}} \text{ cm} \right] \left[ 0.8 \rho \frac{\text{gm}}{\text{cm}^3} \right] \left[ 1570 \frac{\text{cal}}{\text{gm}} \right] \left[ 4.19 \times 10^7 \frac{\text{ergs}}{\text{cal}} \right]$$

$$= 7.37 \times 10^{10} h_{\text{eff}} \text{ (cm)}$$

where  $\rho = 1.4 \text{ gm/cm}^3$  is the overall density of the explosive and  $0.8 \rho$  is the PETN content. The characteristic length is

$$s_1 \text{ (cm)} = \frac{E_1}{P_1} = \frac{7.37 \times 10^{10} h_{\text{eff}} \frac{\text{ergs}}{\text{cm}^2}}{1.013 \times 10^6 \frac{\text{dynes}}{\text{cm}^2}} = 7.26 \times 10^4 h_{\text{eff}} \text{ (cm)}$$

For  $s_1$  in inches and  $h_{\text{eff}}$  in mils

$$s_1 \text{ (in.)} = 72.6 h_{\text{eff}} \text{ (mils)} \quad (26)$$

Using  $h_{\text{eff}} = 2h$ , the pressure curves in Fig. 26 give a normalized curve very nearly coinciding with the normalized curve in Fig. 23 for running detonation of Primacord. Thus in Fig. 23 no distinction is made between Primacord and Detasheet. Similarly, the pressure-impulse curves for Detasheet are merely an extension of the curves in Fig. 24 for Primacord, extending pulse times down to  $t_0 \approx 25 \mu\text{sec}$ .

##### 5. Surface Loads from Flat Charges Confined in a Shock Tube

At standoffs greater than a few feet, it is impractical to maintain one-dimensional flow by keeping the charge dimensions large compared to the standoff. A better arrangement is to place the charge in a shock tube as in Fig. 27 so that the walls of the tube maintain one-dimensional flow. Some loss occurs because of friction along the sides of the tube, but the comparison to theory given later suggests that this effect is not serious for  $X/D \gtrsim 5$  and causes a decrease in pressure of at most 40 percent at  $x/D = 10$  ( $D$  is tube diameter). It becomes impractical to use

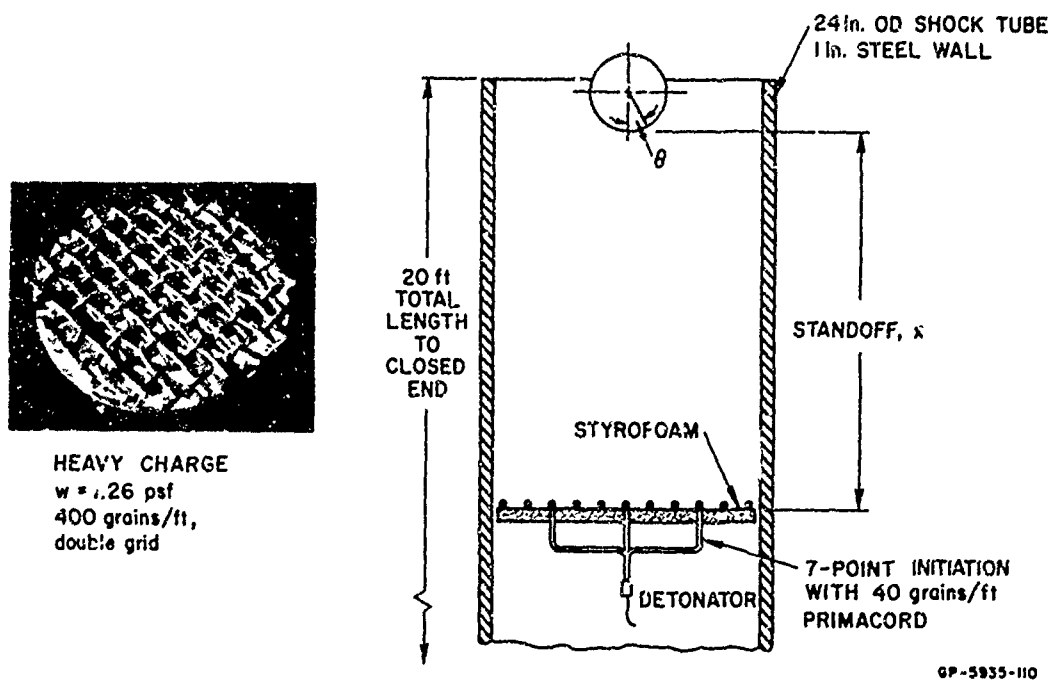


FIG. 27 ARRANGEMENT OF FLAT CHARGES IN SHOCK TUBE

the shock tube at standoffs less than a few feet because detonation of the charge must be nearly simultaneous to initiate one-dimensional flow. At large standoffs, multipoint symmetric initiation is satisfactory, but at small standoffs it is more convenient to use single point initiation of a running detonation, which is the scheme already described in the preceding sections. Running detonation cannot be used in a shock tube because it results in an oblique shock (Fig. 13) which would reverberate against the tube walls.

Charge arrangement and method of detonation in the shock tube are shown in Fig. 27. The charges were made of Primacord grids and were simultaneously initiated at 7 points by a lead-in spider of 40 grain/ft Primacord. The model was placed at the open end of the shock tube and the charges were placed at standoffs of 1, 2.5, 5, 10, and the total 20-foot length to the closed end of the shock tube. At the 20-foot standoff, expansion from the charge was confined by the bottom of the tube to one direction, as in the field charges on the ground. At smaller standoffs, however, the charges were suspended on low density

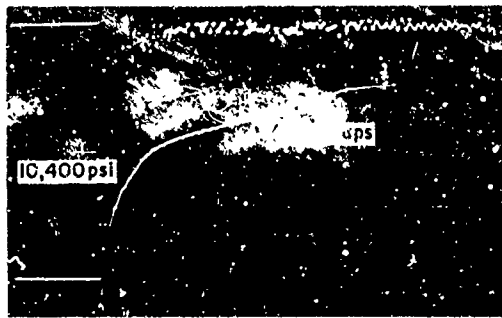
(about 2 lb/ft<sup>3</sup>) styrofoam pads so the blast was free to expand in both directions from the charge. At these intermediate standoffs the reflected shock from the bottom of the tube arrived at the model much later than the direct shock and was always at a much smaller pressure. In the worst case, at the 10-foot standoff, the model pressure from the reflected shock was less than 15 percent of the direct shock model pressure (see Fig. 28d), which can safely be neglected in structural testing.

a. Pulse Shape and Pressure Distribution

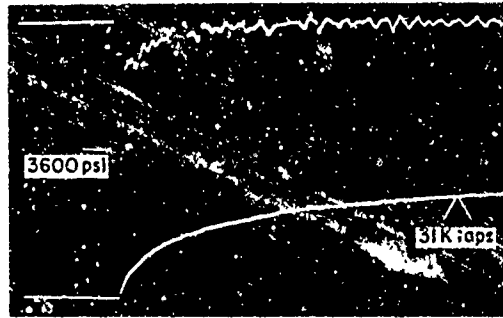
Typical pressure pulses at each standoff are given in Fig. 28. Pulses at various charge densities for a 10-foot standoff are given in Fig. 29. The main body in all the pulses is exponential in shape, followed by a low pressure tail which decays at a lower rate. In some cases the exponential is preceded by an initially more rapid decay. In all cases, except at the 1-foot standoff, the entire decay in pressure is quite smooth as seen by the integrated pressures (the lower traces). At the 1-foot standoff the method of charge initiation does not give a sufficiently plane shock wave and shocks reflect from the tube walls. Also, at one foot the pressure measured at the center of the model was as much as twice the pressure measured at either end gage. However, at  $x > 2.5$  feet, pressures from all three gages along the model length were generally within a few percent of each other and showed no tendency for the pressure at the center of the model to be larger. Variation in pressure around the model was again reasonably well approximated by Eq. (23).

b. Peak Pressures and Impulses

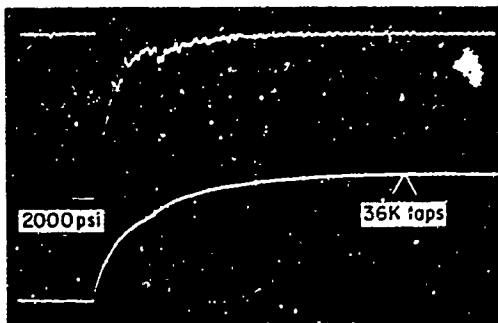
Figure 30 gives peak pressures and impulses plotted against charge density. Each data point is an average from the three  $\theta = 0$  gages along the shell. Data for  $x = 1$  foot are omitted for the reasons just discussed. The pressures at  $x = 2.5, 5,$  and  $10$  feet scale very closely to the one-dimensional blast theory in Fig. 23, i.e., the curves are merely shifted along the  $w$ -axis by factors of 2. The dotted curve for  $x = 10$  feet is the curve for  $x = 5$  feet shifted by 2 and falls very close to the solid curve, drawn through the 10-foot data. One would



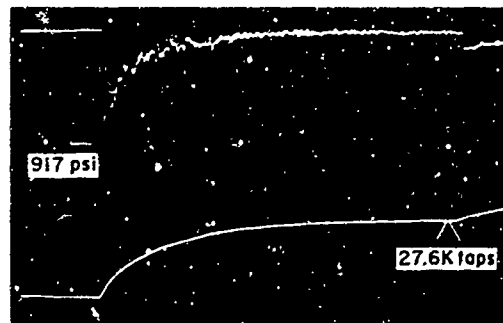
(a)  $x = 1$  ft, SWEEP RATE =  $50 \mu\text{sec/cm}$



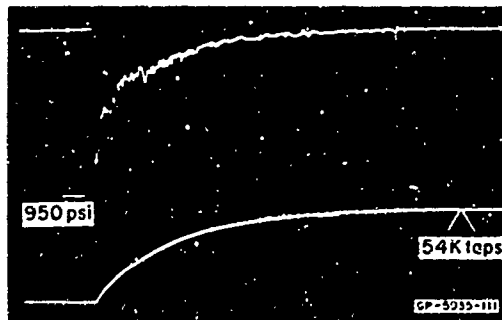
(b)  $x = 2.5$  ft, SWEEP RATE =  $200 \mu\text{sec/cm}$



(c)  $x = 5$  ft, SWEEP RATE =  $500 \mu\text{sec/cm}$



(d)  $x = 10$  ft, SWEEP RATE =  $500 \mu\text{sec/cm}$



(e)  $x = 20$  ft,  $w_{\text{eff}} = 0.52 \text{ psf} \times 2$ ,  
SWEEP RATE =  $1 \text{ msec/cm}$

FIG. 28 SHOCK TUBE PRESSURE PULSES AT STANDOFFS FROM 1 FOOT TO 20 FEET [all at  $w = 0.316 \text{ psf}$  except  $w = 0.52 \text{ psf} \times 2$  in (e)]

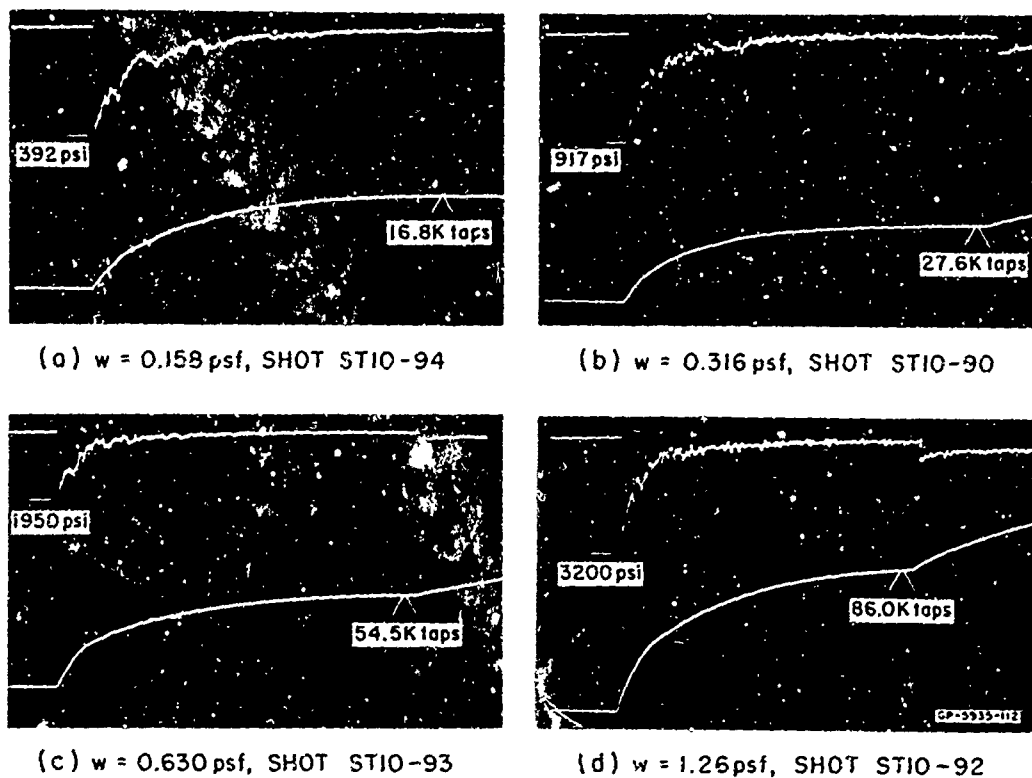


FIG. 29 SHOCK TUBE PRESSURE PULSES AT 10-FOOT STANDOFF

expect the 10-foot curve to fall below the theory because of friction losses along the tube wall. The upper dat. point for  $x = 2.5$  feet is slightly below its curve, but this is attributed to poor records on this shot. The pressure curve for  $x = 20$  feet should fall on the  $x = 10$ -foot curve if the one-dimensional theory were still applicable, because the charge is at the bottom of the tube and the effective charge weight is doubled. Instead, the curve lies a factor of about 1.6 to the right of the solid 10-foot curve and 1.7 to the right of the dotted curve. This wide divergence from theory is probably caused partly by still further wall friction losses at this large standoff and, perhaps more important, because the charge was actually a few inches above the bottom of the tube, thereby spreading out the initial front of the shock.

The magnitudes of the pressures in Fig. 30 were compared with the intense explosion theory using Eq. (25) and Fig. 23 as for the field shots.

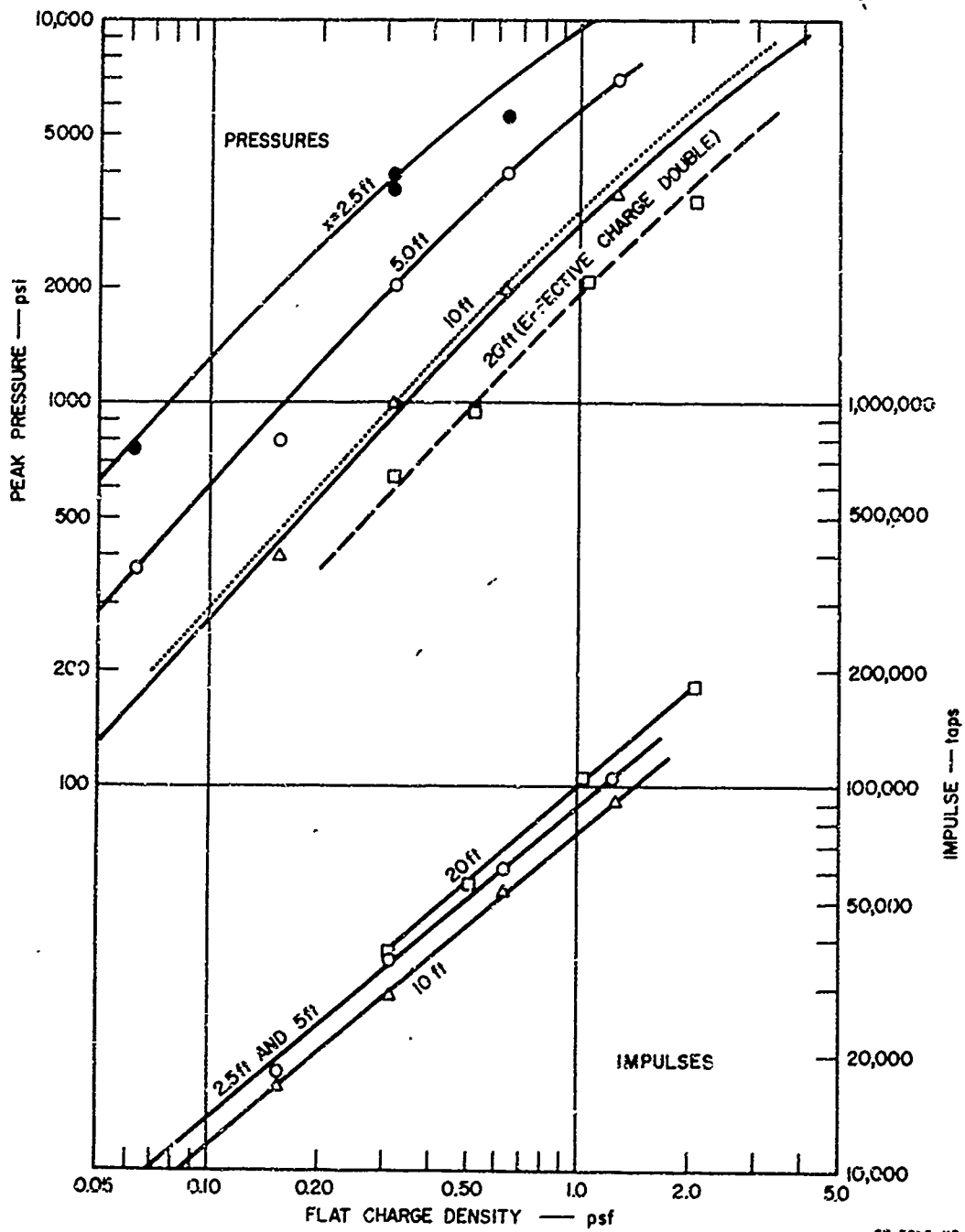


FIG. 30 PEAK SHOCK TUBE PRESSURES AND IMPULSES VERSUS CHARGE DENSITY (charges freely suspended except at  $x = 20$  feet, charge against bottom of tube)

Data for  $x = 2.5$  feet, 5 feet, and the dotted curve in Fig. 30 for  $x = 10$  feet all fall on a single curve in Fig. 23. This curve coincides with the running detonation curve at the low pressure end, and at higher pressures lies closer to the theoretical curve than the running detonation curve, as one would expect, because here we have normal shock incidence.

Impulses for  $x = 2.5$  feet and  $x = 5.0$  feet are given by a single curve in Fig. 30 to the accuracy of measurement. The impulse curve for  $x = 10$  feet lies about 15 percent below the 5-foot curve, and the 20-foot curve (after it is shifted to the right by a factor of 2 to account for effective charge doubling) lies about 25 percent below the 10-foot curve. Thus, as in the field shots, impulse depends mainly on charge density, but here the standoff is becoming large enough that impulse per unit charge density is decreasing measurably with standoff.

A pressure-impulse plot of the data in Fig. 30 appears in Fig. 31 along with data from the running detonation field shots. The  $x = 4$ -foot curve for the field shots is omitted for clarity and because in practice it is more convenient to prepare shock tube charges than the large 8 x 8-foot charges required in the field at  $x = 4$  feet. The P,I curves for the field and shock tube data fall nicely together into a set of nearly parallel curves, but it is apparent that at a given standoff, impulse is higher in the shock tube. Imagining an interpolated curve drawn for  $x = 2.5$  feet for the field shots, the corresponding  $x = 2.5$ -foot shock tube curve gives pressures from 30 to 50 percent larger. This difference is attributed to pressure decay in the field shots caused by the finite size of the charges (see Fig. 11).

Also drawn in Fig. 31 are critical curves for damage of a weak shell and a strong shell, both taken from Reference 1. The weak shell is a simple unsupported 6061-T6 aluminum shell with radius-to-thickness ratio  $a/h = 100$  and length-to-diameter ratio  $L/D = 1$ . The strong shell has  $a/h = 24$  and is covered by a Micarta\* shell with  $a/h = 12$ . The sheet charge pressure-impulse curves span the region between these two shells and between the  $t_0 = 10 \mu\text{sec}$  and  $t_0 = 1000 \mu\text{sec}$  lines, as desired.

\*Micarta is a registered tradename of Westinghouse Electric Corporation.

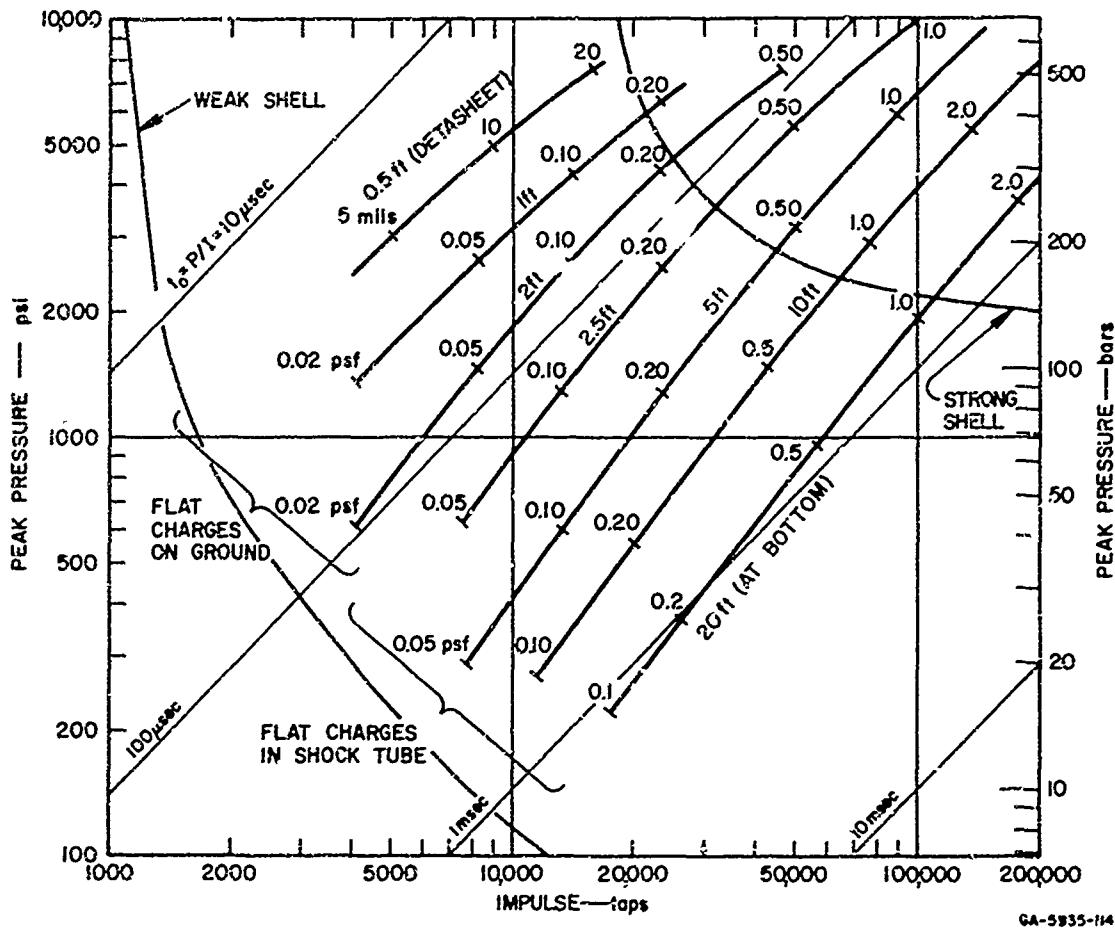


FIG. 31 PRESSURE-IMPULSE CURVES FOR ASYMMETRIC LOADING TECHNIQUES (6-inch-diameter model)

The characteristic times  $t_o = I/P$  in Fig. 31 can be compared to the incident pulse time scales  $t_{fl}$  calculated using Eq. (6) from the strong shock theory. For  $w = 1$  psf in the shock tube at  $x = 5$  feet, this equation, with  $s_1$  from Eq. (25), gives  $t_{fl} = 458 \mu\text{sec}$ . From Fig. 31,  $t_o$  for the point  $x = 5$  feet,  $w = 1$  psf, is  $200 \mu\text{sec}$ . As expected, this time is smaller than  $t_{fl}$ , the ratio being  $t_o/t_{fl} = 0.44$ . Further down the curve, at  $x = 5$  feet and  $w = 0.05$  psf,  $t_{fl} = 1750 \mu\text{sec}$  and  $t_o = 400 \mu\text{sec}$ , giving a ratio  $t_o/t_{fl} = 0.23$ . On the Detasheet curve at  $x = 0.5$  foot and  $h = 10$  mils ( $h_{eff} = 20$  mils), Eqs. (6) and (26) give  $t_{fl} = 36.3 \mu\text{sec}$  and Fig. 31 gives  $t_o = 26 \mu\text{sec}$ ;

the ratio is  $t_o/t_{fl} = 0.71$ . These comparisons show that  $t_{fl}$  is a crude but useful estimate for  $t_o$ , with  $t_o$  being about half of  $t_{fl}$  for high pressures and decreasing to about one-fourth of  $t_{fl}$  for the lower pressures and larger standoffs here. A better estimate for model impulse  $I$  and time  $t_o$  could be obtained by calculating the reflected impulse  $I_r$  from a flat, rigid wall and taking  $t_r = I_r/P_r$ . This would require extensive computer calculations of the type in References 8 and 9, but the usefulness of the results would certainly justify the effort.

All of the curves in Fig. 31 extend easily to loads greater than the strong shell damage curve, and all but the  $x = 0.5$ -foot curve can be extended below the weak shell curve. At small standoffs the explosive spacing rule  $S/x \gtrsim 6$  and minimum explosive rod size discussed in Section III.2 allows impulses only as small as about 1000 taps at  $x = 0.5$  foot. However, impulses as low as 100 taps can be obtained with gaseous explosives.<sup>2,5</sup>

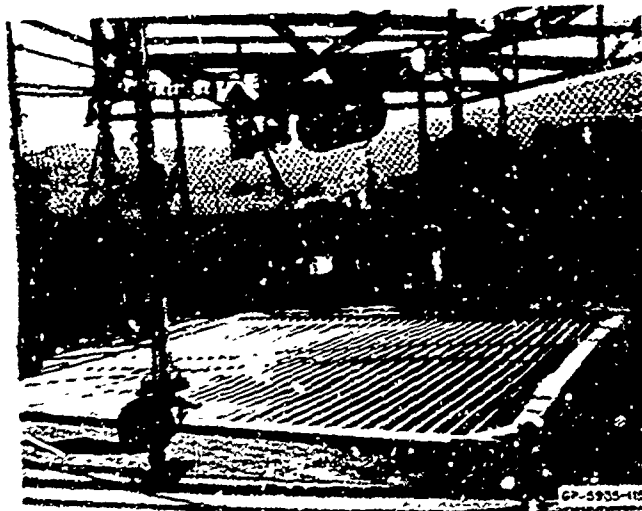
#### 6. Effects of Model Size

The pressure-impulse curves in Fig. 31 are applicable only to 6-inch-diameter models because pressure decay, and therefore impulse, depends upon model size. In the limit of an extremely large model (or small standoff) the impulse is maximum, equal to the reflected impulse from a flat, rigid wall. As the model becomes smaller and smaller (or the standoff becomes larger and larger) quasi-steady flow is established around the model in a time short compared to the total blast duration. The pressure quickly drops from the reflected pressure to a decaying drag pressure and the impulse is determined by drag flow rather than by diffraction flow. For very long pulses the diffraction flow is so short compared to the drag flow that the peak pressure is more appropriately associated with the stagnation pressure. Then pressure and impulse intensity no longer depend on model size.

The 6-inch-model size was selected for most of the experiments described in this report, because it is a convenient size for structural models. However, smaller and larger structural models are often used and, to give some indication of the change in impulse with diameter, a



(a) 2-FOOT STANDOFF  
 $w=0.057$  psf



(b) 4-FOOT STANDOFF  
 $w=0.114$  psf

FIG. 32 ARRANGEMENT FOR DETERMINING EFFECT OF MODEL SIZE (3.5-inch and 12-inch-diameter cylinders)

of shots at  $x = 2$  feet are given in Fig. 33 along with impulse data from the previous shots on the 6-inch model. The difference in impulse on the models is largest at the smallest charge density, with impulse on the 12-inch-diameter model being about 1.4 times that on the 3.5-inch-diameter model at  $w = 0.03$  psf. At the other extreme,  $w = 0.45$  psf, the impulse ratio is only about 1.1. In a shot at  $w = 0.114$  psf and  $x = 4$  feet, the impulse ratio was 1.3. These differences in impulse are not much larger than possible errors of 10 to 20 percent in reading the impulse, caused by inaccuracies in gage sensitivity and, more important, in low pressure drift due to gage heating and other effects. Nevertheless, the smallness of the change in impulse with model size observed here shows that the pressure-impulse curves in Fig. 31 can be used as estimates for larger and smaller models; more accurate estimates can be made over a limited range by correcting with the aid of the ratios above.

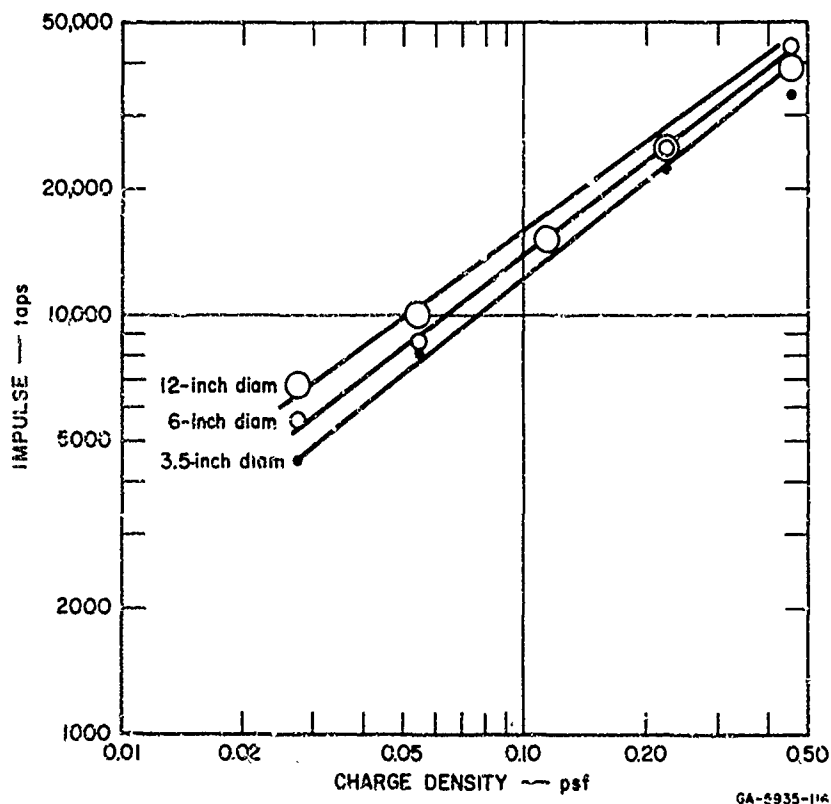


FIG. 33 IMPULSES ON 3.5-, 6-, AND 12-INCH-DIAMETER MODELS

## SECTION IV

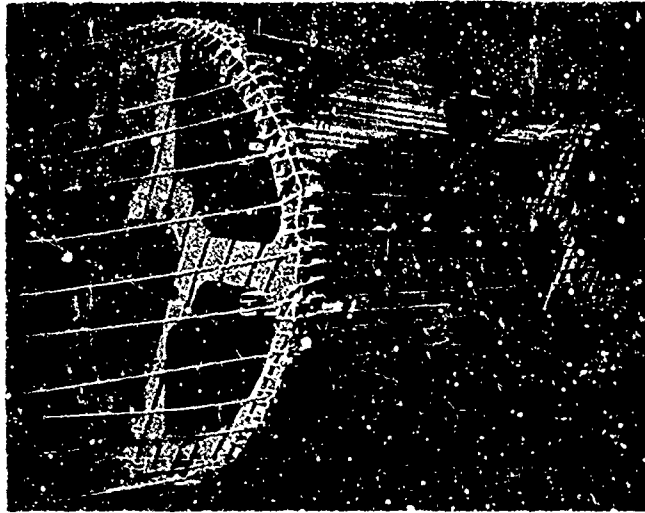
### SIMULATION OF SYMMETRIC LOADS

The methods described here for simulating symmetric loads are logical extensions of the methods just described for asymmetric loads. To obtain quasi-impulsive loads, the flat charges on the ground were replaced by cylindrical charges completely surrounding the model, again at standoffs of a few feet. To obtain longer duration loads, the shock tube was used as it was for asymmetric loads, but the model was pointed down the tube with its axis in line with the axis of the shock tube. The experiments reported here are not as extensive as those described for asymmetric loads because emphasis was on feasibility of the techniques rather than extensive calibration. Considerable further work, both theoretical and experimental, is necessary to exploit the techniques described here.

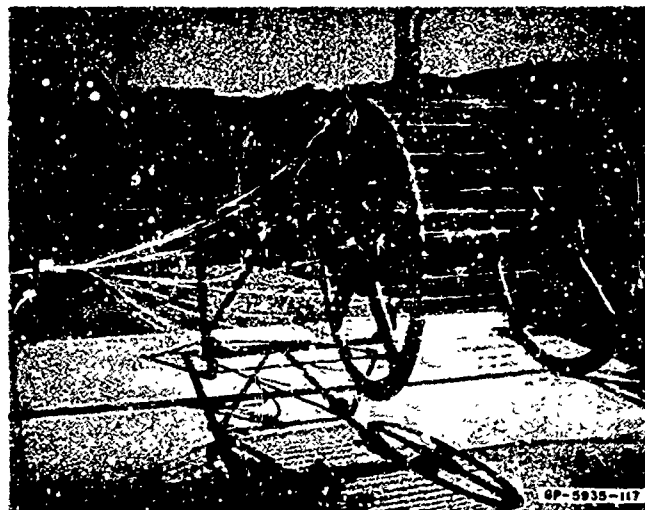
#### 1. Surface Loads from Cylindrical Charges

Cylindrical charges 2 feet and 4 feet in diameter were made by stringing Primacord strands between cartwheel end frames as shown in Fig. 34. The rigid model was 6 inches in diameter, giving corresponding standoff distances of 0.75 and 1.75 feet. For both diameters the distance between end frames was 3 feet and the charges were initiated by a cone of Primacord strands at one end, resulting in a nearly circular detonation front sweeping axially along the model.

Pulse shape was generally exponential, as it was for asymmetric loads. Pressure pulses at the lightest and heaviest charge densities used at each diameter are given in Fig. 35. As Fig. 36 shows, the distribution of peak pressure around the model was satisfactorily uniform in all but one shot. In all of the 2-foot-diameter shots peak pressure was uniform within  $\pm 10$  percent. At 4 feet the spread was slightly larger, but still acceptable, except at the heaviest charge density, for which peak pressure varied from 4500 to 9000 psi. Impulse was always very nearly uniform around the model, even in this shot.

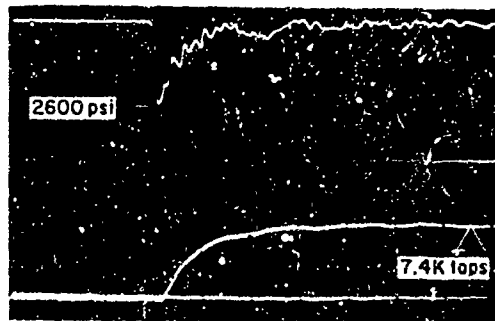


(a) 2-FOOT DIAMETER CHARGE,  $w = 0.0915$  psf  
40-grain PRIMACORD ON 0.75-inch CENTERS,  
SHOT C-88

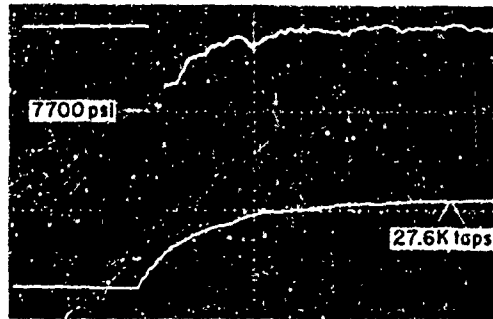


(b) 4-FOOT DIAMETER CHARGE,  $w = 0.023$  psf  
40-grain PRIMACORD ON 3-inch CENTERS,  
SHOT C-120

FIG. 34 CYLINDRICAL CHARGES FOR SYMMETRIC  
QUASI-IMPULSIVE LOADS

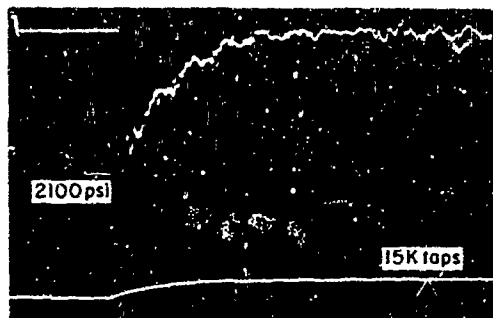


(a)  $w = 0.023$  psf (SHOT C-42)

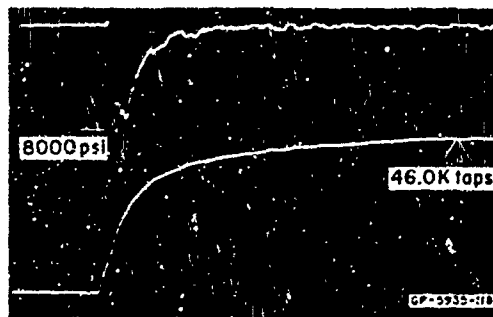


(b)  $w = 0.092$  psf (SHOT C-88)

2-FOOT DIAMETER CHARGES ( $x = 0.75$  ft)



(c)  $w = 0.029$  psf (SHOT C-86)



(d)  $w = 0.115$  psf (SHOT C-87)

4-FOOT DIAMETER CHARGES ( $x = 1.75$  ft)

FIG. 35 PRESSURE PULSES FROM CYLINDRICAL CHARGES [filtered at  $120 \mu c$ ,  $50 \mu \text{sec}/\text{cm}$  sweep in (a) and (b),  $100 \mu \text{sec}/\text{cm}$  in (c) and (d)]

Thus the pressure pulse at 9000 psi decayed more rapidly than the pulses at 4500 psi. One would expect the pressure to fluctuate more for the larger diameter charge cause of imperfect convergence and instability of the imploding shock, but it is not evident whether the largest pressure fluctuations occurred at the highest charge density by chance, or because of inherently poorer convergence as charge density increases. Unsymmetric convergence also caused some changes in the initial shape of the pressure pulse, reducing the peak pressure and giving it a flat or rounded top. These changes were not serious and were observed in only a few of the more than 50 pressure records.

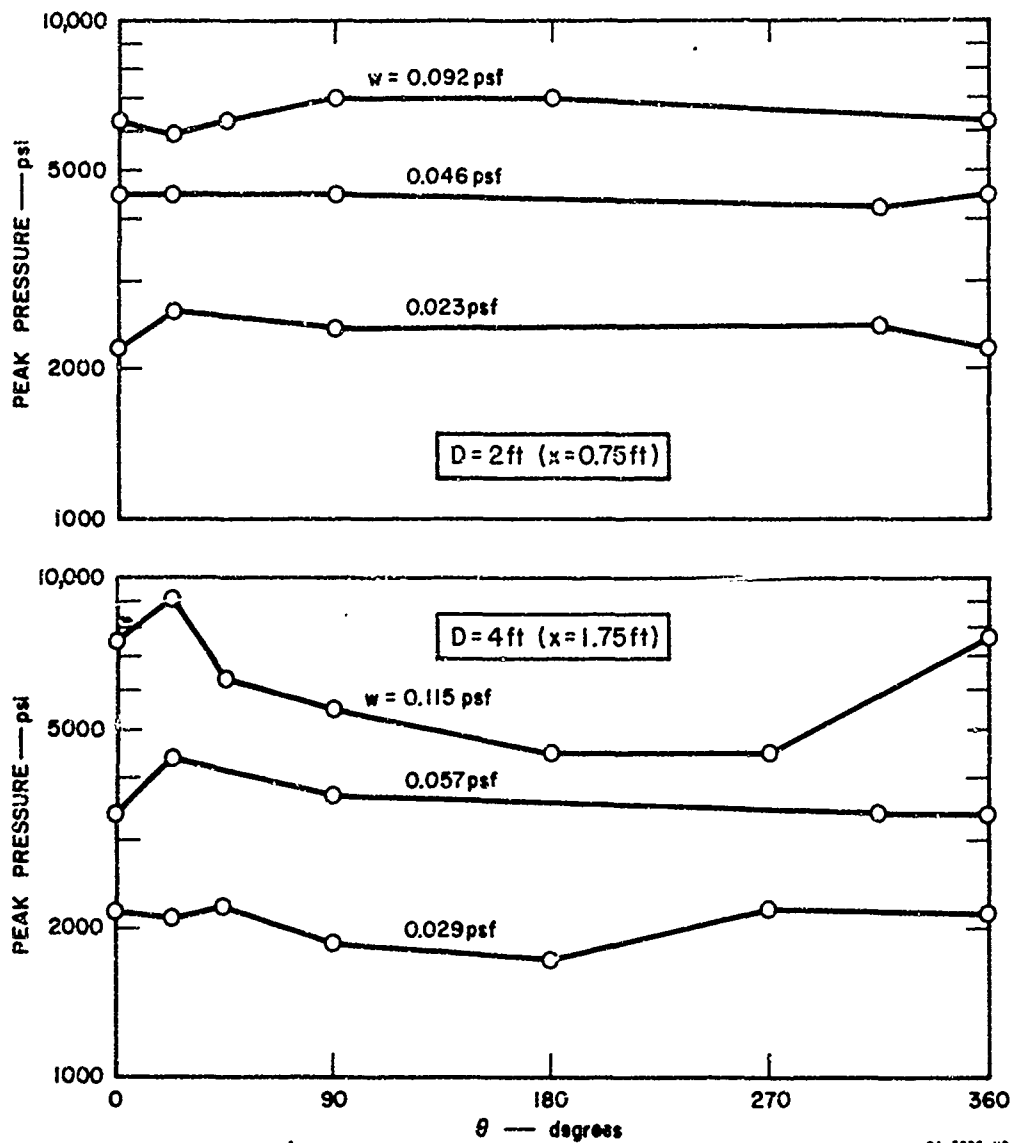


FIG. 36 VARIATION IN MEASURED PRESSURES AROUND THE CIRCUMFERENCE

Peak pressure and impulse versus charge density at each radius are given in Fig. 37. As expected, pressures are lower and impulses higher at the larger radius, so that in the pressure-impulse plane (Fig. 38) the characteristic time  $t_0$  is larger for the larger charge radius, about 90  $\mu$ sec at 4 feet compared to about 40  $\mu$ sec at 2 feet. The curves in Fig. 38 converge toward each other at larger pressures, giving a smaller difference in  $t_0$ .

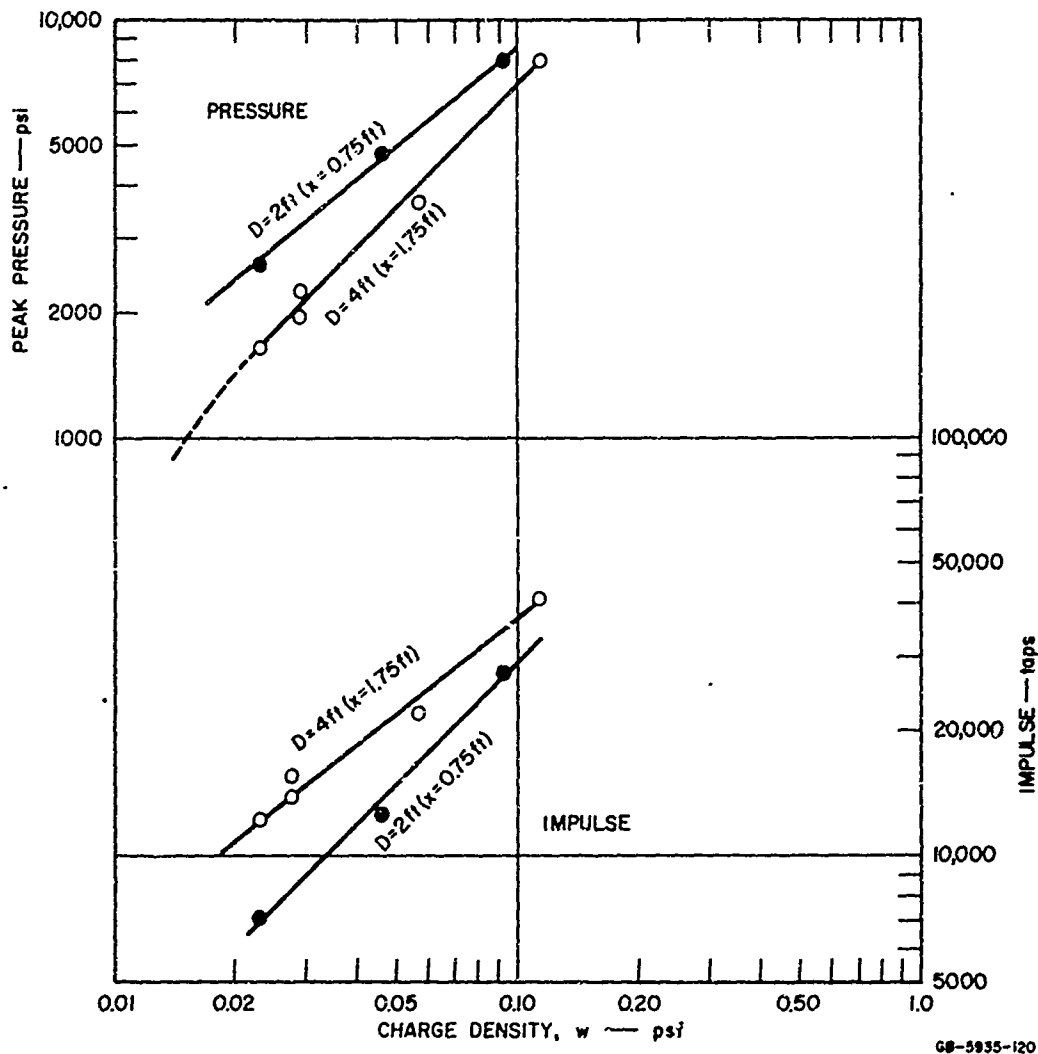


FIG. 37 PEAK PRESSURE AND IMPULSE VERSUS CYLINDRICAL CHARGE DENSITY

No theoretical calculations have been carried out to compare with these measured pressures, but it is apparent that such calculations are even more necessary here than for the plane shocks in the preceding section because model size has a strong effect on both pressure and impulse. For example, the asymmetric pressure-impulse curves in Fig. 31 can be used to estimate loads for model sizes from, say, about 3 inches to 12 inches in diameter with only a small error in impulse (see Section III.6) and no error in peak pressure. By contrast, the data in Fig. 38 apply only to a 6-inch-diameter model. Without a theory, loads

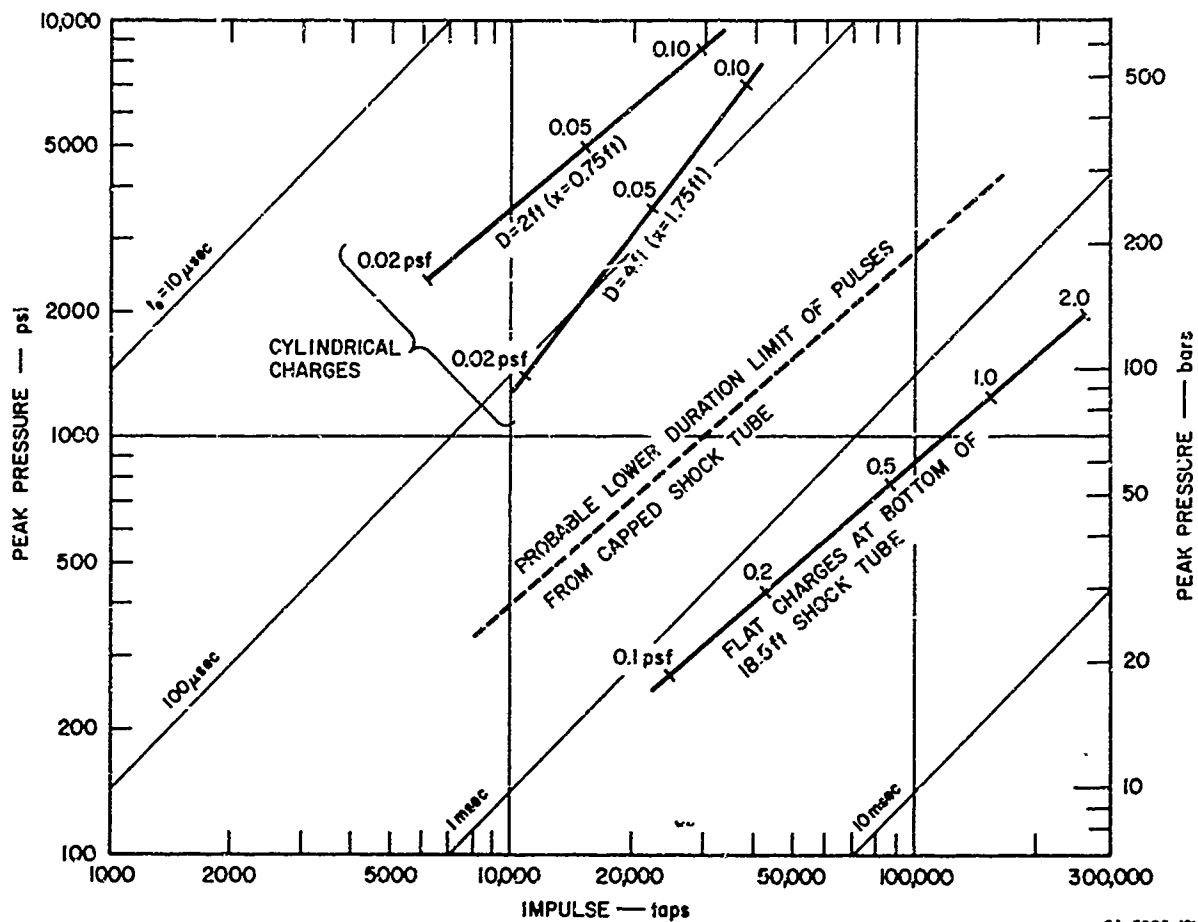
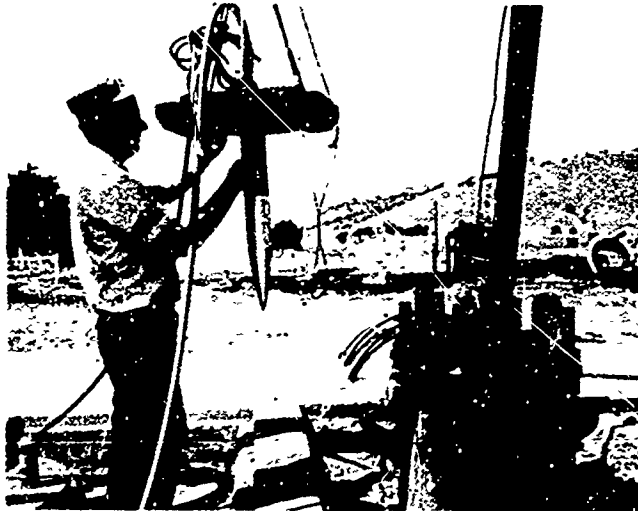


FIG. 38 PRESSURE-IMPULSE CURVES FOR SYMMETRIC LOADING TECHNIQUES (6-inch-diameter models)

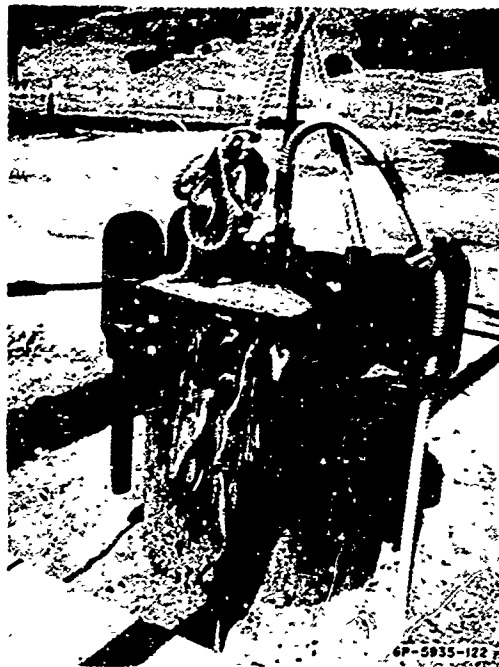
on other model sizes cannot be estimated; it would be difficult to calibrate the cylindrical charge technique for a range of model sizes without a theory as a guide. Since the present experiments demonstrate that useful quasi-impulsive loads can be obtained using cylindrical charges, a theoretical program should also be pursued.

## 2. Symmetric Loads in a Capped Shock Tube

Longer duration loads were obtained using flat charges in the 2-foot-diameter shock tube with the model pointing down the tube as shown in Fig. 39. For moderately low pressures the model can be placed on a sting with a minimum of cross bracing so that the incident blast wave can flow



(a) 3.5-inch DIAMETER MODEL



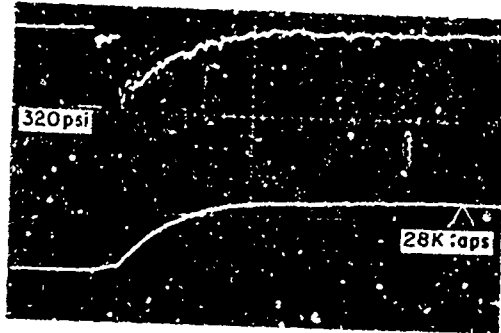
(b) TUBE CAPPED, 3/8-inch ABOVE  
TUBE FOR VENTING

FIG. 39 EXPERIMENTAL ARRANGEMENT FOR SYMMETRIC  
LOADS IN CAPPED SHOCK TUBE

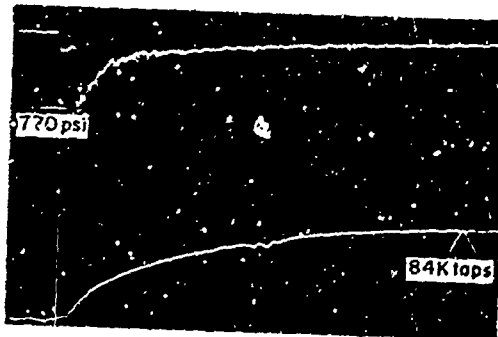
past the model. Peak pressure is then near the incident pressure. At high pressures, however, the necessary charge weights using the incident pressure become objectionably large. For example, to obtain an incident overpressure ratio of 200 ( $\approx 3000$  psi), Fig. 53 shows that the normalized standoff must be less than  $R = x/s_1 = 0.001$ . At a standoff  $x = 10$  feet, Eq. (25) gives a corresponding charge density of  $w = x/1040 R \approx 10$  psf. For the 2-foot-diameter shock tube this gives a total charge weight of 30 pounds. The actual charge weight needed is probably about twice this because at these high pressures the self-similar theory overestimates the pressure. It is very likely that a 60-pound disk of explosive would rupture the 1-inch-thick steel wall of the shock tube. Sandia Corporation has obtained incident pressures of 3000 psi using plywood shock tubes which are destroyed with each shot.<sup>10</sup>

To circumvent these problems, symmetric loads were obtained here by using the reflected pressure rather than the incident pressure. This is done by placing the model against a rigid back plate as in Fig. 39a. The incident blast reflects from this plate so that the model is exposed to the reflected pressure. Pressure records from this configuration with  $x = 18.5$  feet are given in Fig. 40. The model is exposed to a short part of the incident pressure as well as the reflected pressure, but the incident pressure is much lower (about one-fourth that of the reflected pulses in Fig. 40) and the duration is quite short (the time for the shock to traverse the model and return from the back plate). At the pressure gage location, 5.2 inches from the back plate, this time is 0.5 msec compared to a total pulse duration of about 3 msec. The impulse under the incident pressure toe is negligible, as is seen in the integrated pressure traces in Fig. 40.

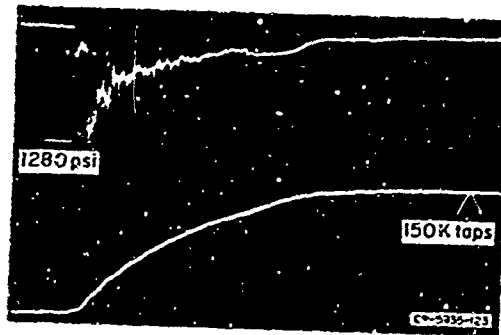
Peak pressures and impulses from these pulses are plotted in Figs. 41 and 38. Figure 38 shows that a peak pressure of 2000 psi can be obtained with a charge density of only 2 psf. The lowest pressure obtained here was about 300 psi, but pressures as low as 50 psi, the extreme of current interest, can easily be obtained with smaller charges. Therefore no apparatus was built and no tests were run with the model supported on a sting.



(a)  $w = 0.133$  psf (SHOT CT-11)



(b)  $w = 0.53$  psf (SHOT CT-11)



(c)  $w = 1.06$  psf (SHOT CT-13)

FIG. 40 INCIDENT AND REFLECTED PRESSURE PULSES IN CAPPED SHOCK TUBE (sweep rate 1 msec. cm)

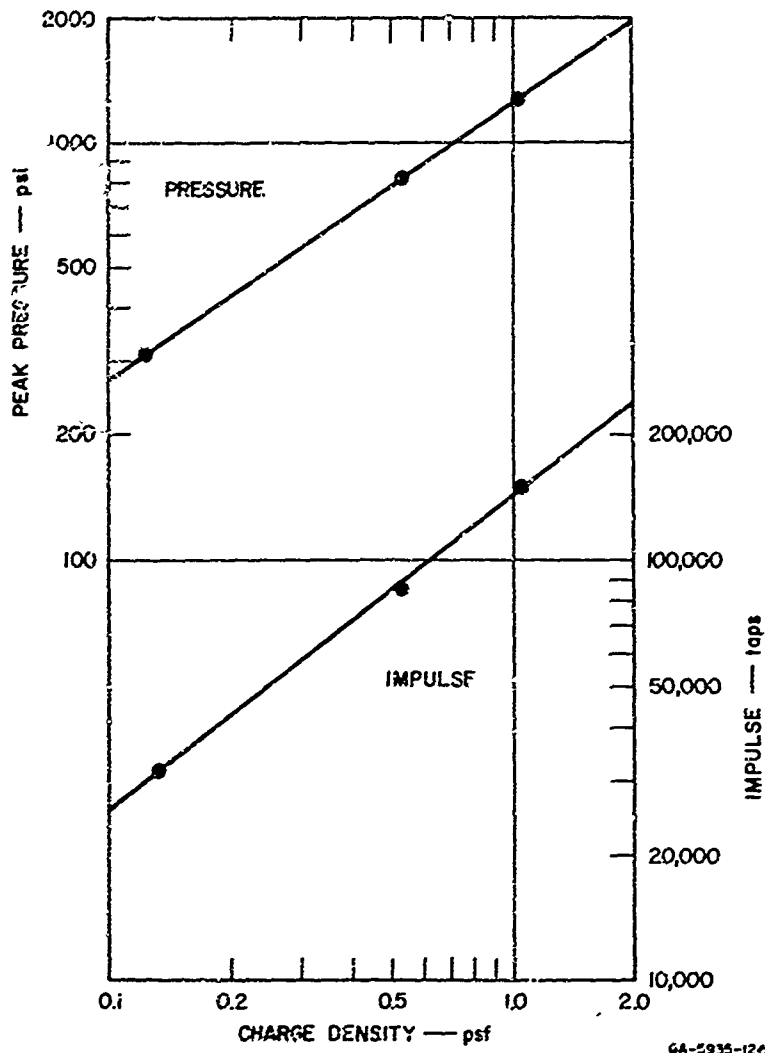


FIG. 41 PRESSURE AND IMPULSE VERSUS FLAT CHARGE DENSITY IN CAPPED SHOCK TUBE

Peak pressures are lower here than the lateral load pressures in Fig. 30 because the initial spike occurs only at the back plate and is lost by the time the reflected shock has traversed back to the gage location. The impulses here are about 1.5 times the lateral load impulses in Fig. 30 (again suggesting that calculation of reflected pressure pulses will give a good estimate of peak lateral loads). Figure 38

shows that the characteristic times of the capped 18.5-foot shock tube\* pulses are near 1.5 msec.

### 3. Recommendations for Future Work

Figure 38 also shows that there is a wide gap in pulse times from  $t_0 \approx 0.1$  msec for 4-foot-diameter cylindrical charges to  $t_0 = 1.5$  msec for the 18.5-foot shock tube. The most convenient method for obtaining intermediate durations would be to use the shock tube at smaller standoffs as was done for asymmetric loads. The minimum standoff for a 9-inch-long model is probably about 5 feet because of difficulties in obtaining a plane detonation and because at smaller standoffs the incident pressure pulse and shock decay along the length of the model become significant. Assuming that pressure in the reflected shock drops off in proportion to the total distance traveled, for a 0.75-foot-long structural model and a 5-foot standoff the pressure will drop about 13 percent along the length of the model. This drop is well within the overall accuracy of vulnerability analyses. Probably more important, at small standoffs the duration of the incident pressure toe (see Fig. 40) will become a sizable fraction of the overall pulse duration. Measurements of pressure pulses at various stations along the model should be made at smaller standoffs to investigate these effects.

Assuming that acceptable pulses can be obtained at a 5-foot standoff, a line has been drawn in Fig. 38 shifted to the left by a factor of 4 from the 18.5-foot shock tube line. A sizable gap still remains between this line and the pressure-impulse curve for 4-foot-diameter cylindrical charges. One possibility for providing pulses in this remaining region would be to make larger cylindrical charges with rigid plates at each end to reduce the amount of explosive needed. Once again, there is a need for a theoretical investigation of the diameters and charge weights needed for various diameter models, and of the stability of shock convergence for larger diameters.

---

\* Shock tube length was decreased from 20 to 18.5 feet because it was necessary to pour in a block of concrete to seal the base of the tube against water leakage.

## SECTION V

### LOADS OF OTHER DISTRIBUTIONS AND PULSE SHAPES

As discussed in the introduction, the basic approach proposed for determining structural response and vulnerability to transient surface loads is to test structures with pressure distributions and pulse shapes that simulate the principle features, but not all of the detail, of actual loads. Indeed, the actual loads are often not known and the number of possible loads at various target orientations is too large to contemplate examining each in detail. Instead, response is examined under a basic set of asymmetric and symmetric loads and then under loads perturbed from these basic loads. If significant differences in response to the perturbed loads are observed, then we know that response to a more extensive set of basic loads must be examined. If response to the perturbed loads does not differ significantly from the basic load response, then we are more confident that the basic loads chosen contain the significant features that influence response.

In this section we examine a few methods for changing pressure distribution and pulse shape. The experiments are merely exploratory because an extensive study of load variations should be closely coupled with the study of structural response. This is the subject of continuing research.

#### 1. Changes in Load Distribution

For impulsive loads from contact charges it has been common practice since the inception of these techniques to obtain smoothly varying distributions of interest by varying the explosive thickness, or equivalent thickness, around the test object. A logical question is whether similar methods can be used to vary the distribution in quasi-impulsive loads. Since quasi-impulsive loads are obtained here with sheet charges some distance from the model, the shape, as well as the thickness (density) in the charge, can be varied. Here we will describe a few experiments to examine the influence of charge shape and density variation on load distribution.

Two sets of quasi-impulsive load distribution experiments were performed. In the first, sheet charges of constant density were applied at various curvatures, and in the second, both curvature and density were varied. In both sets the general layout of the experiments was as illustrated in Fig. 42 for the constant density charges. These were

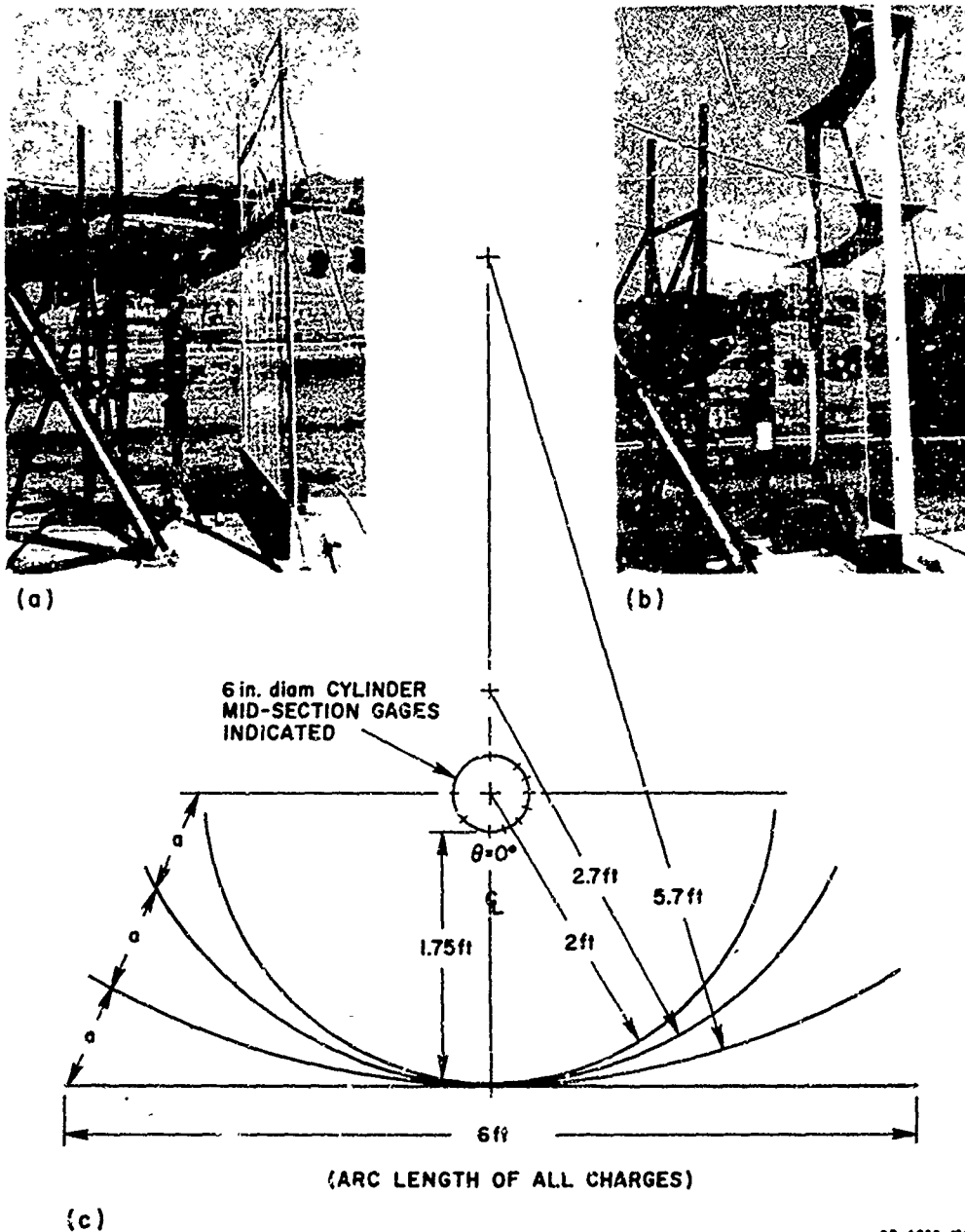


FIG. 42 EXPERIMENTAL ARRANGEMENT FOR CURVED CHARGES

made at  $w = 0.0143$  psf using 25 grain/ft Primacord on 3-inch centers. The charges were all made 6 feet square at a standoff of 1.75 feet (the standoff of the 4-foot-diameter cylindrical charges). Four curvatures were used, from flat to a semi-cylindrical form, with the distance  $a$  in Fig. 42c constant between charges.\* The charges were initiated from a central detonator at the top in Figs. 42a and b.

Pressure distributions from the constant density charges are plotted in Fig. 43. The curve for the flat charge is of the same family of curves discussed in Section III and is described approximately by the  $\cos^2\theta$  distribution in Eq. (23) (the pressure in Fig. 43 is about 20 percent higher at  $\theta = 45^\circ$  than given by Eq. (23)). As the curvature is increased the pressures toward either side of the model are increased as desired, but the converging shock at  $\theta = 0^\circ$  causes this pressure to increase also. The net effect is a more gradual pressure distribution than for the flat charge but still, even for the 2.7-foot radius charge, the pressure at  $\theta = 67.5^\circ$  is 300 psi, only 65 percent of the pressure at  $\theta = 0^\circ$ . However, if this distribution is compared with the distribution from the flat charge that gives the same peak pressure (the dashed curve in Fig. 43), the flat charge distribution is much steeper (as also seen by the increase in the ratio of  $P_r/P_i$  in Eq. (23)). The flat charge pressure at  $\theta = 67.5^\circ$  is 137 psi, only 31 percent of the  $\theta = 0^\circ$  pressure, compared to 65 percent for the curved charge.

From these results it is concluded that significant variations in pressure distribution can be obtained using variations in curvature alone. Even broader variations can be obtained by varying both charge density and curvature. Figure 44 gives a diagram of the variable density charges used to demonstrate this possibility. The density distribution is approximately linear from zero density at the center to a maximum density at the edge. Two shots were fired with this distribution, one flat and the other semicircular, both at a standoff of 1.75 feet as in Fig. 42.

\* Pressure records from the semi-cylindrical charge at constant density 0.0143 psf were lost because of difficulty in estimating proper oscilloscope settings.

The resulting pressure distributions are given in Fig. 45. The distribution from the flat charge is very nearly the same as the distribution from a uniform flat charge at the same average density, 0.057 psf. The distribution from the curved charge is markedly different from any of the other distributions, with a maximum pressure near  $\theta = \pm 80^\circ$ , at a value about 40 percent higher than the pressure at  $\theta = 0^\circ$ . In another shot, using a line charge (i.e., a purely cylindrical blast wave expanding from the charge), which represents the opposite extreme in charge density distribution, the pressure distribution was essentially the same as from the flat variable or flat uniform charges.

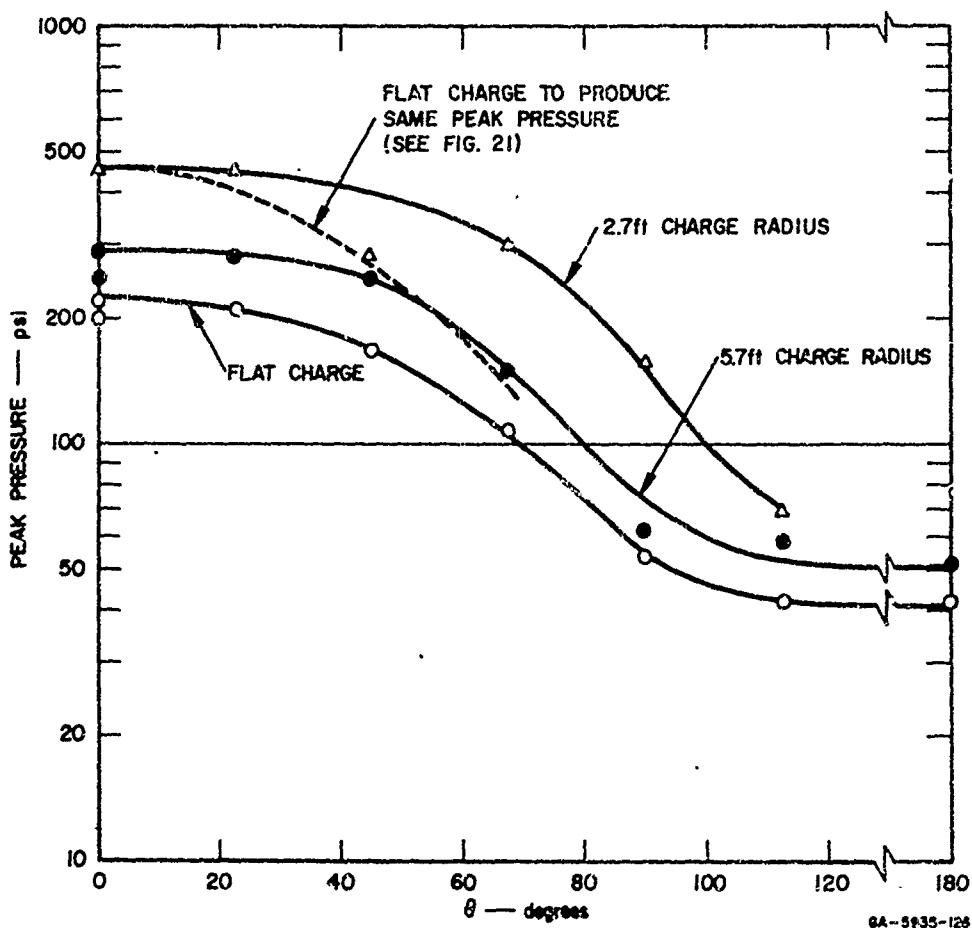


FIG. 43 PRESSURE DISTRIBUTIONS FROM UNIFORM 0.0143-psf CHARGES AT VARIOUS CURVATURES

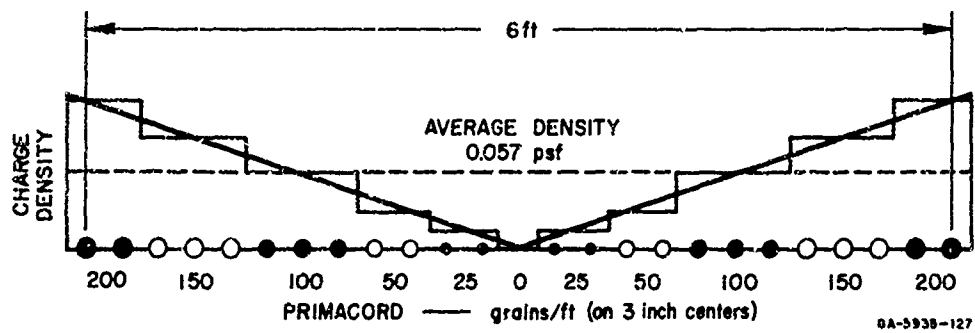


FIG. 44 CONFIGURATION OF VARIABLE DENSITY CHARGES

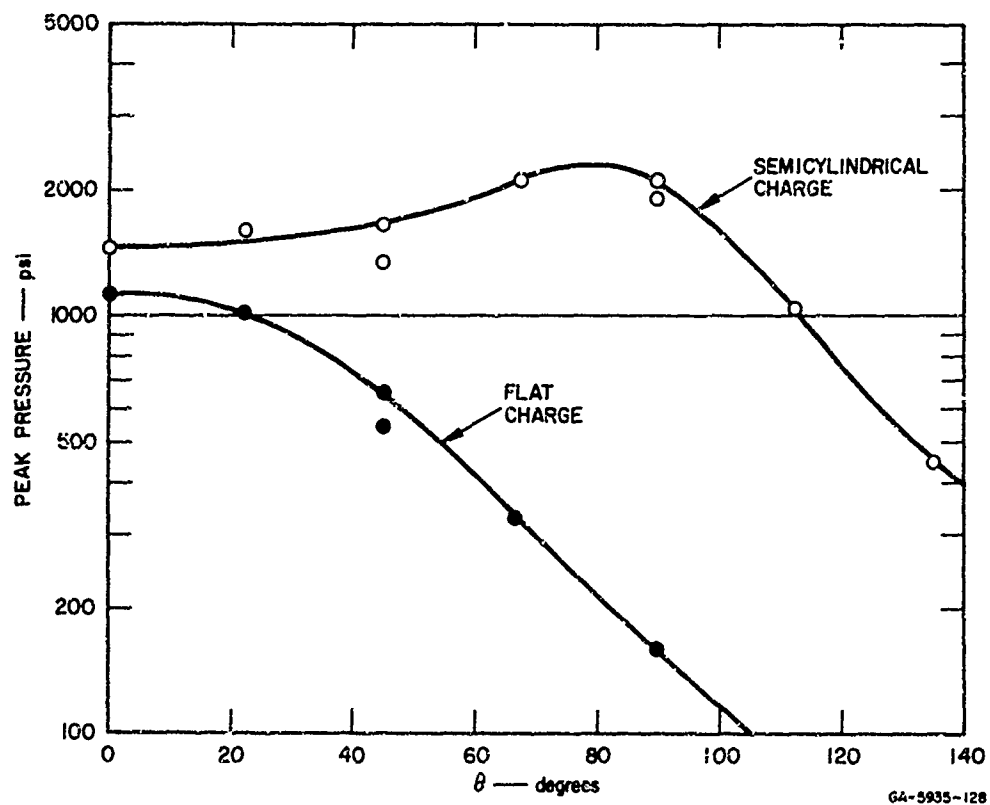


FIG. 45 PRESSURE DISTRIBUTIONS FOR FLAT AND SEMICYLINDRICAL CHARGES OF VARIABLE DENSITY (in Fig. 44)

The similarity in distribution from line charges and from uniform flat charges is to be expected because the shock radius at initial contact (1.75 feet) is large compared to the model radius (0.25 foot). The similarity to the distribution from the nonuniform flat charge is more surprising and apparently occurs because the standoff, although smaller than the half-width of the charge, is sufficiently large to allow the stronger shocks from the outer region of the charge to overtake and coalesce with the weaker shocks from the center of the charge. These results demonstrate that even at standoffs as small as 1.75 feet from a 6-inch-diameter model, charge curvature is more important than charge density distribution in determining load distribution.

Nevertheless, if the variable density charge is curved, the variation of charge density then has a significant effect on pressure distribution because coalescence into a single, nearly plane shock no longer occurs. It is apparent from Figs. 43 and 45 that with appropriate adjustment of curvature and density, pressure distributions can be obtained ranging from  $\cos^2 \theta$  over one side (from a uniform plane shock) to a uniform pressure on one side and a rapid pressure decay over the back side. Application of these distributions, along with the uniform distribution, should be sufficient to establish the sensitivity of structural damage to pressure distribution in quasi-impulsive loads.

For quasi-static loads, completely different loading schemes must be used to vary distribution, since the only variables open in the flat charge technique here are charge density and standoff. These affect mainly peak pressure and impulse and have already been used as the variables for producing the basic set of loads. One loading scheme, which conceptually allows any desired pressure distribution, is a set of vented chambers surrounding the model, with radial and axial vanes to allow separate adjustment of the pressure in each chamber. Development of this scheme would be relatively complicated and should await the results of the impulsive and quasi-impulsive load distribution tests to see how vigorously it should be pursued.

## 2. Changes in Pulse Shape

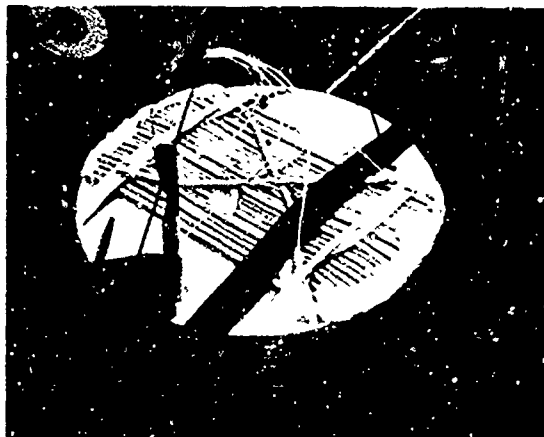
Pulse shapes were examined for shock tube loads to compare the pulses obtained from three methods of charge makeup in current use. These are (1) flat charges; (2) uniform charges of finite length, giving a reservoir of gas at a "constant" high pressure, as in conventional shock tubes; and (3) charges of finite length, but having a variable density to give a decaying shock.

The effect of the length of a uniform charge was studied first, using the charges shown in Fig. 46, placed at the base of the 20-foot shock tube. Charge length varies from zero (flat) to 6 feet, with total charge weight held constant. Pressure pulses from these charges, at  $\theta = 0^\circ$  on the 6-inch-diameter model, are shown in Fig. 47.\* Peak pressure decreases from 2100 psi for flat charge to 830 psi for the 6-foot charge, but impulse remains essentially constant at 100 ktaps. For the 6-foot charge the "steady" drag pressure of about 160 psi is clearly seen, extending from  $t = 1$  to  $t = 4$  msec after the initial shock. Also, at  $t = 2.1$  msec a jump in pressure occurs. For the 3-foot charge a "steady" drag phase is apparent, but it lasts for only about 1 msec and is indistinct. The second jump in pressure occurs earlier, at about  $t = 0.8$  msec. For the 1.5-foot charge there is no steady flow and the pressure jump occurs at about  $t = 0.25$  msec. Finally, for the flat charge there is neither steady flow nor a second jump in pressure; the pressure merely decays smoothly from 2100 psi, with four small pips probably caused by lateral reverberations in the tube.

These experiments demonstrate that pressure pulses from finite length charges differ considerably from the smooth pulses expected from most weapon effects. The source of the second pressure jump is not known but it obviously depends on charge length. For these charges,

---

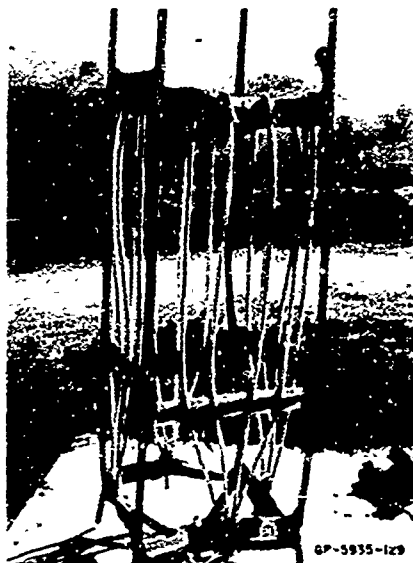
\*The quantity  $\alpha$  given in Fig. 47 is called "charge ratio" and is a measure of the local (shock tube) volume density of the charge in multiples of the density of air in the tube.



(a) L=0ft, STACKED FLAI



(b) L=1.5ft, 32 STRANDS



(c) L=3ft, 16 STRANDS

FIG. 46 SHOCK TUBE CHARGES OF VARIOUS LENGTHS (all made of 400 grain/ft Primacord, total weight 2.74 lb for each)

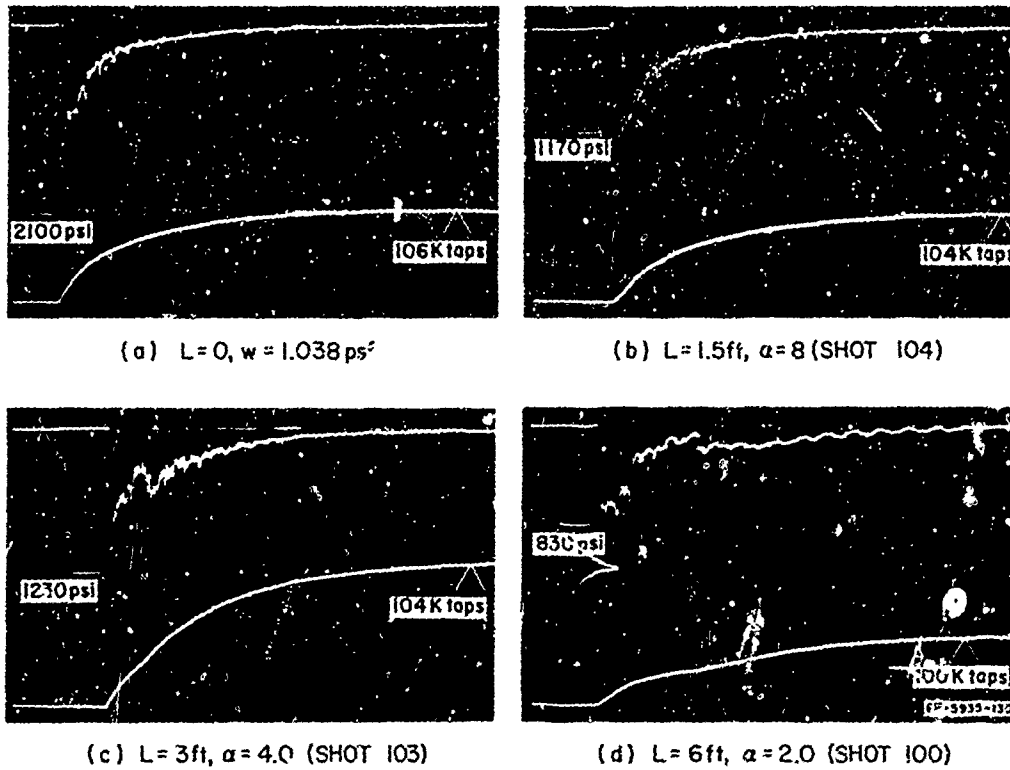
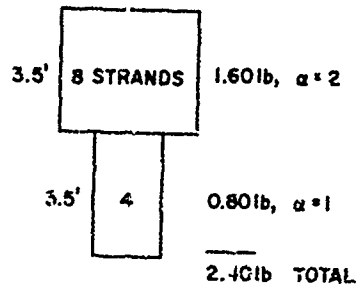
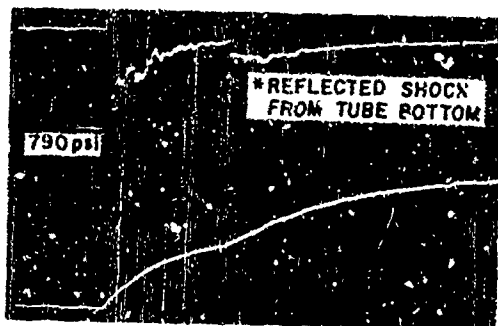


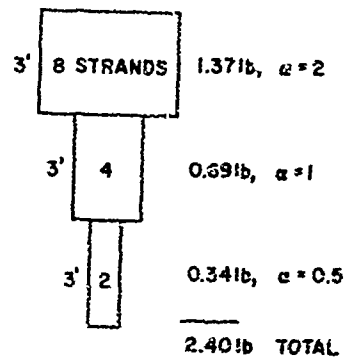
FIG. 47 SHOCK TUBE PRESSURE PULSES FOR VARIOUS LENGTH CHARGES OF SAME TOTAL WEIGHT (sweep rate 1 msec/cm)

total impulse appears to depend only on the total amount of gas that flows past the model, independent of how it is generated.

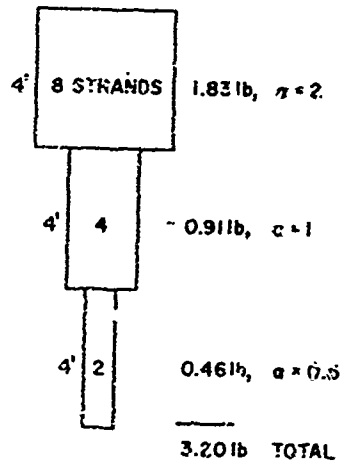
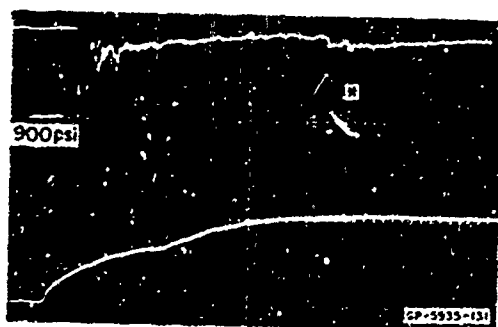
Variable density charges have been proposed for producing decaying rather than steady flow in shock tubes. Schematic diagrams of three such charges are given in Fig. 48 along with the corresponding pressure pulses. In each case the charge is made most dense near the model, at  $\alpha = 2$ , with succeeding charge sections at  $\alpha = 1$  and  $\alpha = 0.5$ . In each case the pressure is roughly exponential as desired, but the pulses are not smooth, probably because of the sudden changes in charge density. This is most apparent in Fig. 48c in which the front of the charge was only 8 feet from the model, allowing little time for discontinuities to smooth out. In no case is the pulse as smooth as from simple flat charges. It is concluded that while variable density charges produce useful loads, flat charges are superior and should be used if the shock tube can sustain the high local pressure near the charge.



(a) TWO CHARGE SECTIONS, TOTAL LENGTH 7ft



(b) THREE CHARGE SECTIONS, TOTAL LENGTH 9ft



(c) THREE CHARGE SECTIONS, TOTAL LENGTH 12ft

FIG. 4 PRESSURE PULSES FROM VARIABLE DENSITY SHOCK TUBE CHARGES (sweep rate 1 msec/cm)

## SECTION VI

### THEORY OF BLAST WAVES FROM INTENSE EXPLOSIONS IN A PERFECT GAS

#### 1. Introduction

Calculation of the diffracted pressures around the cylindrical models discussed in the preceding chapters is beyond the practical means of even the most advanced computer methods. Examples of the shock waves and vortices around the cylinder have been examined experimentally by Bleakney<sup>11</sup> and give a graphic demonstration of the complexity involved. However, the peak pressure and impulse at the leading edge of the cylinder can be estimated if the free-field blast wave is known. For blast waves of moderate duration, in which the flow around the cylinder is dominated by the diffraction phase, the peak pressure is the reflected pressure of the incident wave and the impulse is a significant fraction (of the order of 1/2 in many of the experiments reported here) of the reflected impulse from a flat, rigid wall. Both of these quantities are relatively easy to calculate. For blast waves of long duration the initial peak pressure is still the reflected pressure, but it decays in such a short time relative to the total blast duration that for structural response it is of secondary interest. For these blast waves it is useful to assume that at each instant the flow can be treated as quasi-steady at the instantaneous pressure, particle velocity, and density of the incident wave. The peak pressure to which the reflected pressure decays is then the drag pressure and the impulse can be estimated from a quasi-steady integration using wind tunnel data on steady flow past cylinders.<sup>12</sup>

Perhaps more important than enabling one to estimate the absolute magnitude of surface pressure pulses, these simple calculations give a means for establishing the trends to be expected from diffraction pulse measurements such as those given in the preceding sections. They can show, for example, the manner in which peak pressure and impulse will vary with charge size and distance-to-charge, and the gain to be expected

in going from spherical to flat charges. Such calculations are given in Section III. For symmetrical implosion from a cylindrical sheet of explosive a relatively simple one space variable theory can give the complete pressure pulse.

The present section treats blast wave theory in an ideal gas with these ends in mind. Section VI.2 summarizes the existing self-similar solutions for explosions in spherical, cylindrical, and plane geometries. Section VI.3 gives an approximate theory for the nonself-similar motion of the shock wave, taking into account the initial pressure in front of the shock. Section VI.4 gives suggestions for fruitful extensions of this effort.

## 2. Summary of Self-Similar Theory

The theory of blast waves from intense explosions in a perfect gas can be found in advanced texts on fluid mechanics,<sup>13,14</sup> but it is so fundamental to the interpretation of the present blast load experiments that we give it here in brief form. To aid in the calculation of blast wave parameters, pertinent numerical results for spherical and plane blast waves are also given.

### a. Characteristic Length and Self-Similarity

The explosion is visualized as a sudden release of a finite energy  $E_3$  in a small (spherical) volume of gas, giving in the limit an infinite energy density at the mathematical point of the explosion. As the gas expands away from the point of energy release it drives an intense spherical shock into the surrounding undisturbed gas. The average energy per unit volume within the expanding sphere decreases, eventually becoming comparable to the energy density in the undisturbed ambient gas,\* initially at pressure  $p_1$  and density  $\rho_1$ . For example,

\*Most of the gas and energy are contained in a thin layer immediately behind the shock, but the average energy decrease with increasing volume still gives a measure of the local energy density decrease. Also, the apparent release energy  $E_3$  is related to the chemical energy release through a complex process not treated here. Erode<sup>6</sup> showed that peak pressures from the self-similar theory are matched (in its range of validity) to numerical calculations for spherical explosions from TNT by taking  $E_3$  equal to the explosive release energy. The same result was found by Goodman<sup>15</sup> using compiled data from experimental pressure measurements.

in a perfect gas with specific heat ratio  $\gamma$ , the ambient gas has an internal energy (per unit volume) of

$$e = \frac{p_1}{(\gamma - 1)} \quad (27)$$

The release energy per unit volume of the blast sphere at radius  $r$  is

$$e_b = \frac{E_3}{\frac{4}{3} \pi r^3} \quad (28)$$

These energy densities are equal at radius

$$r_e = \left[ \frac{3(\gamma - 1)E_3}{4\pi p_1} \right]^{1/3} \quad (29a)$$

Similarly, for a cylindrical explosion from a release energy  $E_2$  per unit length along the axis,  $e_b = E_2/\pi r^2$  and the energy densities are equal at

$$r_e = \left[ \frac{(\gamma - 1)E_2}{\pi p_1} \right]^{1/2} \quad (29b)$$

For a plane explosion from a release energy  $E_1$  per unit area,  $e_b = E_1/2r$  and the energy densities are equal at

$$r_e = \frac{(\gamma - 1)E_1}{2p_1} \quad (29c)$$

Thus, in each geometry a characteristic length  $r_o$  can be defined by

$$r_o = \left( \frac{E_o}{p_1} \right)^{\frac{1}{\nu}} \quad (30)$$

where  $\nu = 1, 2,$  and  $3$  for a plane, cylindrical, and spherical explosions, and it is understood that the release energy  $E_o$  has appropriate units in each case. From the above examples we see that  $r_o$  is the blast radius (within a multiplicative constant) at which the release energy becomes comparable to the initial energy of the ambient gas enveloped by the blast. For a one-pound pentolite sphere in a standard atmosphere,  $r_o = 10.0$  feet.

If we confine our attention to the early motion ( $r \ll r_0$ ) the energy density within the blast is so large compared to the ambient energy density  $p_1/(\gamma - 1)$  that the ambient energy can be neglected. Stated another way, near the explosion the shock pressure is so much greater than  $p_1$  that  $p_1$  can be neglected. Under these conditions the ambient gas is described by  $\rho_1$  alone and there is no characteristic length. Consequently, with no length as a basis of comparison, the blast wave at any instant is identical to the blast wave at any other instant, except for scale changes as the sphere expands--the wave is self-similar. This similarity greatly simplifies the mathematical treatment because the flow can be described in terms of a single parameter  $\xi$  which is an appropriate combination of  $r$  and time  $t$ , rather than in terms of both  $r$  and  $t$  independently. At later times, as  $r$  approaches  $r_0$ , this simplification is no longer appropriate and the pressure  $p_1$  ahead of the shock must be considered. This will be done later. Also, the self-similar theory gives an infinite pressure as  $r \rightarrow 0$  and is therefore inapplicable at small distances from a real explosion. For small  $r$  the mechanism of energy release and the properties of real gases must be considered. These effects have been treated by several authors, for example by Brode.<sup>8,9</sup>

In the remainder of this subsection we consider that the ambient gas can be characterized by its density  $\rho_1$  alone so that the blast is self-similar. In all, there are five fundamental parameters\* in the self-similar problem:

$$E_0, \rho_1, \gamma, r, \text{ and } t$$

There are three fundamental units: force, distance, and time. The fundamental parameters can therefore be reduced to two dimensionless combinations. These are taken as

$$\gamma \quad \text{and} \quad \xi = r \left( \frac{\rho_1}{E_0 t^2} \right)^{\frac{1}{\gamma-2}} \quad (31)$$

\* Any other parameter can be expressed in terms of these.

The specific heat ratio  $\gamma$  is a constant for any given problem so that  $\xi$  is the single independent variable, demonstrating the self-similar nature of the problem. The dependent variables of primary interest are the pressure  $p$ , density  $\rho$ , and particle velocity  $v$ .

b. Motion of the Shock Front

Before attempting to describe the complete flow within the blast sphere, let us examine the motion of the shock front and the values of  $p$ ,  $\rho$ , and  $v$  just behind the shock. At each (and every) instant the pressure wave appears as shown in Fig. 49, in which both  $p$  and  $r$  have been normalized to their values  $p_2$  and  $r_2$  at the shock front. Since  $\xi$  is the only independent variable, each relative position behind the shock corresponds to a value of  $\xi$  and, in particular, the position of the shock itself corresponds to a unique value  $\xi_0$ .

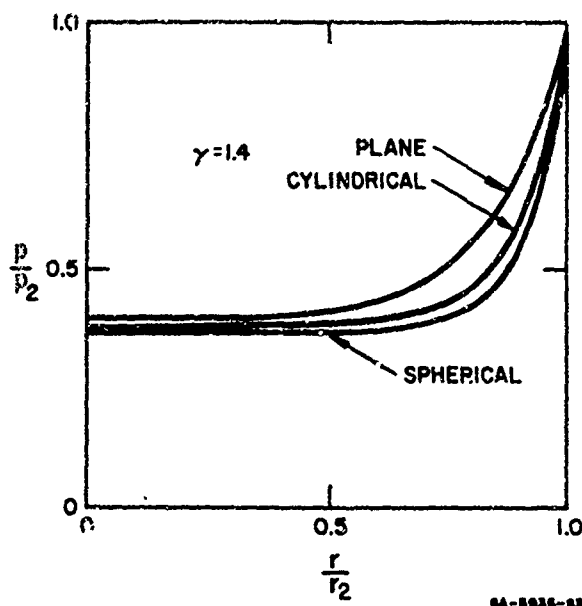


FIG. 49 PRESSURE DISTRIBUTION  
IN SELF-SIMILAR BLAST WAVES

From Eq. (31) the position of the shock is then

$$r_2 = \xi_0 \left( \frac{E_0 t^2}{\rho_1} \right)^{\frac{1}{\nu+2}} \quad (32)$$

and the velocity of the shock is

$$U = \frac{dr_2}{dt} = \left( \frac{2}{\nu+2} \right) \frac{r_2}{t} = \frac{2\xi_0}{\nu+2} \left( \frac{E_0}{\rho_1} \right)^{1/2} r_2^{-\frac{\nu}{2}} \quad (33)$$

The variables at the shock front can then be calculated directly from the strong shock relations

$$\nu_2 = \frac{2U}{\gamma+1}, \quad \rho_2 = \left( \frac{\gamma+1}{\gamma-1} \right) \rho_1, \quad p_2 = \frac{2\rho_1 U^2}{\gamma+1} \quad (34)$$

For example, the pressure behind the shock is

$$p_2 = \frac{8E_0 \xi_0^{\nu+2}}{(\nu+2)^2(\gamma+1)} \cdot \frac{1}{r_2^\nu} \quad (35)$$

Thus, using only dimensional analysis, all of the quantities at the shock can be determined within an unknown constant which can be determined by a single experiment. The dimensional analysis also shows that if all of the flow variables are measured as a function of time at a single radius from any single explosion, these data can be used to calculate the complete flow for any other combination of charge and radius, so long as the self-similar approximation is valid.

In the next section it will be convenient to use nondimensional dependent variables  $\nu'$ ,  $\rho'$ , and  $p'$ , defined using Eqs. (32) and (34) such that they are unity at the shock front.\*

\* This normalization and the subsequent self-similar solution follow that given by Landau and Lifshitz,<sup>14</sup> based on the original work by Sedov.<sup>13</sup> The self-similar problem was also solved independently by Taylor,<sup>16</sup> and by von Neumann.<sup>17</sup>

$$\begin{aligned}
 v &= \frac{4}{(2 + \nu)(\gamma + 1)} \frac{r}{t} v' \\
 \rho &= \rho_1 \left( \frac{\gamma + 1}{\gamma - 1} \right) \rho' \\
 p &= \frac{8\rho_1^4}{(2 + \nu)^2(\gamma + 1)} \frac{r^2}{t^2} p'
 \end{aligned}
 \tag{36}$$

c. Flow Behind the Shock

The equations for gas flow behind the shock are

$$\begin{aligned}
 \frac{\partial v}{\partial t} + v \frac{\partial v}{\partial r} + \frac{1}{\rho} \frac{\partial p}{\partial r} &= 0 \\
 \frac{\partial \rho}{\partial t} + \left( \frac{\partial}{\partial r} + v - 1 \right) (\rho v) &= 0 \\
 \left( \frac{\partial}{\partial t} + v \frac{\partial}{\partial r} \right) \left( \frac{p}{\rho^\gamma} \right) &= 0
 \end{aligned}
 \tag{37}$$

The first results from Newton's second law, the second from mass continuity, and the third from assuming the flow is isentropic in a perfect gas. The solution to these equations is simplified by observing that the first equation can be replaced by an energy integral which can be found immediately for the self-similar problem. This follows from the observation already made that in the self-similar problem the energy in the undisturbed gas can be neglected compared to the energy  $E_0$  released by the explosion; the total energy within the blast therefore remains constant. Furthermore, since we have a similarity flow, the energy of the gas inside any sphere of a smaller radius, which increases in such a way that  $\xi = \text{any constant}$  (not only  $\xi_0$ ), must remain constant; the radial velocity of this sphere, from Eq. (31), is  $v_n = 2r/5t$  for  $\nu = 3$ . To express this in terms of the flow variables, consider an incremental expansion as shown in Fig. 50. Particles that leave the sphere with

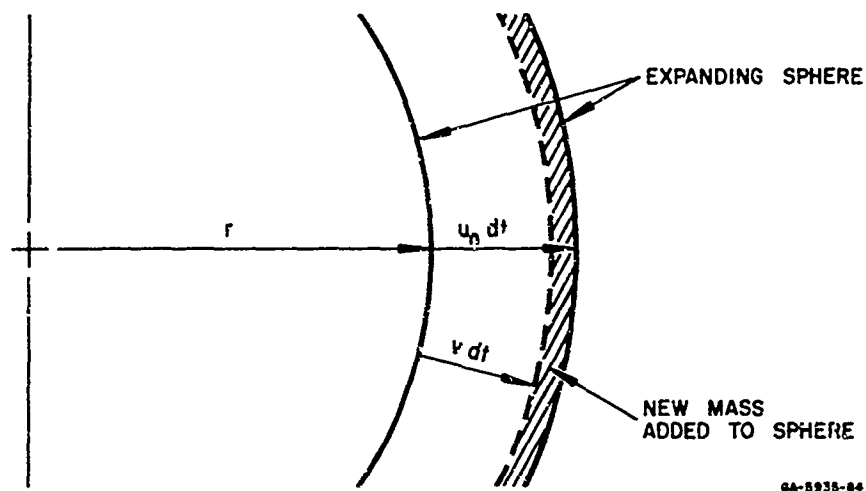


FIG. 50 INCREMENTAL EXPANSION OF AN ARBITRARY SPHERE WITHIN THE BLAST WAVE

velocity  $v$  bring with them an energy  $4\pi r^2 \rho v dt (w + v^2/2)$ , where the enthalpy  $w$  is the internal energy plus the flow work per unit mass:

$$w = e + \frac{p}{\rho} = \frac{p}{\rho(\gamma - 1)} + \frac{p}{\rho} = \frac{p\gamma}{\rho(\gamma - 1)} \quad (38)$$

If the total energy within the sphere is to remain constant, this must be equal to the energy in the incremental volume swept out by the expanding sphere:  $4\pi r^2 \rho u_n dt (e + v^2/2)$ . Equating these energies gives

$$v \left( w + \frac{v^2}{2} \right) = u_n \left( e + \frac{v^2}{2} \right) \quad (39)$$

This same equation results in all three geometries, since the area factor ( $4\pi r^2$  here) divides out. Using  $u_n = 2r/(\gamma + 2)t$  from Eq. (33) and the dimensionless variables in Eq. (36), this energy balance gives

$$\frac{p'}{\rho'} = \frac{(\gamma + 1 - 2v')v'^2}{2\gamma v' - \gamma - 1} \quad (40)$$

in all three geometries. Converting the last two equations in (37) to the primed dependent variables, and independent variables  $\xi$  and, say  $t' = t$  (in order to properly differentiate  $r/t$  in Eq. (36)) yields

$$\frac{dv'}{d \log \xi} + \left( v' - \frac{\gamma + 1}{2} \right) \frac{d \log \rho'}{d \log \xi} = -\gamma v' \quad (41)$$

$$\frac{d}{d \log \xi} \left( \log \frac{\rho'}{\rho'^{\gamma}} \right) = \frac{(\gamma + 2)(\gamma + 1) - 4v'}{2v' - (\gamma + 1)}$$

Thus the three partial differential equations (37) have been reduced to an algebraic equation (40) plus two ordinary differential equations (41).

To solve these equations it is convenient to treat  $v'$  as the independent variable rather than  $\xi$  because derivatives of  $\xi$  and  $\rho'$  can be expressed as functions of  $v'$  alone. These can be integrated by quadrature. After laborious manipulation this procedure gives explicit solutions for  $\xi$  and  $\rho'$  in terms of  $v'$  which, together with  $p'$  from Eq. (40), completes the solution of the problem. The resulting equations are elementary but lengthy; they are given in Ref. 14, p. 395, for spherical geometry and in Ref. 13, p. 219, for all three geometries.

The parameter  $\xi_0(\gamma)$  is determined such that the total energy in the gas is equal to the energy  $E_0$  of the explosion. (The relation between  $E_0$  and the explosive yield, however, remains unknown without a study of the explosive gas flow.<sup>9</sup>)

$$E_0 = \int_0^{r_0} \left( \frac{\rho v^2}{2} + \frac{p}{\gamma - 1} \right) A \, dr \quad (42)$$

where  $A = 4\pi r^2$  for spherical waves,  $A = 2\pi r$  for cylindrical waves, and  $A = 2$  for plane waves. Sedov,<sup>13</sup> instead of finding  $\xi_0$  from Eq. (42), defines an artificial energy  $E = E_0/\alpha$  to be used in Eq. (32) such that  $\xi = 1$  at the shock front and  $\alpha$  is found from Eq. (32). The two parameters are related by  $\alpha = \xi_0^{-(\gamma+2)}$ . In this notation  $\lambda$  is used in place of  $\xi$ . Figure 5! gives Sedov's curves for  $\alpha$  versus  $\gamma$

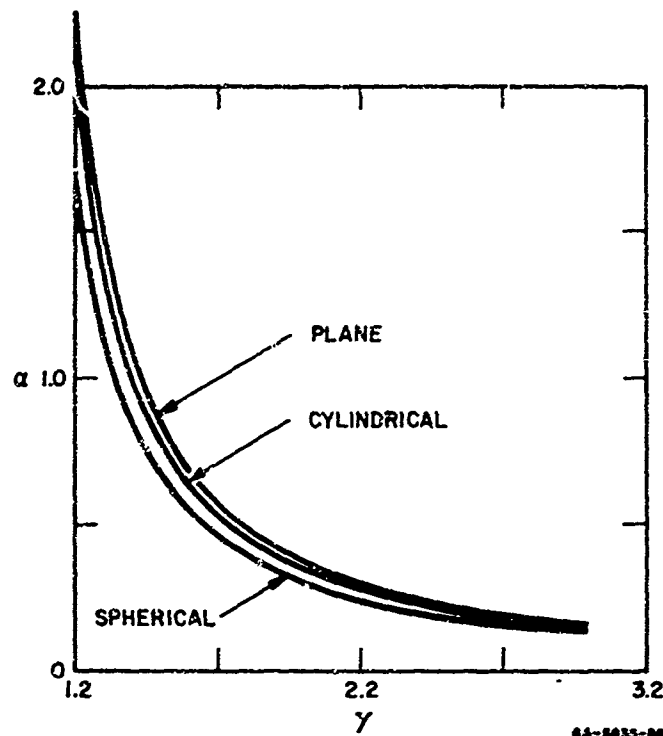


FIG. 51 THE RATIO  $E_0/E = \alpha = \xi_0^{-(\nu+2)}$  AS A FUNCTION OF  $\gamma$

for all three geometries. For air ( $\gamma = 1.4$ ),  $\alpha = 1.075, 1.00,$  and  $0.85$  for plane, cylindrical, and spherical geometries, respectively.

d. Incident Pressure Pulses from Self-Similar Solution

Sedov also gives  $p/p_2, \rho/\rho_2,$  and  $v/v_2$  as functions of  $\lambda = r/r_2$  behind the shock in all three geometries. For use in blast load calculations we need to find  $p, \rho,$  and  $v$  as functions of time at a fixed radius  $r_f$ . Here we find the incident pressure pulse  $p(t)$ , the quantity of most interest for estimating diffracted pulses from available data. From Eqs. (35) and (32) the peak pressure is

$$p_f = \frac{8E_0}{\alpha(\nu + 2)^2(\gamma + 1)} \cdot \frac{1}{r_f^\nu} \quad (43)$$

at time

$$t_f = \left( \frac{c\rho_1}{E_0} \right)^{1/2} r_f^{\frac{\nu+2}{2}} \quad (44)$$

At a later time  $t$  the shock front  $r_2$  has continued past  $r = r_f$  and the pressure at  $r_f$  has decayed because both  $p_f/p_2$  (see Fig. 49) and  $p_2$  decrease with time. We define a normalized pulse time  $\tau$  after the shock has passed according to

$$\tau = \frac{t - t_f}{t_f} = \left( \frac{r_f}{r_2} \right)^{-\frac{\nu+2}{2}} - 1 \quad (45)$$

in which Eq. (32) has again been used. The pressure at  $\tau$  is

$$p(\tau) = p_2 \left( \frac{p}{p_2} \right) = p_f \left( \frac{r_f}{r_2} \right)^\nu \left( \frac{p}{p_2} \right) \quad (46)$$

Equations (45) and (46) are parametric equations for  $p$  and  $\tau$  with  $r_f/r_2$  as a parameter. We can now replace  $r_f$  by  $r$  without confusion so that these equations become

$$\tau = \lambda^{-\frac{\nu+2}{2}} - 1, \quad \frac{p(\tau)}{p_f} = \lambda^\nu P_\nu(\lambda) \quad (47)$$

where  $P_\nu(\lambda)$  is  $p/p_2$  vs.  $\lambda = r/r_2$  as tabulated by Sedov,<sup>13</sup> pp. 222-223, and given here in Fig. 49.

Curves of  $p(\tau)/p_f$  are given in Fig. 52 for  $\nu = 1, 2,$  and  $3$ . The general shapes of the curves do not differ appreciably for small  $\tau$ , but for large  $\tau$  the pressure decays more slowly in cylindrical and plane geometry than in spherical geometry. The difference is particularly evident for plane geometry. (See also Fig. 6 for a comparison with the time scale for the plane wave compressed to give close agreement at early times.) For  $\tau \gg 1$  the limiting forms of Eqs. (47), along with the observation that  $P_\nu(\lambda = 0)$  are constants, yield

$$\frac{p(\tau)}{p_f} \rightarrow P_\nu(0) \tau^{-\frac{2\nu}{\nu+2}} \quad (48)$$

Thus, for large times the incident pressure decays as  $t^{-2/3}$ ,  $t^{-1}$ , and  $t^{-6/5}$  in plane, cylindrical, and spherical geometries.

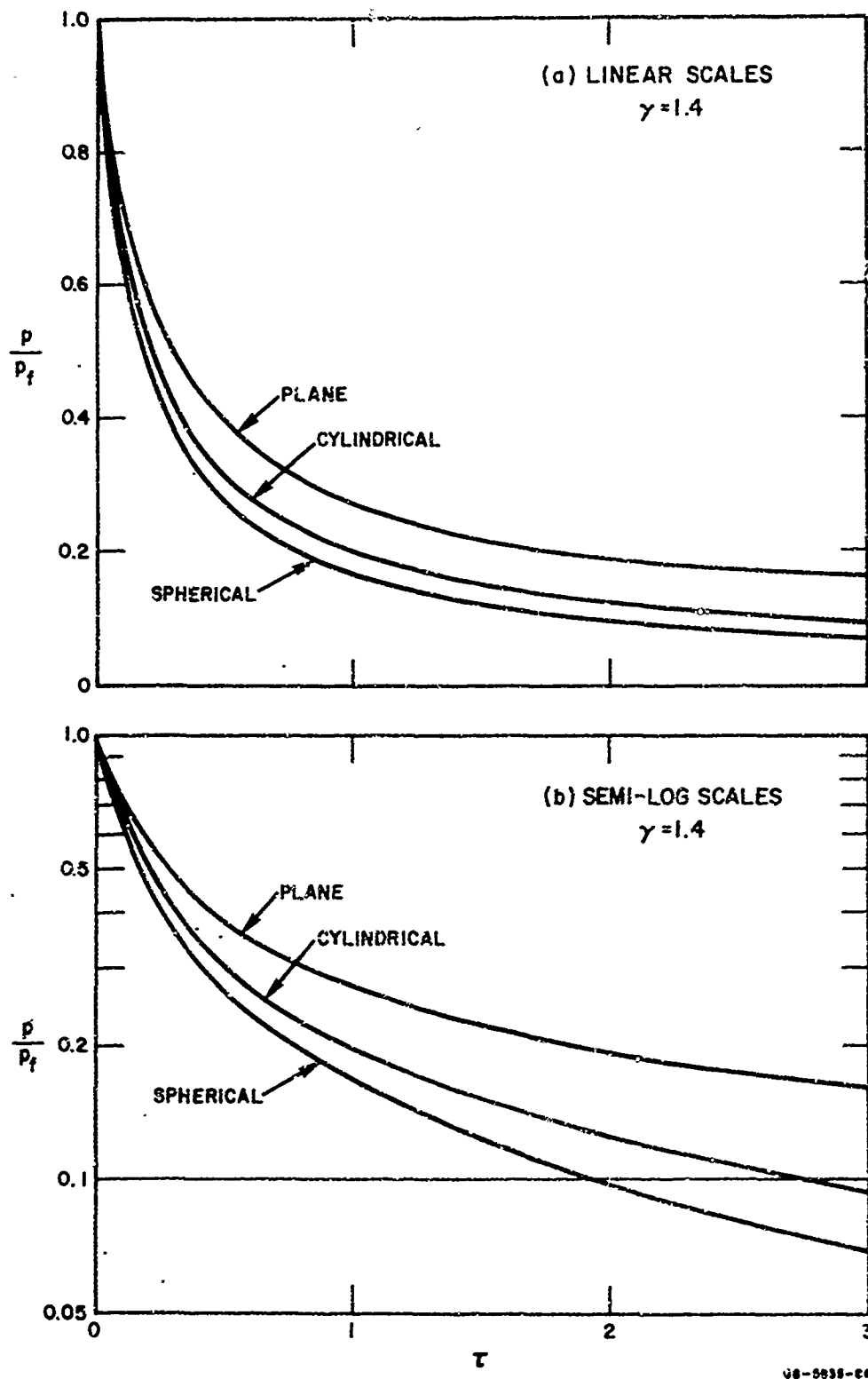


FIG. 52 INCIDENT PRESSURE PULSE AT  $r = r_f$ , FOR SELF-SIMILAR FLOW, NORMALIZED TO  $p_f = 8E_o/a(\nu + 2)^2(\gamma + 1)r_f^\nu$ ,  $t_f = (\alpha\rho_1/E_o)^{1/2}r_f^{(\nu+2)/2}$

### 3. Shock Front Motion into an Initial Pressure

In the remainder of this section we will treat blast waves taking into account the initial pressure (and energy) of the ambient gas ahead of the shock front. As in the self-similar theory, determination of the motion of the shock front is relatively simple and will be undertaken before the complete flow behind the shock is studied. Since we include now the energy entering the blast sphere as it envelopes the surrounding gas, the shock will decay less rapidly than in the self-similar theory, in which the total energy was taken to be constant.

A method for finding a first (and second) approximation to the modified shock front motion was suggested by Korobeinikov.<sup>18</sup> He compared the dependence on  $r_2$  of the particle velocity  $v_2$  just behind the shock front as given by the self-similar theory (valid for small  $r_2$ ) and by the asymptotic theory of Landau<sup>14</sup> (pp. 375-377, valid for large  $r_2$ ) and observed that there was little change in this dependence. This is demonstrated in Table I. On the basis of this observation, he suggested that for intermediate values of  $r_2$  the particle velocity can be taken from the self-similar theory and then the shock velocity  $U$  can be calculated from the particle velocity jump condition across the shock. Using this modified expression for  $U$  the pressure  $p_2$  and density  $\rho_2$  can then be determined from the other two jump conditions.

Table I

DEPENDENCE OF PARTICLE VELOCITY  $v_2$  ON SHOCK RADIUS  $r_2$

Theory	Geometry		
	$v = 1$ plane	$v = 2$ cylindrical	$v = 3$ spherical
Self-similar	$r_2^{-1/2}$	$r_2^{-1}$	$r_2^{-3/2}$
Acoustic shock	$r_2^{-1/2}$	$r_2^{-3/4}$	$r_2^{-1} \log^{-1/2} \left( \frac{r_2}{r_0} \right)$

Conservation of mass, momentum, and energy across the shock give the following jump conditions for a perfect gas:

$$\frac{v_2}{c_1} = \frac{2}{\gamma + 1} \left( \frac{M^2 - 1}{M} \right)$$

$$\frac{p_2}{p_1} - 1 = \frac{2\gamma}{\gamma + 1} (M^2 - 1) \quad (49)$$

$$\frac{\rho_2}{\rho_1} = \frac{(\gamma + 1)M^2}{2 + (\gamma - 1)M^2}$$

expressed in terms of shock Mach number  $M$ , defined by

$$M = \frac{U}{c_1}, \quad c_1^2 = \frac{\gamma p_1}{\rho_1} \quad (50)$$

where  $c_1$  is the sound speed in the ambient gas ahead of the shock. Using Eqs. (33) and (34), the particle velocity from the self-similar solution is

$$v_2 = \frac{4}{(\nu + 2)(\gamma + 1)} \left( \frac{E_0}{\alpha \rho_1} \right)^{1/2} r_2^{-\nu/2} \quad (51)$$

in which we have used  $\alpha = \xi_0^{-(\nu+2)}$ . Since we now take account of  $p_1$ , it is convenient to express  $r_2$  in terms of the characteristic length  $r_0 = (E_0/p_1)^{1/\nu}$ , giving a dimensionless shock radius  $R$ .

$$R = \frac{r_2}{r_0} \quad (52)$$

Using this definition and  $c_1$  from Eq. (50), the particle velocity is expressed by

$$\frac{v_2}{c_1} = \frac{4R^{-\nu/2}}{(\nu + 2)(\gamma + 1)(\alpha\gamma)^{1/2}} \quad (53)$$

Combining Eq. (53) with the first of Eqs. (49) gives the desired expression for shock velocity:

$$M = A + \sqrt{A^2 + 1} \quad (54)$$

where

$$A^2 = \frac{R^{-\nu}}{\alpha\gamma(\nu + 2)^2} \quad (55)$$

Substituting Eq. (54) into the second of Eqs. (49) gives the decay of the shock overpressure with distance.

$$\frac{p_2}{p_1} - 1 = \frac{4\gamma}{\gamma + 1} A^2 \left[ 1 + (1 + A^{-2})^{1/2} \right] \quad (56)$$

The limiting form for small radius  $R$  ( $\text{large } A$ ) is

$$\frac{p_2}{p_1} - 1 = \frac{8\gamma}{\gamma + 1} A^2 = \frac{8R^{-\nu}}{\alpha(\nu + 2)^2(\gamma + 1)} \quad (57)$$

After multiplying by  $p_1$  and taking  $p_1 \rightarrow 0$ , this is seen to coincide with the self-similar formula (35). The density  $\rho_2$  can be similarly found.

For large  $R$  the self-similar particle velocity (51) becomes a poor approximation for cylindrical and spherical waves (see Table I). In this range the small disturbance expressions in Table I can be used, matching the large and small  $R$  expressions at some intermediate value. For example, in the spherical case Korobeinikov matches them at  $R = 2$  to obtain

$$\frac{v_2}{c_1} = \begin{cases} \frac{4R^{-3/2}}{5(\gamma + 1)(\alpha\gamma)^{1/2}} & R \leq 2 \\ \frac{4R^{-1}[\log(R/2) + 1]^{-1/2}}{5(\gamma + 1)(2\alpha\gamma)^{1/2}} & R \geq 2 \end{cases} \quad (58)$$

Similarly, for cylindrical blast waves we take

$$\frac{v_2}{c_1} = \begin{cases} \frac{R^{-1}}{(\gamma + 1)(\alpha\gamma)^{1/2}} & R \leq 2 \\ \frac{R^{-3/4}}{2^{1/4}(\gamma + 1)(\alpha\gamma)^{1/2}} & R \geq 2 \end{cases} \quad (59)$$

Using these expressions, the incident overpressure throughout the entire range of  $R$  is given by Eq. (56) with the following expressions for  $A^{-2}$ :

$$\begin{aligned} \nu = 1 \quad \text{Plane waves} \\ (\alpha = 1.075 \text{ for } \gamma = 1.4) \quad A^{-2} = 3\alpha\gamma R \quad \text{all } R \\ \\ \nu = 2 \quad \text{Cylindrical waves} \\ (\alpha = 1.00 \text{ for } \gamma = 1.4) \quad A^{-2} = \begin{cases} 16\alpha\gamma R^2 & R \leq 2 \\ 16\sqrt{2} \alpha\gamma R^{3/2} & R \geq 2 \end{cases} \\ \\ \nu = 3 \quad \text{Spherical waves} \\ (\alpha = 0.85 \text{ for } \gamma = 1.4) \quad A^{-2} = \begin{cases} 25\alpha\gamma R^3 & R \leq 2 \\ 50\alpha\gamma R^2 [\ln(R/2) + 1] & R \geq 2 \end{cases} \end{aligned} \quad (60)$$

The reflected overpressure ratio is given by

$$\frac{p_r}{p_i} - 1 = \left[ \frac{(2\mu + 1)p_2/p_1 + 1}{\mu p_2/p_1 + 1} \right] \left( \frac{p_2}{p_1} - 1 \right) \quad (61)$$

where  $\mu = (\gamma - 1)/(\gamma + 1)$ .

Figures 53 and 54 give curves of incident and reflected overpressure ratios from these equations. Also shown are (dashed) curves from compiled data on spherical pentolite explosions, taken from Goodman.<sup>15</sup> The approximate theory matches identically with the experimental data for

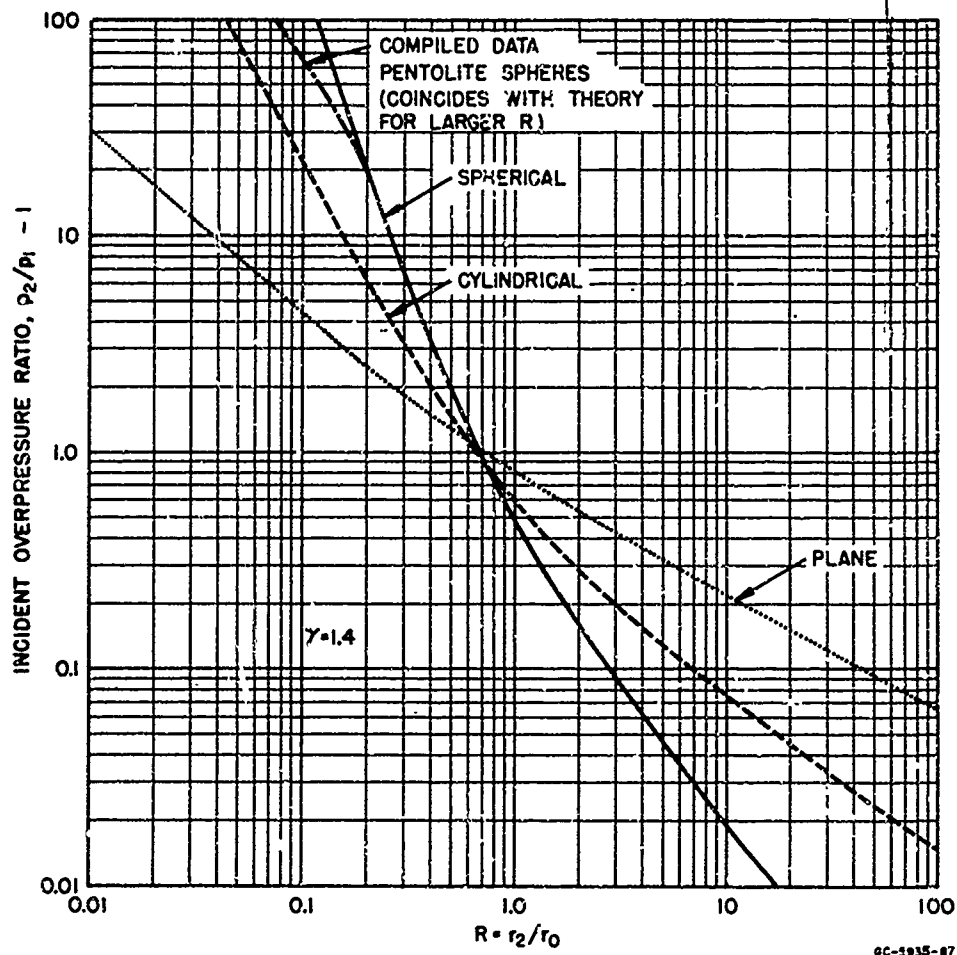


FIG. 53 INCIDENT SHOCK OVERPRESSURE RATIO vs.  $R = r_2/(E_0/p_1)^{1/\nu}$

$R > 0.2$  if  $E_0$  is calculated on the basis of 1430 cal/gm (pressures were measured only out to  $R = 7$ ). At smaller radii real gas and explosive properties become important and the measured pressures are smaller than predicted by the self-similar theory. At larger radii other mechanisms of wave damping, such as viscosity, become important. However, the range of validity of the approximate theory is quite broad, giving reliable reflected overpressure ratios from about 0.1 to 100 a useful range for quasi-impulsive structural response. This excellent agreement for spherical explosions gives some confidence in using the approximate solutions for cylindrical and plane blast waves, for which few experimental data are available.

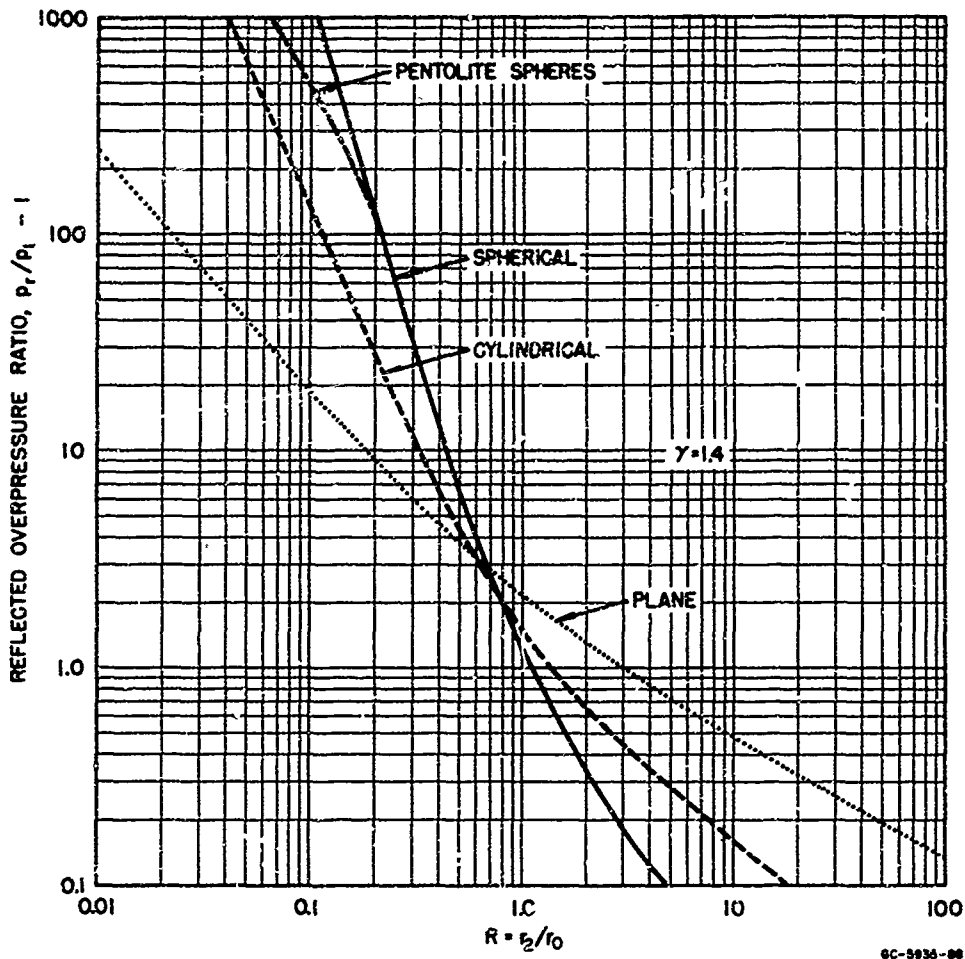


FIG. 54 REFLECTED SHOCK OVERPRESSURE RATIO vs.  $R = r_2/(E_0/p_1)^{1/\nu}$

#### 4. Future Theoretical Program

In order to determine the pressure-time history behind the shock, the complete flow must be calculated. Although extensive calculations have been made for spherical blast waves,<sup>8,9,13</sup> the authors know of no published results for plane waves other than the self-similar curves of Sedov<sup>13</sup> which were used here in Section VI.2. The usefulness of plane blast waves in structural testing, as demonstrated in the preceding sections, gives sufficient motivation for making plane wave calculations. The calculations should include a complete description of both the flow behind the shock as it moves out from the explosion and the reflected

wave from a flat, rigid wall at a sequence of values of  $R$ . The reflected pressure-time histories would give a first estimate of the diffracted pressure-time history on structural models and an upper bound on the impulse.

These calculations could be made using the self-similar solution as initial conditions at a radius small enough that the ambient pressure can be neglected, as was done in the spherical problem.<sup>8</sup> Similarly, the self-similar theory could be used to start the calculations for the implosion-explosion problem from cylindrical sheet charges. In this case the reflected pressure pulse at the rigid cylindrical boundary (model) would be the true model pressure within the accuracy of the theory. Such calculations would allow relatively inexpensive determination of peak pressure and impulse as functions of charge diameter and thickness for various model sizes. They should be accompanied by an investigation of the stability of the implosion process, which defines the allowable parameters for acceptably small pressure fluctuations.

## REFERENCES

1. Lindberg, H. E.; Anderson, D. L.; Firth, R. D.; Parker, L. V.; "Response of Reentry Vehicle-Type Shells to Blast Loads," Stanford Research Institute Final Report, Lockheed Missiles and Space Company P.O. 24-14517, Contract AF 04(694)-655, Vol. IV-C, 30 September 1965.
2. Abrahamson, G. R.; Lindberg, H. E.; "Explosive Simulation for Structural Response of Reentry Vehicles and Satellites (U)," 10th Symposium on Space and Ballistic Missile Technology, sponsored by Space Systems Division and Ballistic Systems Division, Air Force Systems Command, conducted by Aerospace Corporation, August 1965, Vol. V, pp. 83-134 (S-RD).
3. Abrahamson, G. R.; "Explosively Induced Impulses," Stanford Research Institute, Poulter Laboratories PLTR 009-62, July 20, 1962.
4. Abrahamson, G. R.; Lindberg, H. E.; "Review of Explosive Simulation and Theoretical Investigations of X-Ray Induced Structural Effects (U)," Stanford Research Institute Final Report, DASA 1598, Contract W.O. 655 supported by DASA Nosp 65043-c (FBM), January 1965 (S-RD).
5. Holt, R. E.; Crist, R. A.; "Calibration of a Six-Foot- and a Two-Foot-Diameter Shock Tube," Univ. New Mexico Report under Contract AF 29(601)-4520, Report No. AFSWC-TDR-63-5, April 1963.
6. Duff, R. E.; Blackwell, A. N.; "High-Explosive-Driven Wind Tunnels for High-Altitude Blast Simulation," 9th Symposium on Ballistic Missile and Space Technology, sponsored by Space Systems Division and Ballistic Systems Division, Air Force Systems Command, conducted by Aerospace Corporation, August 1964, Vol. II, pp. 419-446.
7. Kinney, G. F.; Explosive Shocks in Air, the Macmillan Co., New York, N.Y., 1962.
8. Brode, H. L.; "Numerical Solutions of Spherical Blast Waves," J. Appl. Phys., 26, 6, pp. 766-775, June 1955.
9. Brode, H. L.; "Blast Wave from a Spherical Charge," Phys. Fluids, 2, 2, pp. 217-229, March-April 1959.
10. Deal, W. E.; Taylor, J. W.; "Explosive Simulation of Nuclear Blast on Test Vehicles," 9th Symposium on Ballistic Missile and Space Technology, sponsored by Space Systems Division and Ballistic Systems Division, Air Force Systems Command, conducted by Aerospace Corporation, August 1964, Vol. II, pp. 359-394.

11. Bleakney, W.; et al.; "The Cylinder and Semicylinder in Subsonic Flow," Princeton Univ., Phys. Dept. TR-II-13, ONR Contract N6ori-105, Task II, July 1952.
12. Gowen, F. E.; Perkins, E. W.; "Drag of Circular Cylinders for a Wide Range of Reynolds Numbers and Mach Numbers," NACA-TN-2960, June 1953.
13. Sedov, L. I.; Similarity and Dimensional Methods in Mechanics, Academic Press, New York, N.Y., 1959, pp. 146-260.
14. Landau, L. D.; Lifshitz, E. M.; Fluid Mechanics, Vol. 6 of Course of Theoretical Physics, Addison-Wesley Publishing Co., Reading, Massachusetts, 1959, pp. 372-377, 392-396.
15. Goodman, H. J.; "Compiled Free-Air Blast Data on Bare Spherical Pentolite," Ballistic Research Laboratories Report No. 1092, February 1960.
16. Taylor, G. I.; "The Formation of a Blast Wave from a Very Intense Explosion. I. Theoretical Discussion," Proc. Royal Soc., A., Vol. CCI (1959), pp. 159-174, and "II. The Atomic Explosion of 1945," *ibid.* pp. 175-186.
17. Bethe, H. A.; et al.; "Blast Wave," LA-2000, Los Alamos Scientific Laboratory of the Univ. of California, written August 1947, distributed March 1958, Chapter 2, "The Point Source Solution," by John von Neumann, pp. 27-56.
18. Korobeinikov, V. P.; "Approximate Formulas for Calculation of the Characteristics of a Shock Wave Front in the Case of a Point Explosion in a Gas," Dokl. Akad. Nauk SSSR, 3, 3, 1956, pp. 557-559, Translated Associated Tech. Services, Inc., Glen Ridge, N.J.

UNCLASSIFIED

Security Classification

DOCUMENT CONTROL DATA - R&D		
<i>(Security classification of title, body of abstract and indexing annotation must be entered when the overall report is classified)</i>		
1. ORIGINATING ACTIVITY (Corporate author) Stanford Research Institute, Poulter Laboratories Menlo Park, California 94025		2a. REPORT SECURITY CLASSIFICATION UNCLASSIFIED
		2b. GROUP
3. REPORT TITLE STRUCTURAL RESPONSE OF SPINE VEHICLE; Vol II, Simulation of Transient Surface Loads by Explosive Blast Waves		
4. DESCRIPTIVE NOTES (Type of report and inclusive dates) 4 December 1965-15 September 1966		
5. AUTHOR(S) (Last name, first name, initial) Lindberg, H. E.; Firth, R. D.		
6. REPORT DATE May 1967	7a. TOTAL NO. OF PAGES 112	7b. NO. OF REFS 18
8a. CONTRACT OR GRANT NO. AF 29(601)-7129		8a. ORIGINATOR'S REPORT NUMBER(S) AFWL-TR-66-163, Vol II
a. PROJECT NO. 5710		
c. Subtask No. 01.028		
d.	8b. OTHER REPORT NO(S) (Any other numbers that may be assigned this report) Contractors report no. SRI Project FGU-5935	
10. AVAILABILITY/LIMITATION NOTICES This document is subject to special export controls and each transmittal to foreign governments or foreign nationals may be made only with prior approval of AFWL (WLRP), Kirtland AFB, NM, 87117. Distribution is limited because of the technology discussed in the report.		
11. SUPPLEMENTARY NOTES (Distribution Limitation Statement No. 2) Applies to Abstract.	12. SPONSORING MILITARY ACTIVITY AFWL (WLRP) Kirtland AFB, NM 87117	
13. ABSTRACT Techniques are described for simulating blast-type transient surface loads of nearly exponential pulse shape having characteristic times (impulse/peak pressure) ranging from 10 to 1000 $\mu$ sec (the quasi-impulsive range for cylindrical shells about 1 foot in diameter). Pressure-time histories are measured at various positions around and along cylindrical models 3.5, 6, and 12 inches in diameter. A basic set of loads is obtained consisting of two limiting pressure distributions, an asymmetric distribution typical of side exposure to a normally incident blast wave, and a symmetric distribution typical of nose-on exposure. All of the loads are obtained using sheet explosive charges of various forms, from flat to semi-cylindrical to completely cylindrical surrounding the model and flat charges suspended at various standoffs in a shock tube. In support of the experiments, the self-similar solutions for blast waves from intense explosions are used to calculate the range of sheet charges needed to produce loads of interest and to show that the corresponding spherical charges become much too small and much too large for practical application near the extremes in load duration. Approximate formulas are also derived (the Korobeinikov theory) for the variation of peak pressure with distance from plane, cylindrical, and spherical charges. The range of validity of the formulas extends from high pressures, where the self-similar solutions are valid, to acoustic shock pressures. Experimental measurements from the present program and from compiled blast data show excellent agreement with the theory over the entire range.		

DD FORM 1 JAN 60 1473

UNCLASSIFIED  
Security Classification

14. KEY WORDS	LINK A		LINK B		LINK C	
	ROLE	WT	ROLE	WT	ROLE	WT
Blast waves Explosives Simulation techniques Shock tube						

**INSTRUCTIONS**

1. **ORIGINATING ACTIVITY:** Enter the name and address of the contractor, subcontractor, grantee, Department of Defense activity or other organization (corporate author) issuing the report.
- 2a. **REPORT SECURITY CLASSIFICATION:** Enter the overall security classification of the report. Indicate whether "Restricted Data" is included. Marking is to be in accordance with appropriate security regulations.
- 2b. **GROUP:** Automatic downgrading is specified in DoD Directive 5200.10 and Armed Forces Industrial Manual. Enter the group number. Also, when applicable, show that optional markings have been used for Group 3 and Group 4 as authorized.
3. **REPORT TITLE:** Enter the complete report title in all capital letters. Titles in all cases should be unclassified. If a meaningful title cannot be selected without classification, show title classification in all capitals in parenthesis immediately following the title.
4. **DESCRIPTIVE NOTES:** If appropriate, enter the type of report, e.g., interim, progress, summary, annual, or final. Give the inclusive dates when a specific reporting period is covered.
5. **AUTHOR(S):** Enter the name(s) of author(s) as shown on or in the report. Enter last name, first name, middle initial. If military, show rank and branch of service. The name of the principal author is an absolute minimum requirement.
6. **REPORT DATE:** Enter the date of the report as day, month, year, or month, year. If more than one date appears on the report, use date of publication.
- 7a. **TOTAL NUMBER OF PAGES:** The total page count should follow normal pagination procedures, i.e., enter the number of pages containing information.
- 7b. **NUMBER OF REFERENCES:** Enter the total number of references cited in the report.
- 8a. **CONTRACT OR GRANT NUMBER:** If appropriate, enter the applicable number of the contract or grant under which the report was written.
- 8b, 8c, & 8d. **PROJECT NUMBER:** Enter the appropriate military department identification, such as project number, subproject number, system number, task number, etc.
- 9a. **ORIGINATOR'S REPORT NUMBER(S):** Enter the official report number by which the document will be identified and controlled by the originating activity. This number must be unique to this report.
- 9b. **OTHER REPORT NUMBER(S):** If the report has been assigned any other report numbers (either by the originator or by the sponsor), also enter this number(s).
10. **AVAILABILITY/LIMITATION NOTICES:** Enter any limitations on further dissemination of the report, other than those

imposed by security classification, using standard statements such as:

- (1) "Qualified requesters may obtain copies of this report from DDC."
- (2) "Foreign announcement and dissemination of this report by DDC is not authorized."
- (3) "U. S. Government agencies may obtain copies of this report directly from DDC. Other qualified DDC users shall request through \_\_\_\_\_."
- (4) "U. S. military agencies may obtain copies of this report directly from DDC. Other qualified users shall request through \_\_\_\_\_."
- (5) "All distribution of this report is controlled. Qualified DDC users shall request through \_\_\_\_\_."

If the report has been furnished to the Office of Technical Services, Department of Commerce, for sale to the public, indicate this fact and enter the price, if known.

11. **SUPPLEMENTARY NOTES:** Use for additional explanatory notes.
12. **SPONSORING MILITARY ACTIVITY:** Enter the name of the departmental project office or laboratory sponsoring (paying for) the research and development. Include address.
13. **ABSTRACT:** Enter an abstract giving a brief and factual summary of the document indicative of the report, even though it may also appear elsewhere in the body of the technical report. If additional space is required, a continuation sheet shall be attached.  
It is highly desirable that the abstract of classified reports be unclassified. Each paragraph of the abstract shall end with an indication of the military security classification of the information in the paragraph, represented as (TS), (S), (C), or (U).  
There is no limitation on the length of the abstract. However, the suggested length is from 150 to 225 words.
14. **KEY WORDS:** Key words are technically meaningful terms or short phrases that characterize a report and may be used as index entries for cataloging the report. Key words must be selected so that no security classification is required. Identifiers, such as equipment model designation, trade name, military project code name, geographic location, may be used as key words but will be followed by an indication of technical context. The assignment of links, roles, and weights is optional.